Effect of Si-doping on the Properties of AlN Powder

Yujin CHO

February 2016

Effect of Si-doping

on the Properties of AlN Powder

Yujin CHO
Doctoral Program in Materials Science and Engineering

Submitted to the Graduate School of
Pure and Applied Sciences
in Partial Fulfillment of the Requirements
for the Degree of Doctor of Philosophy in
Engineering

at the
University of Tsukuba

Abstract

Deep-ultraviolet (UV) light-sources with emission wavelengths ranging from 230~350 nm (3.5~5.4 eV) have various applications including water purification, air sterilization, medical treatment, etc. Although conventional UV lamps are available, those lamps have several disadvantages such as the need for high voltage, etc. Hence, the development of UV solid state lightening devices such as UV-light emitting diodes (UV-LEDs) has been given great attention.

Aluminum Nitride (AlN) is a promising material for UV emitting sources due to its wide band gap (6.2 eV), high thermal conductivity and chemical inertness. AlN based III-V nitride heterostructures thin films are have currently used for UV-LEDs, but they are difficult to synthesize and expensive. Our suggestion is to use AlN powders as UV emitting sources of in a field emitting device (FED). Although AlN powders are now commercially available, they are mostly low quality and contain many defects and impurities, i.e., Oxygen. Most of these defects act as non-radiative centers, to hinder the UV emissions. Thus, the control of the defects in AlN powder is necessary to use AlN as an UV emitter. Recently, the group of Prof. Hirosaki at NIMS has found that Si-doping has improved the solubility of Eu into the AlN lattice, thus producing enhanced blue light from Eu^{2+} [50-53]. But the mechanisms in which Si acts on the AlN powder were still unclear.

In this thesis, the effects of Si-doping on the structural, chemical, electrical and optical properties of AlN powders were elucidated. It was found that Si has three effects on AlN powders depending on the Si concentration: 1. Purification of AlN powder by removing O impurities; 2. Substitution of Al lattice site; 3. Generation of SiAlON secondary phases. The

first one occurred at low, the second one at the medium, and the third one at high Si concentration. AlN with medium Si doping showed the most promising properties as UV emitters. Based on cross-sectional investigation, a sintering mechanism model of Si-doped AlN powders was proposed: Si_3N_4 additives promoted liquid phase sintering by melting and combining the AlN particles. Consequently, the O out-diffusion along the grain boundaries induced a particle growth and Si dissolution in AlN particles.

Finally, we propose some perspectives to get deeper UV emission from Si-doped AlN powder, and to extend our method to other wide band gap materials.

Acknowledgements

The work in the following dissertation would not have been possible without the help, support, guidance and efforts of many people. I wish to acknowledge them for their contributions.

Firstly, I would like to express my sincere gratitude to my supervisor, Prof. Takashi Sekiguchi, for the tremendous guidance, support and encouragement he has provided me on this journey.

I am also grateful my mentor, Dr. Benjamin Dierre for instilling in me the qualities of being a good scientist.

With regards to powder synthesis, equipment training, general discussions and study of phosphors, I wish to thank people of Sialon Unit, especially to Dr. Takashi Takeda, Dr. Kohsei Takahashi, Dr. Rong-jun Xie, Dr. Naoto Hirosaki, Mr. Yoshinobu Yamamoto, Mr. Eisuke Bannai, and Ms. Kazuko Nakajima for their help and support over the years.

I am deeply grateful to my colleagues who trained me or offer me to use of equipment. Prof. Naoki Fukata, Prof. Kazuhiro Marumoto, Dr. Dong-hyun Son, and Dr. Yoshiaki Kamigaki helped me in ESR; Dr. Benjamin Dierre, Dr. Kentaro Watanabe and Dr. Ken Nakagawa in CL; Dr. Kiyotaka Iiyama in EDS, Dr. Hidehiko Tanaka and Dr. Keiko Suzuta in particle size analyzer; Dr. Daiming Tang in TEM; Dr. Mitsuaki Nishio in EPMA; Dr. Takashi Kimura in XPS; Dr. Yoon-hyun Kim helped me to use many software.

I sincerely express my appreciations to all of my lab members, especially to Mrs. Kazuko Tomura, for her unending care and assistance, Dr. Jun Chen, Dr. Jiptner Karolin, Dr. Ronit Roneel Parakash, Dr. Xian-jia Luo, and Mr. Toshihide Agemura for their warm help in many aspects of my study and life. I am grateful to my MD supervisor, Prof. Jiho Chang for his guidance.

Finally, I want to thank my family. 아버지, 어머니 그리고 오빠, 감사하고 사랑합니다.

2016.02

Yujin CHO

Table of contents

Chapter 1: Importance of Si-doped AlN powder for UV emitters

1.1 Motivations

Since early 1990s until now, many efforts have been done on the development of Aluminum Nitride (AlN) and its compound for ultraviolet (UV) optoelectronics application[1-3]. The optical properties of AlN crystals are strongly affected by the presence of defects. Thus, the understanding the luminescence origin and control of defects in AlN are the key to fabricate high efficiency optical devices. This dissertation describes the way to control defects in AlN powder by Si-doping. The fundamental study of Si-doped AlN powders will be reported.

1.1.1 Importance of UV applications

UV radiation ranges from 10 to 400 nm in the electromagnetic spectrum, being shorter than that of visible light but longer than X-rays. It is subdivided into a number of ranges recommended by the ISO standard[4], as shown in Table 1-1. A wide variety of application has been identified depending on its wavelength. UVA light called chemical ray, is used for industrial applications such as curing system, forensic analysis and solid state lightening. UVB light called health ray causes the body to make vitamin D, an important nutrient. It is mainly used for medical and bio-agent detection, skin treatment and optical sensors. The highest energy of UVC light known as germicidal ray deactivates the DNA of bacteria, virus and other pathogens or causes damage to the microorganisms or polymers. Thus it is beneficial for the disinfection of water, air and substrates without chemical treatments[5-8]. Consequentially, developing UV emitting sources is greatly important for these society demands.

Table 1-1. *Electromagnetic spectrum of Ultraviolet (UV) radiation.*[4]

Name	Abbreviation	Wavelength (nm)	Photon energy (eV)
Ultraviolet A	UVA	315–400	3.10–3.94
Ultraviolet B	UVB	280–315	3.94–4.43
Ultraviolet C	UVC	100–280	4.43–12.4
Near ultraviolet	NUV	300–400	3.10–4.13
Middle ultraviolet	MUV	200–300	4.13–6.20
Far ultraviolet	FUV	122–200	6.20–10.16
Hydrogen Lyman-alpha	H Lyman-α	121–122	10.16–10.24
Vacuum ultraviolet	VUV	10–200	6.20–124
Extreme ultraviolet	EUV	10–121	10.24–124

1.1.2 Conventional UV sources

- UV lamps

Various conventional UV lamps such as a mercury vapor, xenon arc or metal-halide arc lamps are available, the mercury vapor lamp being popularly used. This lamp emits UVC bands due to the mercury. However, the bulky lamps reveal many disadvantages such as the need for high voltage, the release of pollutant wastes, short lifetimes, and long warm-up times[9].

-UV light emitting diodes (UV-LEDs)

Development of UV-LED on flux density, stability and lifetime was promoted for replacing traditional UV light sources. Recent advances were reported in the field of III-Nitride

based LEDs, addressing the deep UV emitters based on high Al-content AlGaN quantum wells (QWs)[10-13]. Specifically, the identification of large TM-polarized emission from high Al-content AlGaN QWs and the use of delta-like QW structures were reported. In addition, recent works have also focused on the development of AlInN-based[14, 15] and AlGaInN-based alloys[16] for achieving emission in deep UV spectral regime, and the polar III-Nitride QW[17] was also used for suppressing the charge separation in the QWs. UV LEDs are more environmentally friendly as they do not contain mercury, do not produce ozone and consume less energy. However, due to the difficulty of achieving adequate ohmic contacts to n-AlGaN with increasing Al percentage as well as the high resistivity of p-AlGaN, the output power decreases significantly as the wavelength is shortened[17-20]. Also, individual LEDs focus on a very small area and the cost is high compared with the efficiency. Therefore, this type of UV-LED sources would be difficult to be easily commercialized using current technology.

1.1.3 Electron beam pumped (EBP) UV sources

Electron-beam pumped (EBP) source, which takes advantage of a field-emission display (FED) structure is a promising UV device. It provides an alternative to the lamps and UVLEDs describe above. Figure 1-1 shows the basic structure of UV-EBP emitter. It uses a cold-cathode gun that directly excites the UV-fluorescent screen, so that it is possible to realize a planar emission. A variety of UV-emitting material can be used for UV-fluorescent screen and several groups have constructed the UV-EBP device by using AlGaN QWs[21, 22]. QWs can be fabricated by sophisticated technique such as chemical vapor deposition (MOCVD) or molecular beam epitaxy (MBE). However, such structures were not grown under thermal equilibrium condition, thus difficult to control. We have focused on the powders that can be fabricated by simple sintering method under thermal equilibrium conditions.

By this approach, a large-area UV device can be realized using a printed electronic technology. For UV-emitting powders, such as borates (SrB_4O_7:Eu, $Ba_2B_5O_9Cl$:Eu), a silicate (Ba_2SiO_5 :Pb), phosphates ($Sr_{2-x}Mg_xP_2O_7$:Eu) and a sulphate ($CaSO_4$:Eu) have been reported[23-25]. However the drawbacks of these compounds are their sensitivity to moisture, giving a poor chemical stability, and their significant degradation under high energy electron bombardment. Thus, nitrides have got attentions for this device application because of chemical stability[26-28]. On the other hand, similar to UV-LEDs, these device performances are still insufficient for commercialization because of lack of efficiency originating from poor crystallinity of powders. To overcome this problem, we propose the high quality AlN powders as phosphors for EBP-UV device.

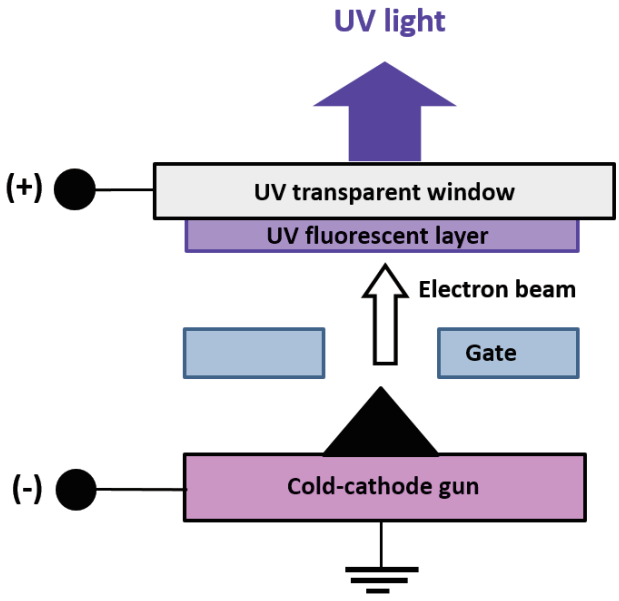

Figure 1-1. *Basic structure of UV EBP device.*

1.2 Aluminum Nitride (AlN) for UV optoelectronics

AlN is a promising material for deep UV applications. It has the largest direct band-gap among group III-nitrides, corresponding to 6.2 eV. This allows an emission of around 200 nm to be achieved. Moreover, its high thermal conductivity and intense chemical inertness under harsh conditions such as e-beam irradiation, high temperature and intense light illumination[1, 29], make it essential for applications in UV wavelength range as well as high temperature operation.

1.2.1 Aluminum Nitride (AlN)

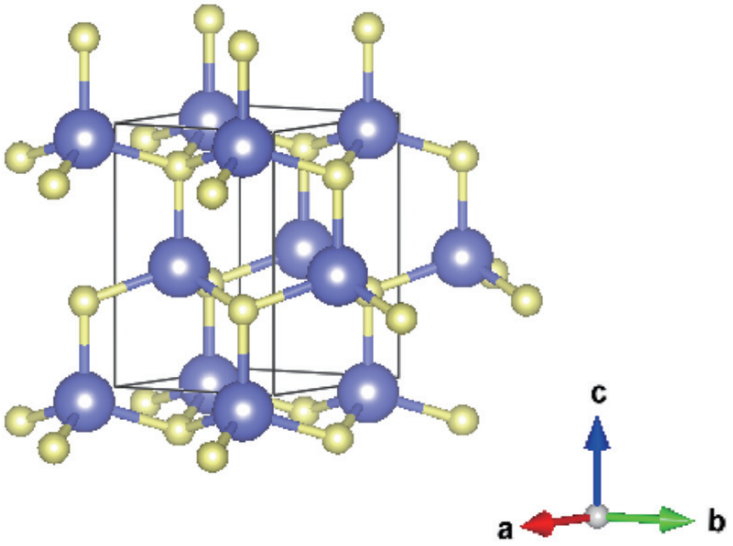

Figure1-2. *Schema of wurtzite AlN structure (Blue-Al, yellow-N).*

AlN is mostly covalent material with wurtzite where anions are hexagonal close packed with the cations filling half the tetrahedral sites, as seen in Figure 1-2. The lattice parameter is a=b=3.11, c=4.98 and c/a=1.600 Å. The space group for this structure is P63mc group. The structure can be modified into a variety of polytypes with the addition of impurities of oxygen and silicon[29]. Since AlN does not form naturally, it must be synthesized by high-temperature reaction, such as carbothermal reaction, or spark plasma synthesis[30].

1.2.2 Defects of AlN powder

Although AlN is known as an excellent material for UV emitters, there are some difficulties to make the AlN-based emitters a commercial reality. The first one is the native defects that are responsible for a blue-UV band emission[31]. Bulk AlN contains a plenty of defects especially originated form oxygen impurities. They exist at N lattice site as substitutional impurity (O_N). It frequently couples with charge compensating aluminum vacancies (V_{Al})[32-35]. Nitrogen vacancies (V_N) is also stable in wurtzite AlN[34, 36, 37]. The concentration V_N has inversely related to the concentration of O_N centers[38]. Other impurities such as metal ions can occupy aluminum sites (M_{Al}). O_N is considered as a deep donor, while V_{Al} an acceptor[39]. The defect complexes (O_N-V_{Al}) are thought as deep acceptors. V_N are expected to be act as amphoteric defect changing from donor to acceptor without a stable neutral state[40]. M_{Al} also induces deep levels with defect complexes[35, 41, 42]. Thus, these defect levels are occupying different energy state in band-gap. On the other hand, defects induced luminescence in the region between 3 ~ 4eV has been intensively studied but it is still controversial issue [31, 43, 44]. Especially, in case of AlN powders, the defects influence is more serious than thin films because of high amount of impurities. It is known that when O concentration is over 1.0 at.%, a new type of defect is stable, in which an aluminum atom is octahedrally bound to oxygen atoms, resulting in extended defect[31].

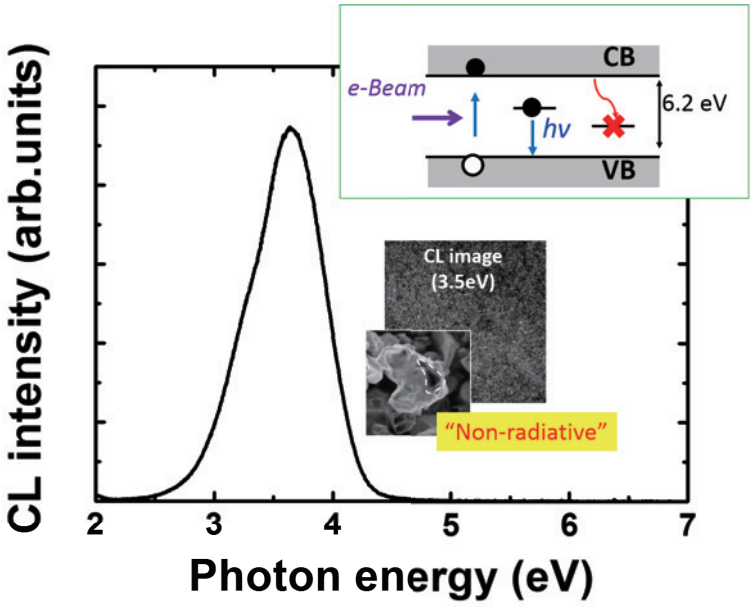

Figure 1-3. *Cathodoluminescence (CL) spectra of commercial AlN powder with insert CL image at 3.5 eV and emission mechanism.*

Figure 1-3 shows cathodoluminescence (CL) spectrum and SE and 3.5eV CL images of commercial AlN powders. The commercial AlN powders usually emit blue bands but not band-edge emission. The biggest problem is the existence of non-radiative defects that may be originated from extended defects or defects complexes[31]. These defects may result in particle dissociation and low quality. Thus, understanding the origin of blue-near UV emissions of AlN is important to control the defects as well as improve the optical property of AlN powders.

1.3 Defects control of AlN powder

The defects in AlN powder can be controlled by high temperature annealing (over 1500°C) to rearrange the lattice under high pressure to prevent nitrogen decomposition[56]. Another possibility is to intentionally dissolve foreign atoms (doping) that will affect the properties of the Al-N compound. This may promote the particle growth and densification. Ceramic sintering method is considered the most suitable way to perform such methods under thermal equilibrium conditions.

1.3.1 Sintering theory

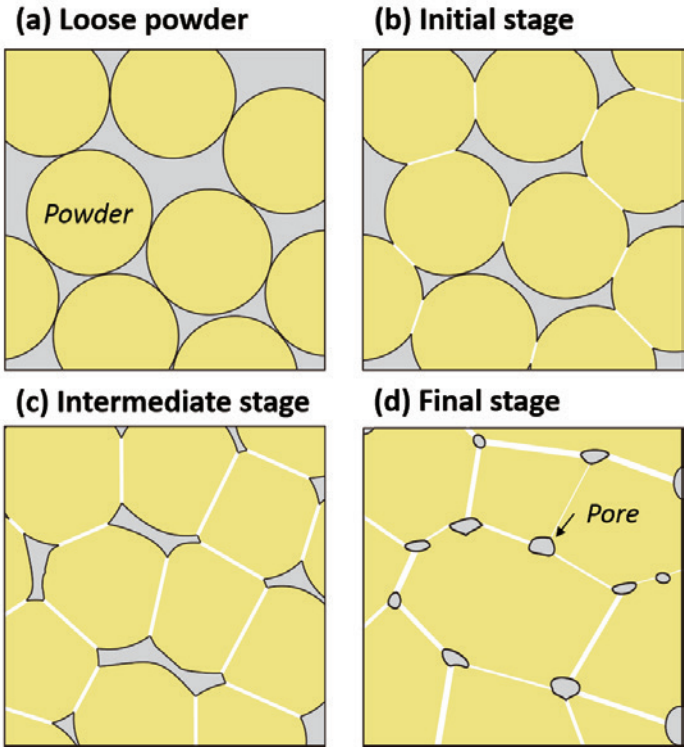

Figure 1-4. *Classical sintering stages.*[45]

Classic stages of sintering a powder are illustrated in Figure 1-4. Four stages can be distinguished: (1) Adhesion- van der Waals and agglomeration forces occur and powders contact with each other at random orientations. (2) Initial neck growth- the contacts grow in size,

resulting in an extensive loss of surface area. (3) Intermediate densification- the pore structure becomes rounded and densification is accomplished by volume and grain boundary diffusion. (4) Final rearrangement- the pores attach to the moving grain boundaries, giving the idealized final stage structure. This process is the most accurate in the case of single-phase powder sintering by solid-state diffusion. The reaction can be accelerated when larger contacting areas between the particles exist.

To promote such reaction in hard material such as AlN, a process called liquid phase sintering is commonly used[46]. In this process, an additive is introduced into the powder that will melt before the matrix, so capillary action will move the liquid into the pores. It promotes the rearrangement of the matrix into a more favorable packing arrangement. Moreover, doping can occur when the liquid spreads and the liquid element penetrates into the matrix lattice.

1.3.2 Si-doping

Basic requirements for the additive to AlN are that it's melting temperature is lower than AlN, it's atomic size should be similar to the AlN matrix and the formation energy of secondary phases during the sintering process must be small. Si_3N_4 powder is a great candidate for both additive and dopant roles for AlN powder. The melting temperature is 1900^{o}C, which is lower than AlN. The atomic radius of Si is very similar to that of Al. Si-accommodating defects such as Si_{Al} and Si_{Al}-V_{Al} have small formation energies so that these are very favorable defects in AlN. Si induces n-type conductivity, and affects the structural and optical properties of AlN[40, 44, 47-49].

1.3.3 Previous studies

The group of Prof. Hirosaki at NIMS has developed a high efficiency blue AlN phosphor

by co-doping AlN with Si and Eu [50-53]. Dierre et al. have reported the luminescence properties of Eu-doped and Si-Eu co-doped AlN, as shown in Figure 1-5 [50]. The CL spectra (Figure1-5 (a)) shows that the blue emission at 470 nm, attributed to Eu^{2+} in AlN, has significantly improved by co-doping with Si. Before Si co-doping, the 550nm emission, attributed to Eu-secondary phase, is strong at the grain boundaries of AlN particles (Figure 1-5 (b)). On the other hand, after Si co-doping, the 470nm emission is uniformly distributed along the particles (Figure 1-5 (c)). This results indicated that Si-co doping plays a key role in an Eu incorporation into AlN. Takeda et al. have found that Si improved the solubility of Eu in AlN by matching up with new-layered structure[51, 52]. Afterward, Dierre et al. have reported that in the proper Si co-doping condition, particles have grown rapidly with the highest luminescence intensity[53]. There is no doubt that Si has impact on the structural and luminescence properties of AlN powder. Therefore, understanding the effects of Si doping on the AlN powder and finding a possibility of high-efficiency AlN phosphors are important.

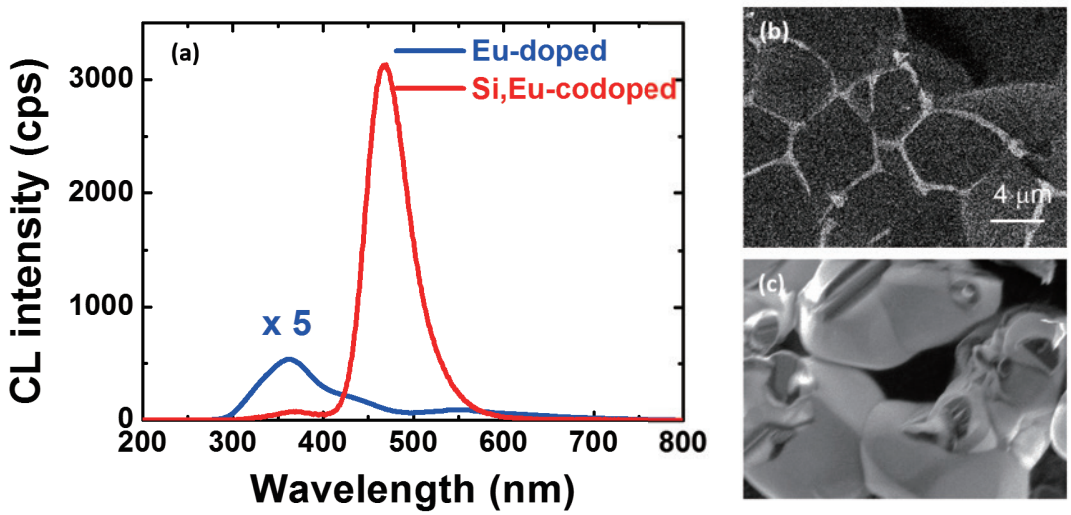

Figure 1-5. *Cathodoluminescence (CL) spectra for AlN:Eu undoped and doped with 2.9at.% Si from Si_3N_4. CL images of 550nm emissions of Si-undoped AlN:Eu (b), and 470nm emissions of AlN:Eu doped with 2.9% Si from Si_3N_4 (c).* [50]

1.4 Objective of this thesis

This thesis is mainly concerned the effects of Si-doping on the AlN particles to improve its optical properties. For this purpose, Si_3N_4 additive will be systemically doped into AlN powder by sintering method under different conditions, and the influence of Si on the properties of AlN powder with respect to the following objectives is investigated:

I. Find the best conditions of Si-doping for AlN sintering

II. Understand the role of Si on the AlN defects and the blue-UV luminescence origin of AlN

III. Clarify the sintering mechanism of Si-doped AlN powders

1.4.1. Thesis outline

Following the introduction chapter, Chapter 2 introduces the experimental procedures and fundamentals of sintering and the measurement techniques. Chapter 3 to Chapter 5 are closely connected to each other, The most commonly found different effects of Si on the AlN particles are analyzed with macro-measurement techniques depending on the doping concentration. Chapter 3 describes the effects of sintering temperature, duration and Si-doping on the structural properties of AlN particles. Powders are investigated by scanning electron microscope (SEM) and X-ray diffraction (XRD). Chapter 4 discusses the variation of chemical components and the structural properties caused by Si-doping. Inductively coupled plasma-optical emission spectrometry (ICP-OES), thermal evolution methods, X-ray photoelectron spectroscopy (XPS) and XRD were used. Chapter 5 discusses the evolution of defects and luminescence properties with Si-doping concentration by Electron Spin Resonance (ESR) and Cathodoluminescence (CL). Throughout these results, we also clarify the type of defects as well as origin of blue-UV emissions of Si-doped AlN powders.

Chapter 6 describes the cross sectional CL and Electron Probe Micro Analyzer (EPMA) measurement, which confirmed the model of sintering.

Chapter 7 summarizes this thesis. Some perspectives for possible further research are presented.

Chapter 2: Experimental procedures

This chapter describes the experimental procedures. The powder synthesis, sample preparations and the characterization techniques used in this research are presented.

2.1. Powder synthesis

We have sintered series of Si-doped AlN powders with different growth conditions. Among synthesis methods, we used two pressure-assisted sintering methods, gas pressure sintering (GPS) and hot isostatic pressing (HIP). They are able to prevent nitrogen evaporation in the high temperature.

2.1.1. AlN, Si_3N_4 powders

High-purity AlN and α-Si_3N_4 raw powders were used as a starting material, properties of which are summarized in table below (Table 2-1)

Table 2-1. *Characteristics of AlN and α-Si_3N_4 raw powders.*

Grade	AlN[54]	α-Si_3N_4[55]
Specific surface area (m^2/g)	3.27～3.47	9~13
Mean Particle Diameter (um)	0.96～1.07	0.5
Impurity	0 (wt%) 0.79～0.88 C (ppm) 220～320 Ca (ppm) 10～22 Si (ppm) 9～13 Fe (ppm) 2～9	O (wt%) < 2.0% C (wt%) < 0.2% Cl (ppm) < 100 Fe (ppm) < 100 Al, Ca (ppm) < 50

Both powders exhibit high qualities, however some negligible amounts of impurities, mainly originated from manufacturing procedures can still be detected.

2.1.2. Furnace schematics

Nitride-reactions generally require higher temperature in a N_2 or NH_3 gas pressure. The nitrogen molecule shows high stability than oxygen, its enthalpy of dissociation is 226 kcal/mol, about two times higher than the oxygen molecule[56]. Gas pressure sintering (GPS) and Hot Isostatic Pressing (HIP) processes are standard pressure-assisted methods to synthesize the hard AlN powder.

- Gas pressure sintering (GPS)

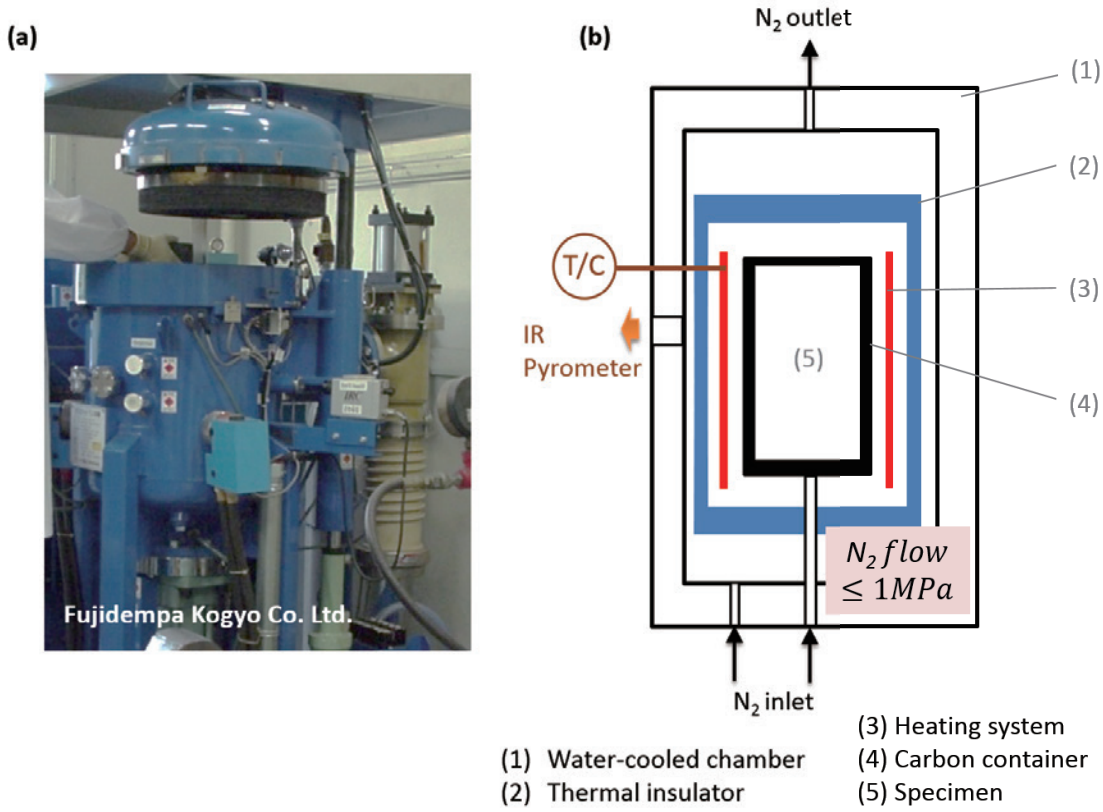

Figure 2-1. *(a) A photograph of the furnace and (b) GPS furnace schematics.*

GPS is a commonly used technique for high temperature sintering for ceramic materials, such as fluorescent, metal powders, carbon materials and quartz glass under ordinary pressure[57]. A photograph and schematics of the GPS furnace are shown in Figure 2-1. The furnace is equipped in graphite heaters that work on the side walls. Thermocouple and IR pyrometer monitor the temperature inside the furnace. Thermal insulator mantel protects the walls of the pressure chamber from high temperatures. Samples are placed on the carbon container and a N_2 or Ar gas continuously flows through in the chamber with constant pressure during sintering. The maximum temperature and pressure are 2300°C and 1 MPa respectively.

-Hot Isostatic Pressing (HIP)

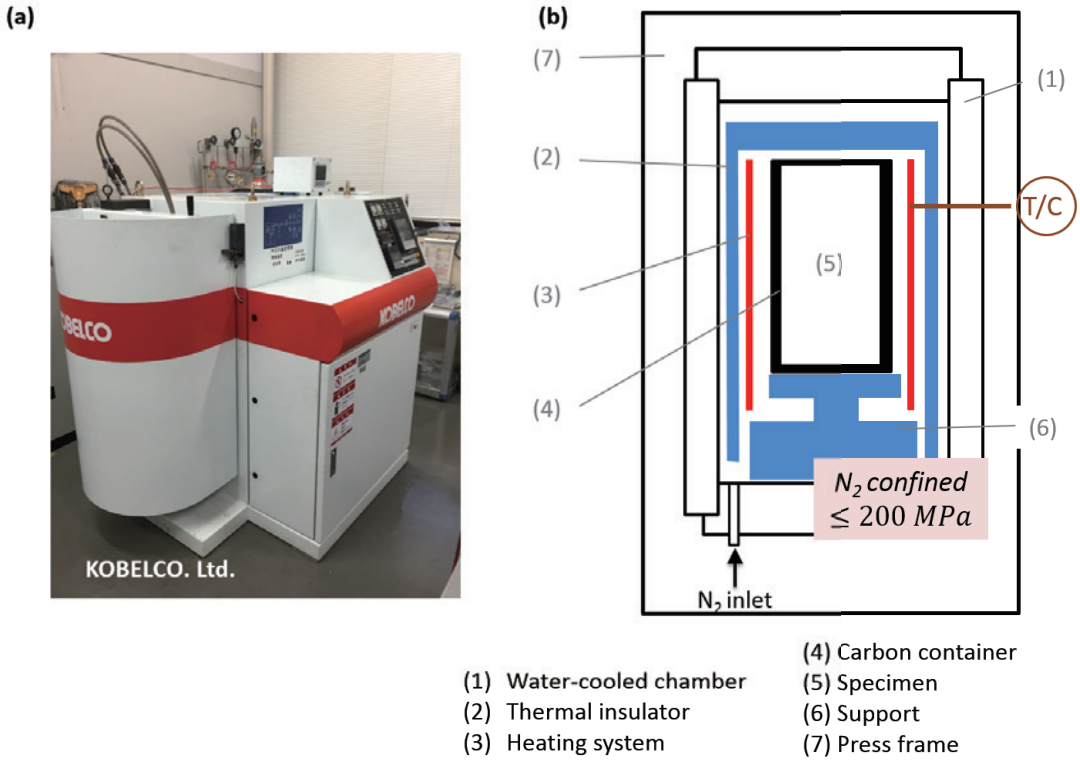

Figure 2-2. *(a) A photograph of the furnace and (b) HIP furnace schematics.*

HIP is a sintering process used to increase the density of ceramics materials without pores by applying isostatic pressure in the sample with high temperature[58]. Figure 2-2 is the schematic image and a photograph of the HIP furnace. Carbon container, heater, insulator and water-cooled chamber are similar with GPS furnace, but the high temperature furnace is enclosed in a press frame, which allows to applying higher pressure. The inert gas is used within the pressure vessel to ensure that the pressure is uniformly applied from all sides. The inert nature of the gas also assists in reducing oxidation effects. The maximum temperature is 2500°C and isostatic pressure is 200 MPa.

2.1.3. Sintering procedure

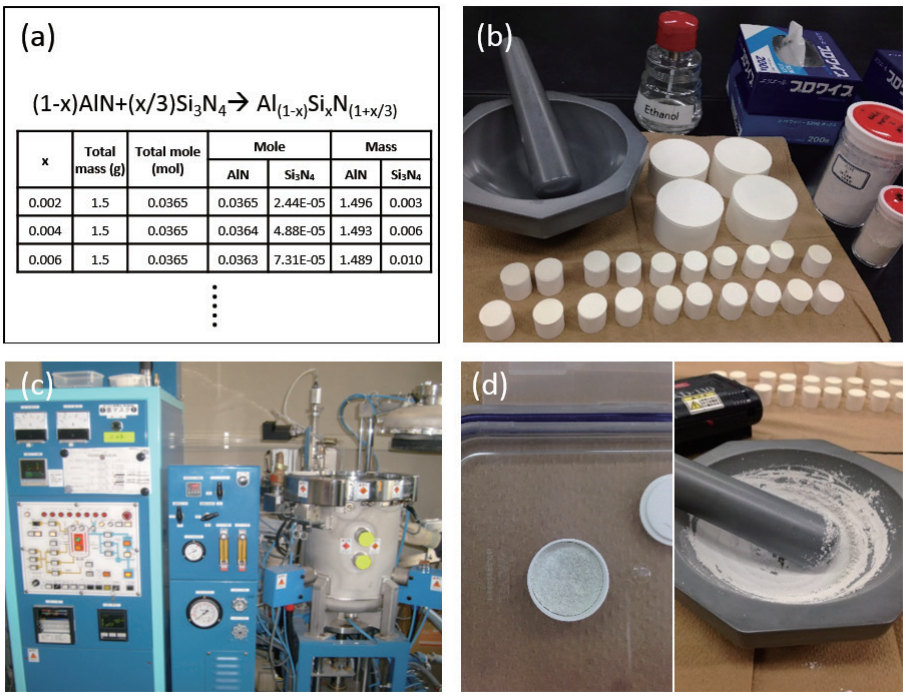

Figure 2-3. *(a) Determination of the starting powders, weight and sintering conditions. (b) Mixing of the raw powders (c) Sintering using GPS furnace (d) Sintered powders before and after crushing.*

Powder synthesis step is shown in Figure 2.3. A total of 1.5g of AlN and Si_3N_4 raw powders were weighed and hand-mixed in an agate mortar according to the composition of $Al_{1-x}Si_xN_{1+x/3}$. The designed atomic concentration of Si, *x*, was varied from 0 to 0.04. The mixed powders were put into BN crucibles, and then fired in the GPS or HIP furnaces. Most experiments were done using GPS furnace, excluding experiments from Annex 2 that were done using HIP furnace. Firstly, to investigate the growth time dependence, the holding time were varied for 2, 4, and 8 h under a graphite heater at 1950 ^oC under N_2 0.92MPa in the GPS furnace. Secondly, to investigate the growth temperature dependence, the holding temperatures are varied for 1750, 1950, and 2050 ^oC during 4h N_2 0.92 MPa by the GPS furnace. Finally, in Annex 2, to compare the GPS with HIP method, HIP process is conducted at 1950 ^oC for 4h. A nitrogen gas pressure is kept at 150 MPa. After firing, the sintered are crushed well in an agate mortar by hand until getting fine particles. Produced specimens were subjected to various characterization.

2.2. Characterizations

Structural, chemical, electrical and optical properties of produced samples have been investigated by various techniques, described below.

2.2.1. Structural analysis

The morphologies, phase and atomic structure of Si-doped AlN powders were investigated by scanning electron microscope (SEM: Hitachi, S4300), X-ray diffraction (XRD: Smart Lab, Rigaku) and transmission electron microscopy (TEM: JEOL, 3100).

- Electron Microscope

When an electron with 0~30 keV energy impinges the target sample, it suffers elastic or inelastic scattering and creates various responses, as shown in Figure 2-4. Depending on the properties to investigate, we can select the response signals and determine the characterization method. Conventional scanning electron microscope (SEM) uses the secondary electrons and backscattered electrons to reveal surface morphology[59]. Transmission electron microscopy (TEM) uses the transmitted electrons through the specimen to obtain the structural information about nano-sized, namely, crystal structure, orientation and defects, etc. In this study, SEM and TEM were operated at 5kV and 300kV, respectively.

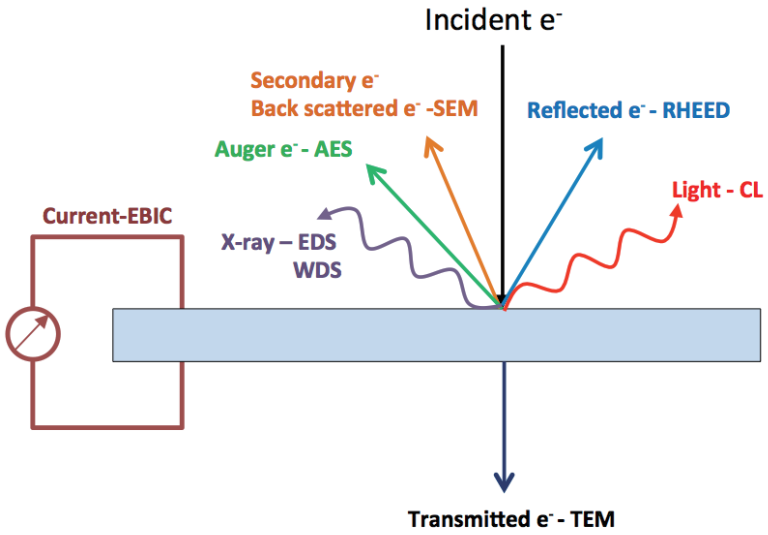

Figure 2-4. *Different type of the signals produced by an electron injection.*

- X-ray diffraction (XRD)

Powder is used to identify the unknown phases in the sintered powder by matching the peak positions with those of a standard sample, or reference data. When the powder contains different phases, the diffraction peaks consist of those from different origins. Automatic assignment software is helpful to identify them. Internal strain of the powder can be also identified with analyzing the peak shift or a profile change. The shift of each peak may be caused by a strain, which can be calculated by Bragg's low[60]. Generally, a strain variation in a polycrystalline sample may cause a peak broadening. For actual measurement, we used CuKα radiation (λ = 1.5406 Å). The obtained diffraction patterns were identified by ICDD database. The samples were prepared by mixing with Si for reducing technical errors.

2.2.2. Chemical analysis

The concentration of Si-doped AlN powders were investigated by electron probe micro analyzer (EPMA, JEOL, JXA-6500F), inductively coupled plasma-optical emission spectrometry (ICP-OES, SII Nanotechnology, SPS3520UV-DD) and thermal evolution methods (LECO, TC-436). A X-ray photoelectron spectroscopy (XPS, Ulvac-PHI Inc., PHI. Quantera) was used to analysis the electric state of each component.

- Electron Probe Micro Analyzer (EPMA)

EPMA is an instrument to analyze the chemical composition of the specimen. It measures the X-rays photon emitted from the sample as the results of electron bombardment. Each material from the sample will produce the characteristic X-ray energy, ranging in energy from 0.1~15 keV that the electron microprobe uses to identify and quantify the elements. Contrary to the SEM and TEM methods (~pA), it uses higher beam currency (~nA) and longer time measurement. EPMA-EDS is used for the determination of the surface element from 10 to 1000 nm as a fast speed, while EPMA-WDS is for the characterization of the surface elements in the monolayer range. WDS is a much more sensitive than EDS and it enables the quantification much more accurately[61]. For experimental set up, the accelerating voltage was 10 kV, the beam current was fixed at 20nA. Al, N, Si, O components were detected by WDS detector. The measurements have been done at room temperature.

- X-ray Photoelectron Spectroscopy (XPS)

XPS is a surface sensitive technique to measure the chemical composition as well as the electrical state of the components. The XPS spectra can be obtained by irradiating with the soft x-ray (200~1500 eV) while simultaneously measuring the binding energy of photoelectrons

from 10 nm of a sample. Since the binding energy of each atom is an inherent factor, the electron state of the desired atom in the surface region can be studied[62]. We used X-ray source of aluminum with Kα=1486.6, and the spectrometer was calibrated to the C-1s peak at 285.0 eV.

- Inductively Coupled Plasma-Optical Emission Spectrometry (ICP-OES)

ICP-OES is a technique to obtain chemical component of the specimen. It measures the wavelength of light from the electron in the ions excited by induced coupled plasma. We can identify the elements and the detailed concentration of those elements in the sample by measuring the wavelength and amount of light emitted by the sample. The solid samples require extraction or acid digestion, so that the sample solution is converted to an aerosol and directed into the plasma channel[63]. We have used digestion method for Si-doped AlN specimens. The powders were dispersed into the boracic acid and then mixed with hydrochloric acid and distilled water.

- Thermal Evolution Methods

Thermal evolution methods are used to determine light elements such as H, N, O, C, and S in the material. The sample is subjected to heating, combustion or fusion to quantify the chemical composition of the material, and then detected by infrared detector or thermal conductivity detector[64]. For Si-AlN sample, O was converted to carbon dioxide and measured by IR absorbance. Nitrogen gas can be quantified by using the thermal conductivity detector.

2.2.3. Defects analysis

- Electron Spin Resonance (ESR)

The presence of paramagnetic point defects in AlN crystal can be detected by electron spin resonance (ESR) technique. ESR measurements were performed with X-band spectrometer (JEOL, JES-FA200) using a cryostat (JEOL, ES-CT470).

Principle

ESR is a resonant absorption of microwave by unpaired electrons in magnetic field. Thus, the characteristics of unpaired electrons as well as their concentration can be elucidated. Figure 2-5 (a) shows a basic principle for electron spin resonance. When an unpaired electron is placed within an applied magnetic field, B_o, the two possible spin states of the electron have different energies as a result of the Zeeman effects. These states are labeled by the projection of the electron spin, M_s, on the direction of the magnetic fields, where M_s=-1/2 is the parallel state, and M_s=+1/2 is the antiparallel state. The energy states of the electron can be defined as[65]:

$$\mathrm{E} = g\mu_\mathrm{b}\mathrm{B_o}\mathrm{M_s} = \pm\frac{1}{2}g\mu_\mathrm{b}\mathrm{B_o} \quad (2\text{-}1)$$

Where g is a dimensionless constant that determines the magnetic moment, μ_b the Bohr magnetron, B_o the magnetic field, M_s the electron spin quantum number. The energy difference between the two spin states increases lineally with magnetic field strength. When this difference corresponds to the applied microwave power, the resonant absorption of radiation is observed.

$$h\nu = g\mu_b B_o \quad (2\text{-}2)$$

Unpaired electrons can exist in semiconductor crystals. Such electrons may be localized in a vicinity of point defects such as impurity atoms or native defects (deep centers). Or alternately they exist as highly delocalized electrons in conduction or impurity bands (shallow

impurities). It may interact with lattice vibrations (phonons). Thus, by analyzing the resonance lines, it is possible to determine the chemical nature of magnetic defects, their charge state and local symmetry of the occupied lattice site, and their positions and angular dependencies[66].

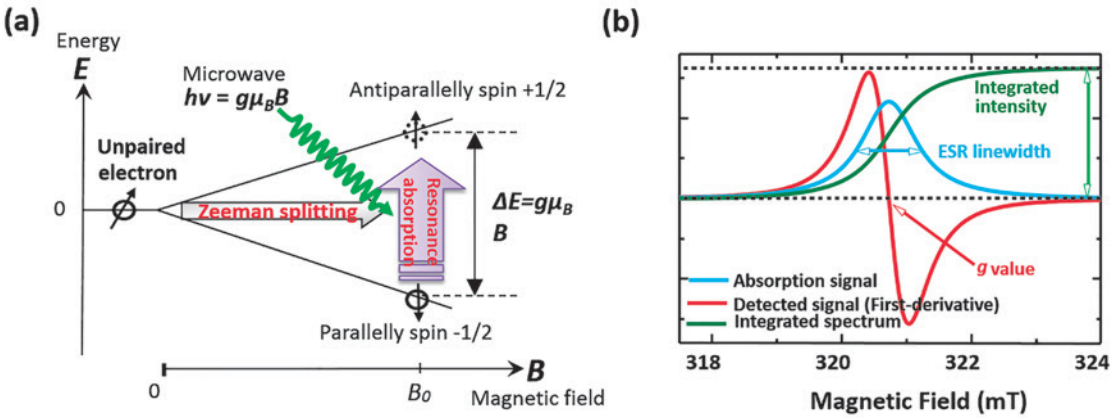

Figure 2-5. *(a) Basic principle of ESR (b) Resulting spectra.*

Typical in the absorbed signal is shown as the blue line on Figure 2-5 (b). Since the first derivative curve has much better appearance than the absorption curve, the ESR signal is usually presented as the first derivative line (red line). The maximum absorption corresponds to the point where the spectrum passes through zero. The 3 important factors in ESR signal are (1) g-value, (2) Integrated intensity (3) line width and (4) line shape.

(1) *g*-value

The effective g-value (center of the ESR signal) is determined by the microwave frequency and magnetic field as,

$$g = \frac{hv}{\mu_b B_o} \tag{2-3}$$

This value is proportional to the spin orbital coupling constant. If the electron is

completely free from the orbital effects, it is a free electron and g_e=2.0023. The magnitude of the spin-orbital coupling depends on the size of the nucleus containing the unpaired electron. Therefore, most of free radical having a small contribution from spin-orbital coupling produce g values closed to g_e, while the electrons near the transition metals are significantly different from g_e. In general, the g values of the semiconductor are represented as[38]

$$g = g_e + \Delta g \tag{2.4}$$

If $\Delta g < 0$, the chemical origin could be considered as donor-type, while $\Delta g > 0$ to acceptor type. And if the Δg is larger, it indicates that the defect in deep centers with localized wavefunction.

(2) Integrated intensity

The integrated intensity of the spectrum is proportional to the concentration of unpaired electrons in the sample, namely the density of corresponding paramagnetic defects.

(3) Line width

The electron with lifetime τ gives the width proportional to 1/ τ. When the lattice contains higher concentration of the defects in which contained localized electrons, the large line width of that broad resonance may be seen due to the unresolved hyperfine interaction of the electron spin from defects, or surrounding ligand. On the other hands, sharp signals may appear due to the existence of the delocalized electrons in the shallow band[67].

(4) Line shape

Spin-lattice relaxation: If the anti-parallel spin-state electron relaxes to parallel spin state via phonon emission, the process is categorized as a spin-lattice relaxation. This absorption

wave becomes Lorentzian.

-Spin-spin relaxation: When the relaxation takes place between electron or nuclear spins, it categories spin-spin relaxation. This relaxation originates from magnetic dipole interaction, so that the absorption curve becomes Gaussian.

Instruments

Shown in figure 2-6 is a block diagram for a typical EPR spectrometer. The radiation source usually used is called a klystron. Klystrons are vacuum tubes known as stable high power microwave sources that have low-noise characteristics. Most of EPR spectrometers operate with a microwave of at 9.5 GHz (X-band). The microwave is guided to the specimen via circulator continuously. The sample is mounted in a resonant cavity, which admits microwaves through an iris. The cavity is located in the center of an electromagnet and helps to amplify the weak signal from the sample. The modulation coil is capable of providing large modulation amplitudes. Microwaves are reflected from the cavity are routed to the diode detector. When the magnetic field is swept in a certain range, radiation is absorbed by the sample, and a small decrease of microwave intensity should be observed.

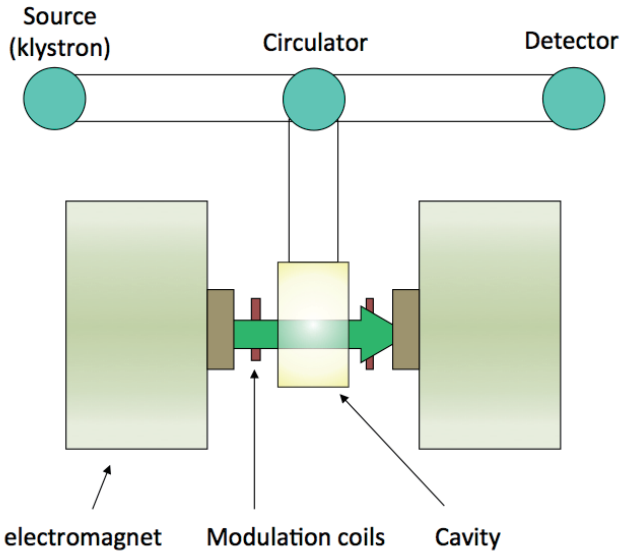

Figure 2-6. *A diagram of ESR spectroscopy.*

Experimental conditions

Each of Si-doped AlN powders was weighted to 100mg and put it on a quartz sample holder, and then placed in the center of magnetic fields. It measures under room temperature without light excitation. The applied magnetic field was in the range from 310 to 360 mT. After plotting the signals, the absolute magnitudes of the g-value, ESR linewidth, and the number of spins were calibrated using a Mn^{2+} standard sample.

2.2.4. Optical analysis

The optical properties of Si-doped AlN powders were determined by the cathodoluminescence system (CL: Horiba, MP32S/M) in SEM (Hitachi S4300)

Principle

CL is a phenomenon in which electrons irradiating on a luminescent material cause the emission of photons (Figure 2-4).

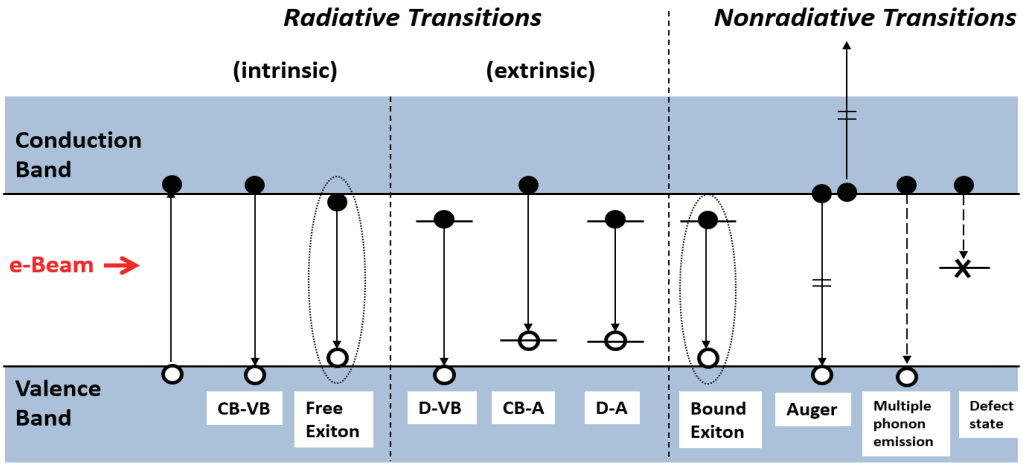

Figure 2-7. *Schematic image of recombination of electron hole pairs.*

Figure 2-7 shows the schematic image of recombination of electron hole pairs in the band gap. When the incident electrons impinge onto a semiconductor, the electrons are excited from the valence band into the conduction band, leaving a hole behind. Excited electrons and holes may directly recombine or diffuse and are trapped by impurity/defect levels, and then recombine. The process accompanied with photon emission is called radiative recombination. On the other hand, when an electron recombines via Auger process or multi phonon emission, it is called

non-radiative recombination. Depending on the material, its purity and defects state, the energy of the emitted photon is different. Thus, it is possible to get the information of band gap, impurity level and doping concentration, and defects of materials[68, 69].

The electron irradiation allows to excite the most of the luminescence centers in the material. Moreover, the electron beam scanning can reveal the luminescence distribution spatially and also in depth. CL is also applicable in the investigation of the luminescence stability under stress. Additionally, the incident electrons can generate not only the CL signal but also various signals, such as reflected electron, Auger or X-ray, which provide different information on the materials. Thus, the structural, chemical or electrical properties can also be obtained simultaneously. The combination of these techniques with CL results in a better understanding of the origin of the luminescence.

-Instruments

CL investigations can be performed by means of different types of e-beam sources. The most common system is SEM-CL, which is the system that we are going to discuss. As seen in the figure 2-8, CL system is composed of an electron source (SEM), a light collector (optical fiber and monochromator) and a detection system. The light from the sample is a result of electron irradiation and is collected via ellipsoidal mirror and optical fiber cable. It is adjusted by slit and dispersed onto monochromator grating and detection system, simultaneously. The detection system consists of a charge-coupled device (CCD) and a photomultiplier tube (PMT), which are for fast spectral acquisition and high resolution spectral acquisition, respectively. CCD can realize parallel signal recording, which is used for spectral acquisition. PMT corresponds to a spectral detection, which is used for CL imaging[70].

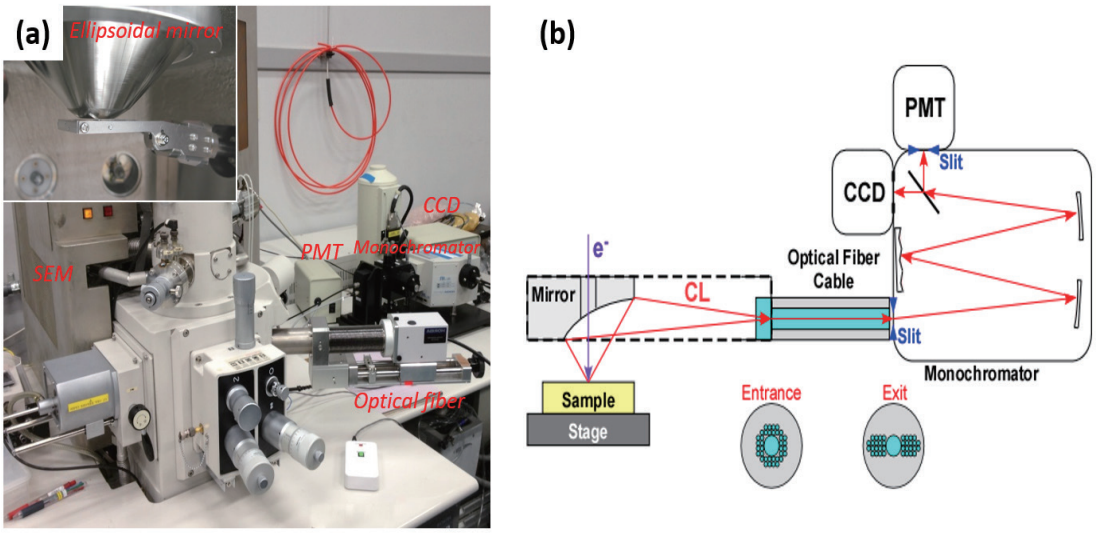

Figure 2-8. *(a) Photograph of the SEM-CL system (b) Schematic image of light detection system.*

-Experimental conditions

The accelerating voltage was 5 kV, which corresponds to an electron penetration depth of 360 nm according to the Kanaya-Okayama model. The beam current was fixed at 100 pA. All CL measurements are performed at room temperature.

2.3. Summary

In this thesis, CL has been intensively used as well as other techniques, such as ESR, TEM or EDS, in order to correlate the optical properties with the structural/chemical/electrical properties. By using those characterization techniques, we clarify the nature on the Si-doped AlN powders as well as the defects and luminescence property.

Chapter 3: Particle growth and phase diagram of Si-doped AlN powders

The luminescence of AlN powder is mainly originated from the defects present in AlN, and we have expected that the incorporation of Si may affect them. To clarify the effect of defects and Si, we have prepared several series of Si-doped AlN powders under different sintering conditions, such as the sintering durations, temperature and Si concentrations (x). Our first concern was whether the synthesized powders are AlN phase and whether Si causes any impact. Thus, we have investigated the structural properties of Si-doped AlN powders by SEM and XRD.

3.1. Particle size and morphology with Si-doping

Figure 3-1 shows the SE images (a)~(f) and a schematic (g) of raw AlN powder (a) and Si-doped AlN powders with 0.0% (b), 0.8% (c), 1.6% (d), 2.4% (e), 4.0% (f) of Si(x) sintered at 1950℃ for 4h. Raw AlN powder exhibits granular and rounded shape. While with sintering and Si-doping, the morphology of particles has changed, varied from an asymmetric polyhedron below x=1.2%, a symmetric octahedron for 1.6%≤x≤2.8%, to an asymmetric polyhedron again above x=3.2%. The particles size has also changed with x. The particle sizes of low and high x are comparable with the initial AlN particle sizes, while particle growth of AlN is promoted at medium x with an octahedron structure.

The average particle size distribution for different x was measured using Image-pro software and is summarized in Figure 3-2. The average particle size is 0.94, 1.12, 2.80 and 1.28 μm with a standard deviation of 0.42, 0.42, 1.02 and 0.53 μm for x=0.0%, 0.4%, 1.6% and 4.0%, respectively. The x=1.6% shows the biggest size with larger deviation than the others.

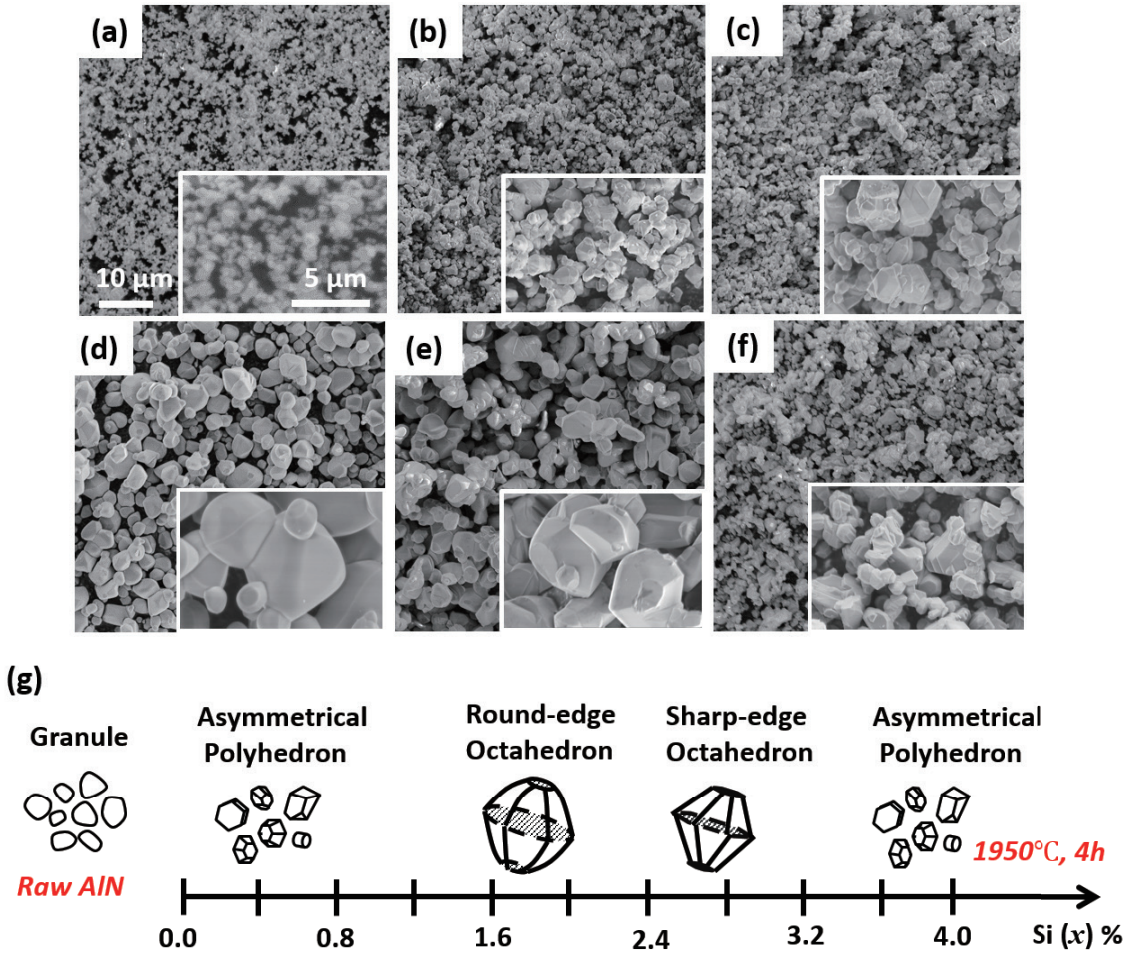

Figure 3-1. *SE images for a raw AlN powder (a) Si-doped AlN powders with 0.0% (b), 0.8% (c), 1.6% (d), 2.4% (e), 4.0% (f) of Si(x) sintered at 1950℃ for 4h, respectively. (g) Particle morphology distributions of these powders.*

The average particle size as a function of x is shown in Figure 3-3. It is rapidly increased above x=1.6% from ~1 to ~3 μm, and then decreased to ~1.5 μm again above x=3.2%. These results indicates that proper amount of Si-doping (1.6%≤x≤2.8%) has a significant impact on the crystal growth of AlN.

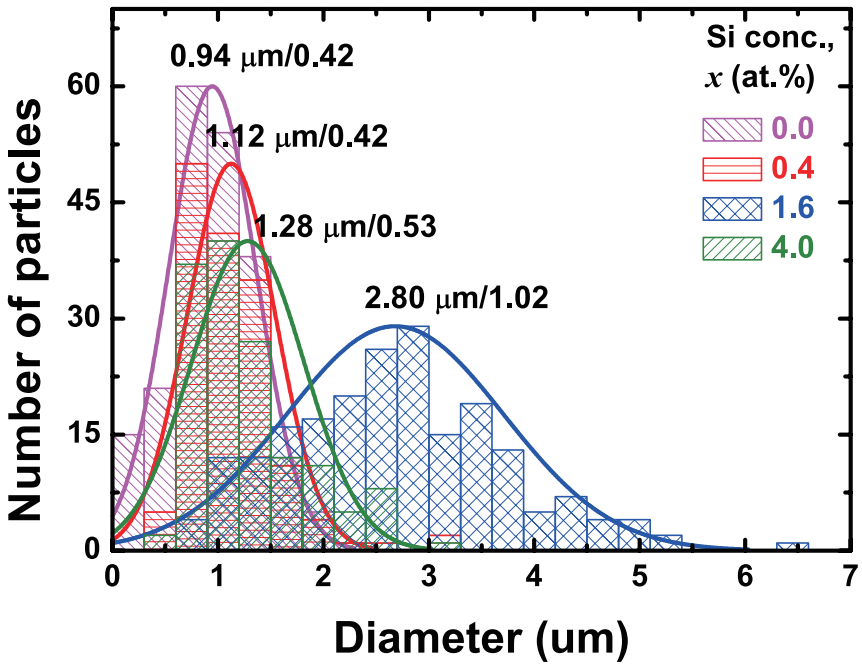

Figure 3-2. *Particle size distributions of Si-doped AlN powders with different x.*

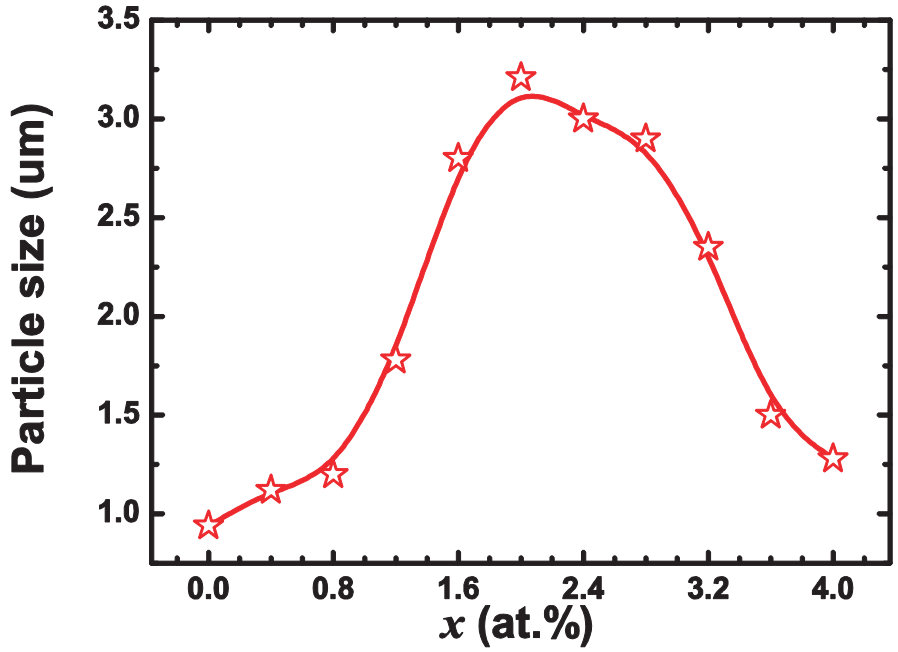

Figure 3-3. *Average particle size as a function of x.*

3.2. Diffraction patterns with Si-doping

Figure 3-4 shows XRD patterns of Si-doped AlN powders sintered at 1950°C for 4h. All the XRD peaks have been attributed to wurtzite AlN. On the other hand, a closer look reveals the existence of small shoulders at x=4.0%. It indicates the existence of polytypes. Figure 3-5 shows the magnified 002 peak profiles. The peak position and FWHM has varied with Si concentration. An inserted image shows the evolution of FWHM with Si concentration, it become the narrowest at x=1.6% and then broaden again. The FWHM is related to crystal quality of the material. Indeed, the crystal growth area shows high crystal quality of AlN. More detailed discussions about the shift of XRD peak position will continue in Chapter 4.

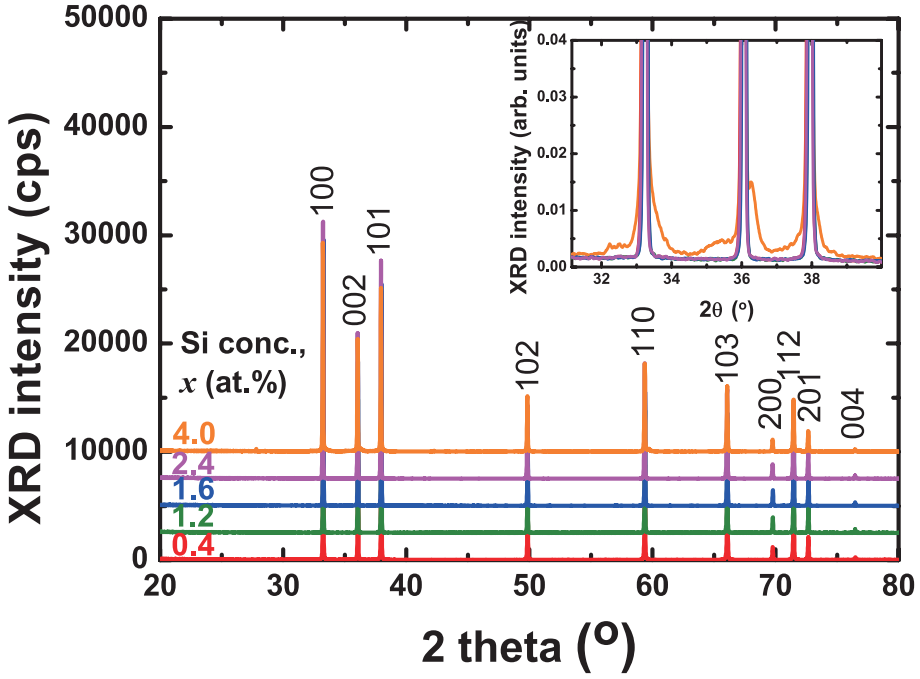

Figure 3-4. *XRD patterns of Si-doped AlN powders with different x.*

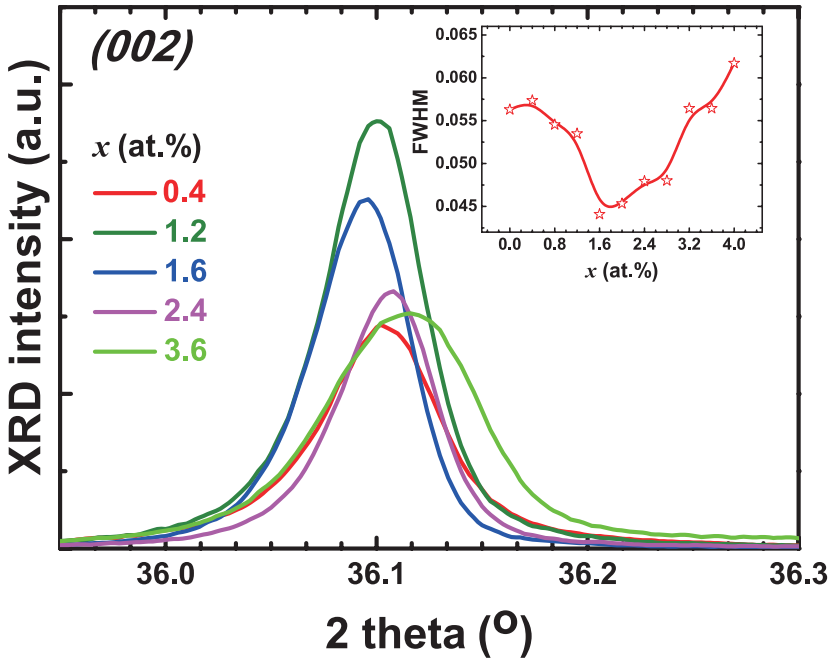

Figure 3-5. *Magnified XRD patterns of Si-doped AlN powders with different x. Inserted image is the FWHM changes as a function of x.*

3.3. Phase diagram

3.3.1 Growth time dependence

Figure 3-6 shows the diagram summarizing SEM and XRD results depending on the growth time and Si concentration, x. Without Si-doping (x=0.0%) no growth has occurred. At low Si-doping (0.4≤x≤1.2%), growth has been observed at 8h. At medium Si-doping (1.6%≤x≤2.8%), growth has started at 4h. At higher Si-doping (3.2%≤x≤4.0%), secondary phase

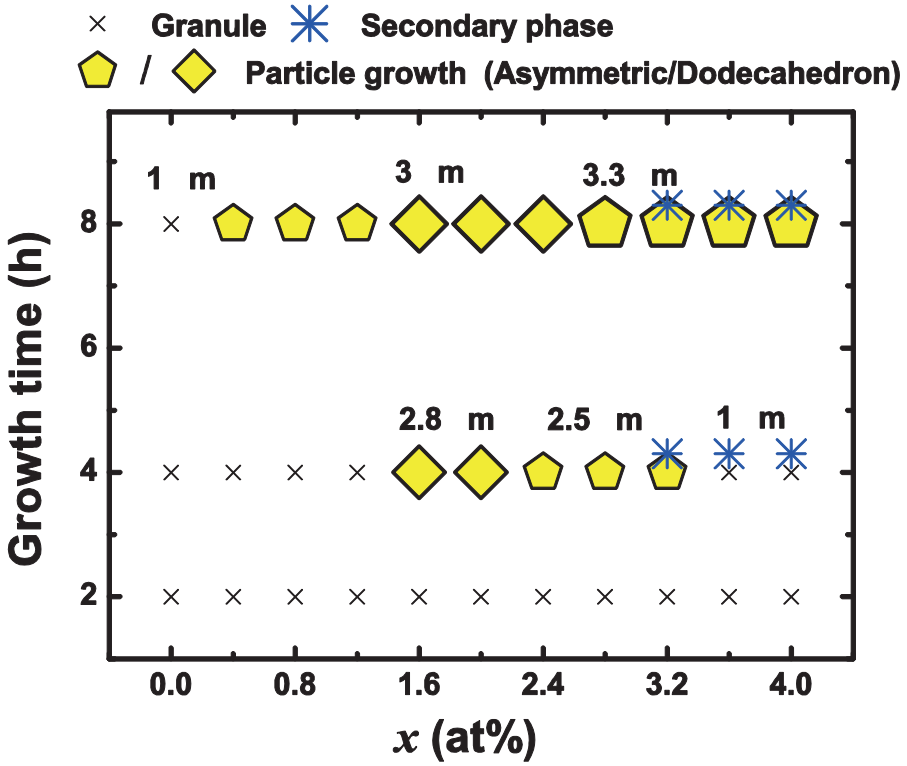

Figure 3-6. *Diagram summarizing the SEM and XRD results for Si-doped AlN powders sintered at 1950 °C with different growth time condition as a function of x. The average particle sizes are written inside.*

has started to grow and the particles sizes started decreasing for 4h. At such concentration, secondary phases have been detected by XRD. Thus, it is reasonable to deduce that the secondary phases may affect on the retarded particle growth of AlN. The diagram shows that

particle growth occurs only at certain Si concentrations. Distribution of particle size depending on the growth time is mainly due to the kinetic effect. Longer reaction time may attribute to longer diffusion distance, consequently enhances the particle agglomeration.

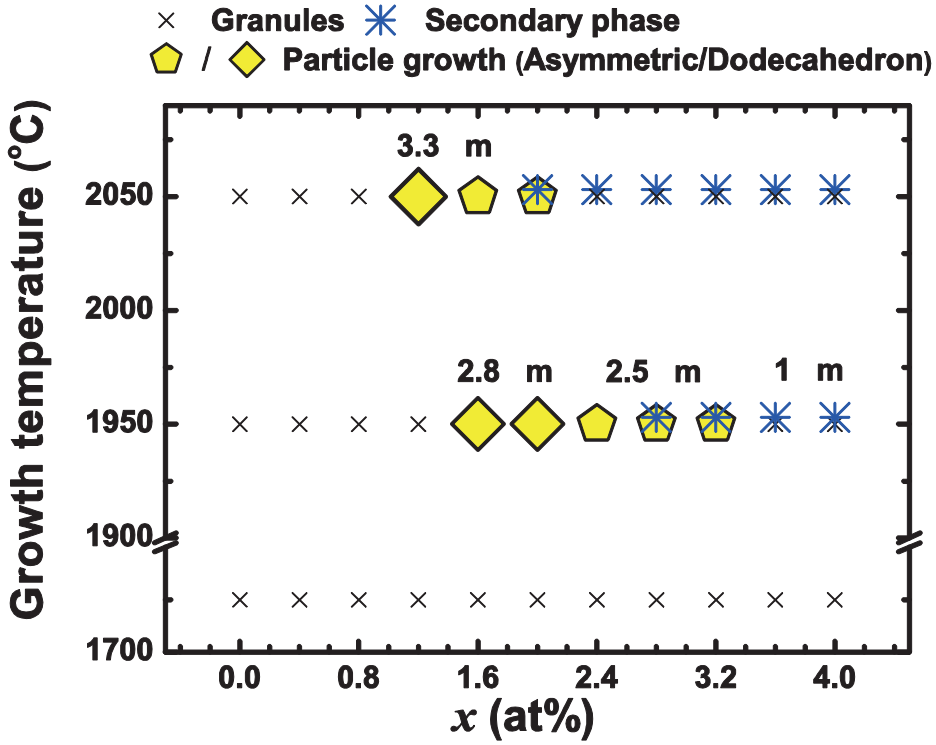

Figure 3-7. *Diagram summarizing the SEM and XRD results for Si-doped AlN powders sintered for 4h with different growth temperature condition as a function of x. The average particle sizes are written inside.*

3.3.2 Growth temperature dependence

Figure 3-7 shows the diagram summarizing SEM and XRD results depending on the growth temperature and Si-concentration, x. At 1750°C, particle growth does not take place for any Si concentration. At 2050°C, the particle growth occurs only for $1.2 \leq x \leq 2.0$ and secondary phases become dominant. It suggests that the sintering reaction occurs faster at higher temperature.

3.4. Summary

Changes in the particle size and morphology of Si-doped AlN were observed by SEM and XRD with the Si-concentration, the sintering temperature and the sintering duration. A certain amount of Si-doping have a significant effects on the particle growth and crystallinity quality of AlN powder. On the other hand, at high concentration of Si induces polytype structure, resulting in the retarded particle growth.

These results suggest that Si greatly influences the sintering of AlN. In the following, we will focus on the AlN powders sintered at 1950^{o}C and 8h since those are the samples exhibiting largest particle size, thus making the investigation easier.

Chapter 4: Chemical and structural properties of Si-doped AlN powders

In the previous chapter, we have determined that Si-doping has impact on the particle growth and crystal quality of AlN. Si seems to behave differently depending on its concentration on the AlN powder, thus it is necessary to identify its effect more deeply. For instance, we have to confirm if Si is incorporated into AlN or if it reacts as a catalyst. For such purpose, we will determine the effect of Si on the chemical components, bonding and lattice strains of AlN by ICP-OES, thermal evolution method, XPS and XRD.

4.1. Chemical compositions with Si-doping

4.1.1. O, Si composition

Figure 4-1 shows O and Si concentration in AlN powder as a function of *x* determined by thermal evolution method (O) and ICP-OES (Si). AlN powder itself natively contains O. The O concentration gradually decreases from 1.08% at *x*=0% to 0.16% at *x*=2.4%, then slightly increases to 0.18% until *x*=4.0%. The Si concentration stays almost constant at 0.08% until *x* = 1.6%, then continuously increases to 1.16% until *x*=4.0%. Interestingly, the actual Si concentration is much smaller than the designed value. It should be noted that the O and Si concentrations have inverse relationship. The O-impurity is dominant at low Si concentration, while the Si-impurity at high Si concentration. We suggest that Si initially contributes to O desorption from AlN. Namely, O may react with Si to form silicon mono-oxide (SiO). Since SiO may vaporize at 1800^{o}C[71], Si may not diffuse into AlN. After the O desorption, Si may start

to be incorporated into AlN. It can be pointed out that the medium Si concentrations (x~1.6%) contains the least impurities.

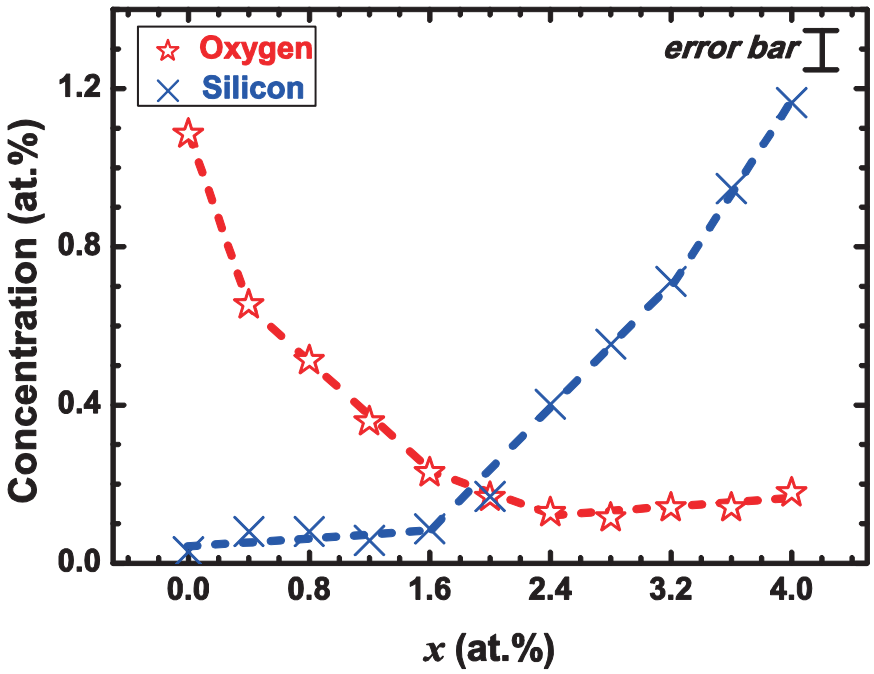

Figure 4-1. *Chemical concentration of O and Si in Si-doped AlN powder as a function of x.*

4.1.2. Al, N composition

Figure 4-2 shows the chemical composition of Al and N in AlN powders as a function of x determined by ICP-OES (Al) and thermal evolution method (N). The Al concentration slightly decreases with Si-doping, but is almost constant at 49.8% until x=1.6%. Above x=1.6, it drastically decreases to 48.5% until x=4.0%. The N concentration increases from 48.8% at x= 0% to 50.3% at x=2.4%, slightly decreases to 50.0% at x=3.2%, then increases to 50.2% until x=4.0%. It is interesting to note that the tendency of Al and N components below x=2.4% are similar to the evolution of Si and O concentration, respectively, as observed in Fig. 4-1.

Al-component was poor with Si-doping while N-component was poor when the O exists at the initial stage. These data suggest that Si may substitute Al-site, while O, N-site in AlN powder below x=2.4%. On the other hand, above x=2.4%, those relationships are not correlated. It is possible to think that the secondary phases that occurred at high x can be attributed to the uneven changes.

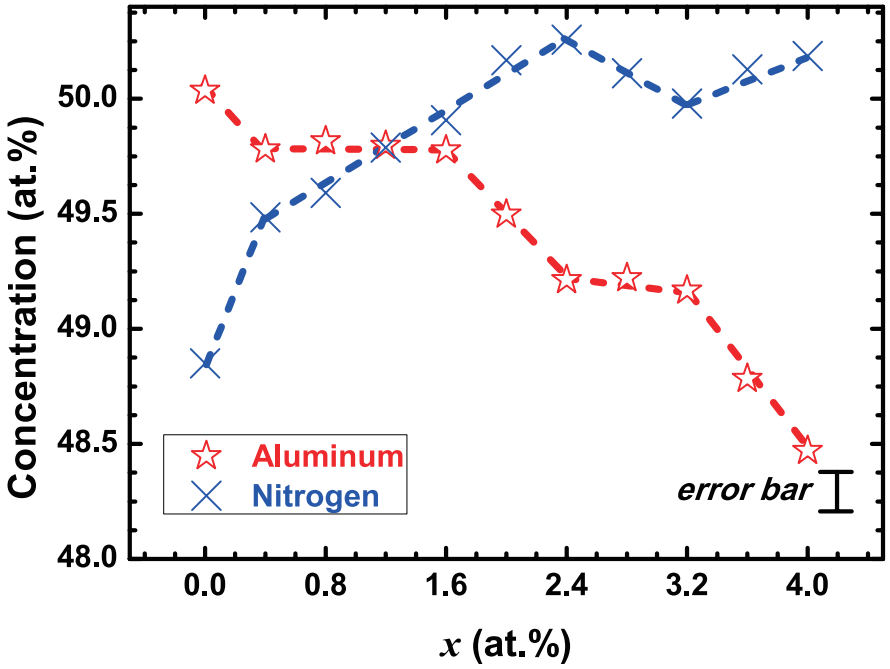

Figure 4-2. *Chemical concentration of Al and N in Si-doped AlN powder as a function of x.*

4.2. Chemical bonding with Si-doping

Figure 4-3 shows the results of XPS wide spectra for Si-doped AlN powders with *x*=0.0, 0.4, 1.6, and 4.0%. All these spectra contain peak of aluminum (Al 2p and Al 2s), nitrogen (N 1s), oxygen (O 1s), carbon (C 1s) and silicon (Si 2s, 2p). The C 1s peak may originate in the carbon tape that fixes the specimen at the holder. The most significant feature is the prominent O peak, which decreased with *x*. Si peak on the other hand increased with *x*.

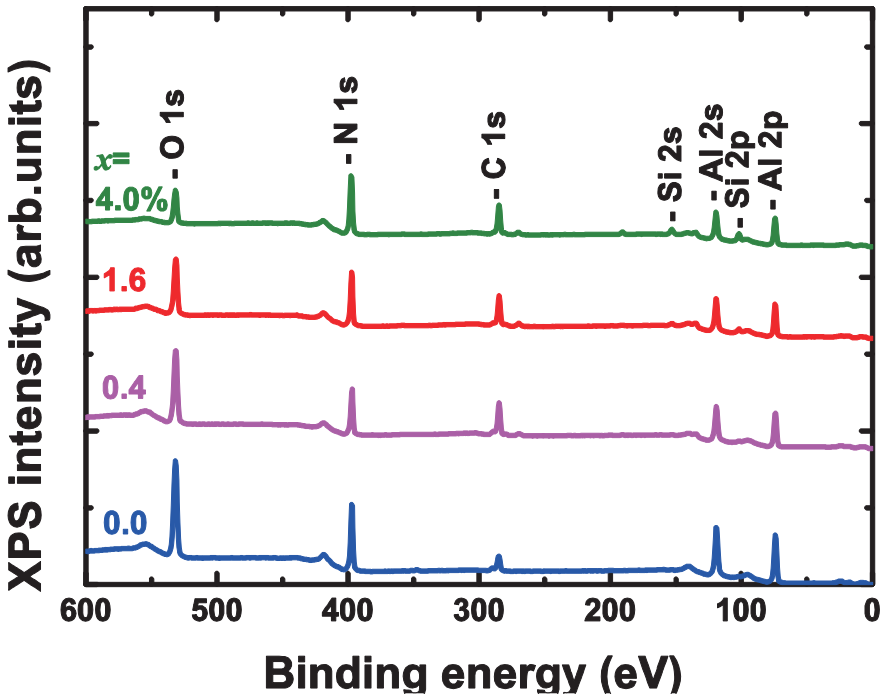

Figure 4-3. *XPS wide spectra for Si-doped AlN powders with x=0.0, 0.4, 1.6, and 4.0%.*

In order to investigate the chemical bonding, high-resolution scan was performed on the area around the peaks of Al 2p, N 1s, O 1s and Si 2p in figure 4-4.

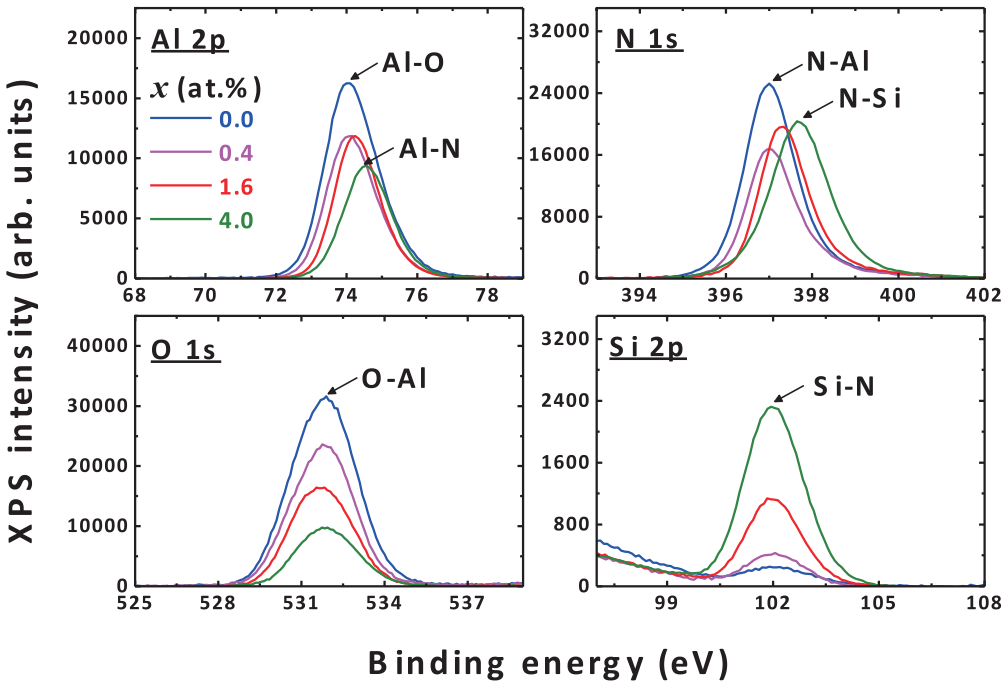

Figure 4-4. *High resolution XPS scans on the area of Al 2p, N 1s, O 1s and Si 2p peaks for Si-doped AlN powders with x=0.0, 0.4, 1.6, and 4.0%.*

The center of the Al 2p peak shifts from 74.1 (x=0.0%) to 74.6 eV (x=4.0) and the N 1s peak shifts from 397.0 (x=0.0%) to 397.7 eV (x=4.0%). On the other hand, the O 1s and Si 2p peaks are not shifted but their intensities changed. The peak of O 1s (531.8e V) decreases whereas the peak of Si 2p (102.0 eV) increases with x. A survey of the literatures reveal that the Al 2p peak with binding energy of 74.1eV is assigned to the oxidic aluminum in α-Al_2O_3[72] and the peak at 74.6eV is a nitridic aluminum in the form of AlN[73]. The binding energy of 397 eV is consistent with N 1s peak bounded to aluminum in hexagonal AlN [74], and 397.7 is near N 1s peak bounded to Si_3N_4 (398 eV)[75]. The energy shifts are caused by the changes in chemical bonding. We assume the following reaction on the surface of Si_3N_4-doped AlN particle.

(1) Al-O to Al-N bonding

$$2\mathbf{Al_2O_3}+Si_3N_4 \rightarrow 4\mathbf{AlN}+3SiO\uparrow+3/2O_2\uparrow$$

(2) N-Al to N-Si bonding

$$\mathbf{AlN}+Si_3N_4 \rightarrow \mathbf{Si_3N_4}+Al\uparrow+1/2N_2\uparrow$$

The first reaction indicates that the surface oxygen has been vaporized as SiO. The second reaction indicates that the Si is incorporated into Al-site in AlN.

4.3. Lattice constant with Si-doping

Figure 4-4 shows the variation of 100 and 002 diffraction peak positions on XRD patterns of AlN powder as a function of *x*. Both 100 and 002 peaks shift to the lower angle until *x* = 1.6%, and then to higher angle. The shift of 002 is larger than that of 100. This result shows that AlN lattice expands until *x*=1.6%, then shrinks above it. For a detail discussion, we have tried to calculate the lattice constants using this result.

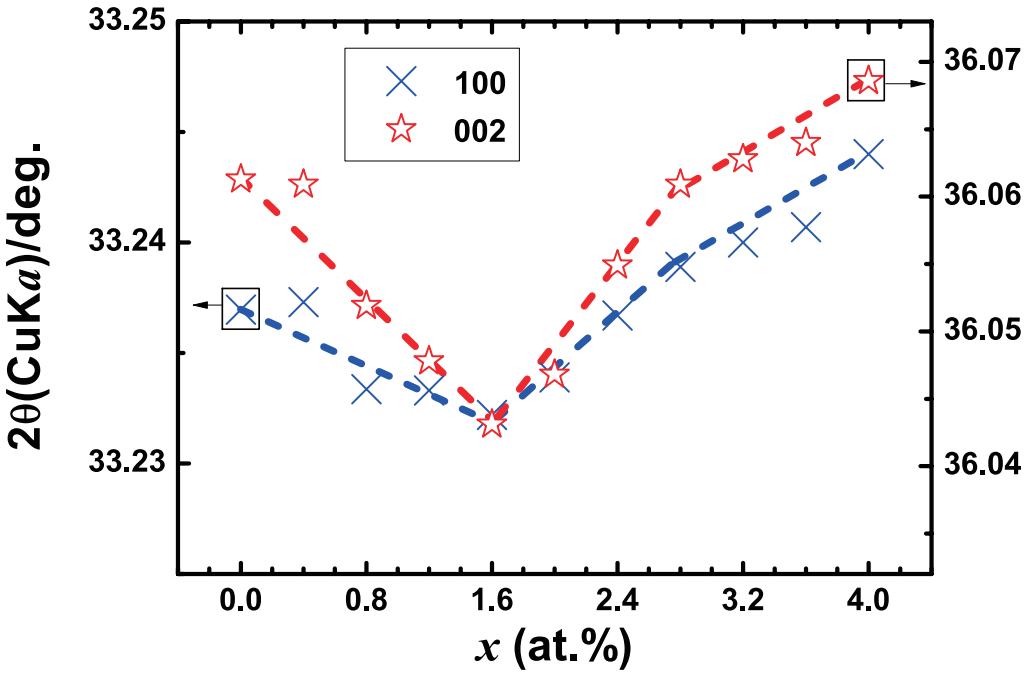

Figure 4-5. *Position shift of 100 and 002 diffraction peaks in XRD spectra as a function of x.*

The lattice spacing for all the samples was calculated using Bragg's relation[60]:

$$d = \frac{\lambda}{2sin\theta}$$

Where θ is the angle between diffracting plane and incident X-ray, λ is the wavelength of X-ray, which in our case was CuKα radiation, 1.5405 Å. The lattice parameters have been

calculated using the following expression for hexagonal system.

$$\frac{1}{d^2} = \frac{4}{3}\left(\frac{h^2 + hk + k^2}{a^2}\right) + \frac{l^2}{c^2}$$

The lattice parameters *a* and *c* calculated are plotted in Figure 4-6.

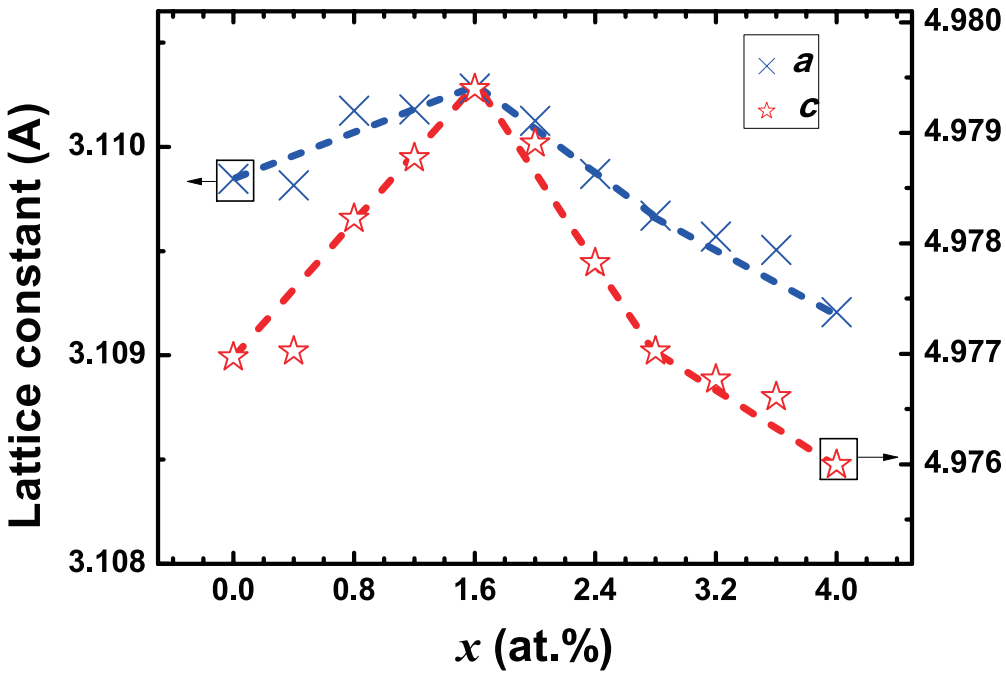

Figure 4-6. *Lattice constants of 'a' and 'c' change as a function of x.*

The lattice constants increase with respect to O-desorption below x=1.6%, and then decrease with respect to Si-incorporation above it. From XPS results, we have found that Al-O bond changes to Al-N bond, while Al-N bond changes to Si-N bond. Since the distance of Al-O bond is 1.96 Å[76], Al-N bond is 2.00 Å[77], and Si-N bond is 1.74 Å[78], it is reasonable to think that the bond shift of Al-O→ Al-N bonding may occur at lower x (x<1.6%), while the Al-N→Si-N bonding at higher x (x>1.6%). When the x is above 2.4%, the change is slightly suppressed. It is possible to think that the secondary phases that occurred at high x can be attributed to

unexpected bonding changes such as Al-Si (2.43 Å), Si-Si (2.35 Å) or Si-O (1.63 Å). Meanwhile, at x=1.6%, the lattice constant values are closest to the ideal AlN powder that are a=b=3.113 Å and c=4.9816 Å[76].

4.4. Summary

In this chapter, we have clarified the effect of Si on the chemical components, bonding and lattice constant of AlN. AlN powder contains about 1.0% Oxygen before Si-doping. With Si-doping, O-impurities are reduced by reacting with Si, and the lattice bonding has changed from Al-O to Al-N until x=1.6%. At medium Si concentrations (1.6%<x<2.4%), Si replaces Al atoms and a subsequent Si-N bond forms in AlN. On the other hand, at high Si concentrations (x>2.4%), this change has been saturated due to the formation of secondary phases.

Chapter 5: Electrical and optical properties of Si-doped AlN powders

So far, it is clear that Si-doping of AlN powder sintering has an impact on the O-desorption, particle growth and secondary phase formation depending on Si concentration. However, the potential effect on the electrical and optical properties of AlN has not been clarified yet.

In this chapter, we will determine the defects and UV emitting properties of Si-doped AlN powders. Normally, defects may induce deep levels in the band-gap and can significantly alter UV-blue emissions (3~4eV). Thus, we believe the investigation of defect evolution is helpful to understand the luminescence origins of Si-doped AlN. For this purpose, we will clarify the nature of defects and luminescence by ESR and CL.

5.1 ESR signals with Si-doping

Figure 5-1 shows the ESR signals of Si-doped AlN powder. The intensity and line-shape of ESR signals drastically change with x. It seems that there exist at least 2 different signals: a sharp and a broad signal. The sharp signal is observed at x=0% and at high x (x≥2.4%). On the other hand, the broad signal is significant at low x (x≤0.8%). The number of spin is calculated and shown in figure 5-2. It significantly decreases with Si-doping up to x=1.6% and then slightly increases at high x%. The number of spin represents the paramagnetic defects density. Thus, most of the paramagnetic defects exist at low x.

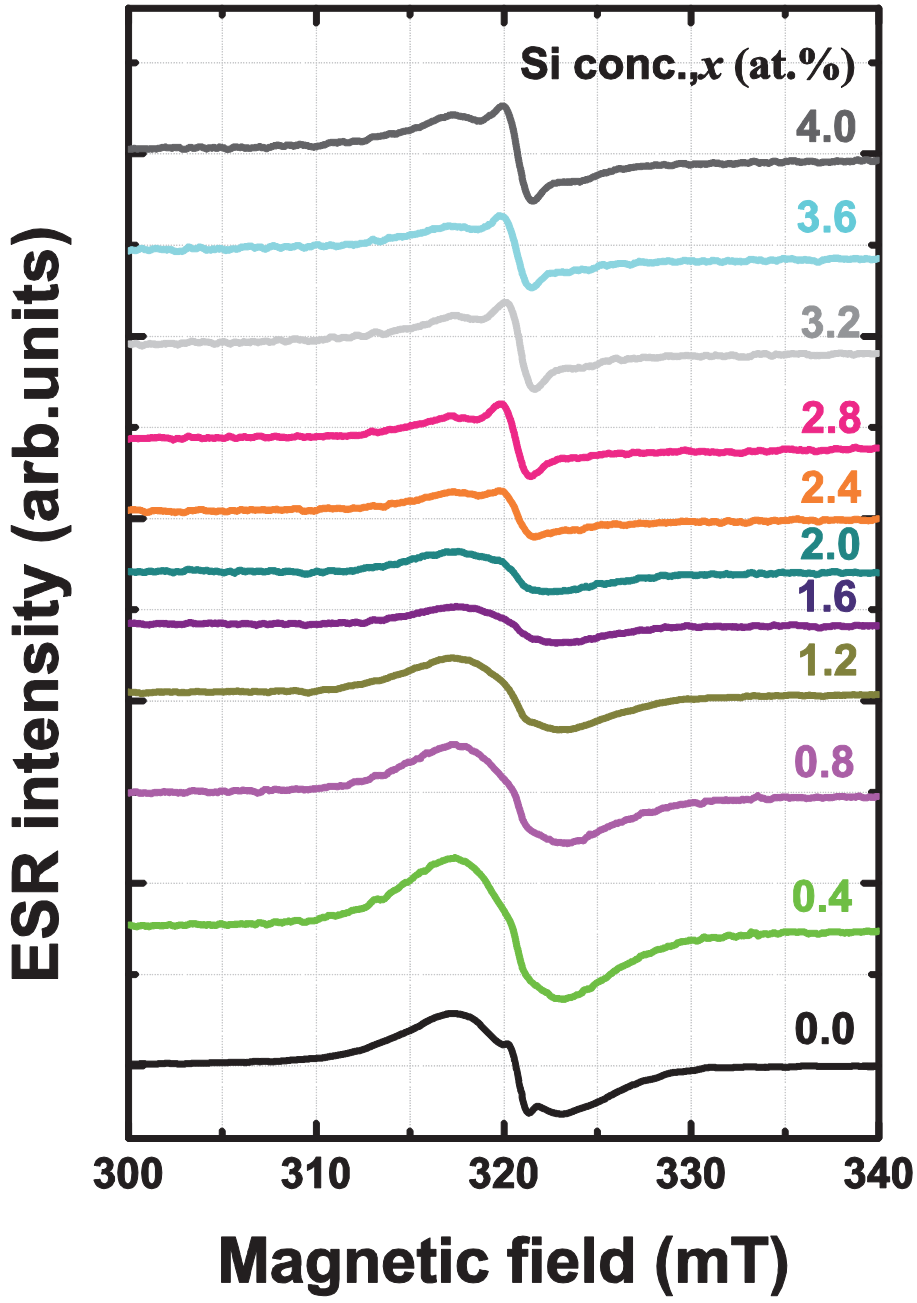

Figure 5-1. *ESR signals of Si-doped AlN powders with different variations of x.*

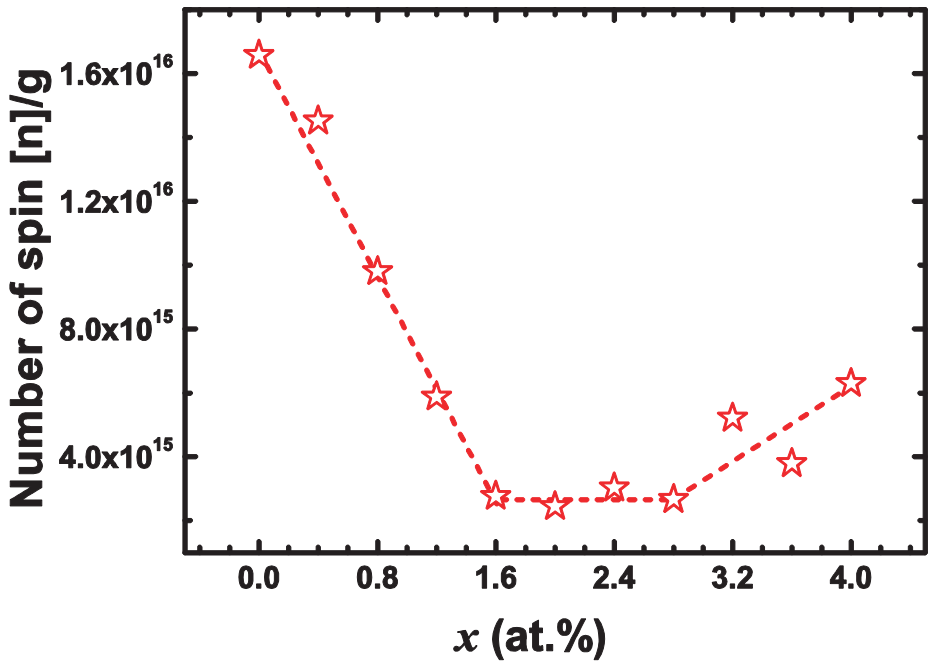

Figure 5-2. *The total number of spin of Si-doped AlN powder with function of x.*

To investigate the evolutions of the ESR signals in detail, we fitted the spectra by Lorentzian, as shown in Figure 5-3. The signals can be fitted with 3 Lorentzian curves. They are simplified to A, B and C in Table 5-1. At low x (x≤0.8%), A and B signals coexist. At the medium x (1.2≤x≤2.0), the A signal is dominant. At high x (x≥2.4%), C signal appears with B signal.

Table 5-1. *The g-value and corresponding line-width of detected ESR signals.*

Sort of content	g-value	Line-width, ΔH_{pp} (mT)
A	2.005±0.001	5.3±0.05
B	2.002±0.0001	1.2±1
C	1.988±0.001	15±0.1

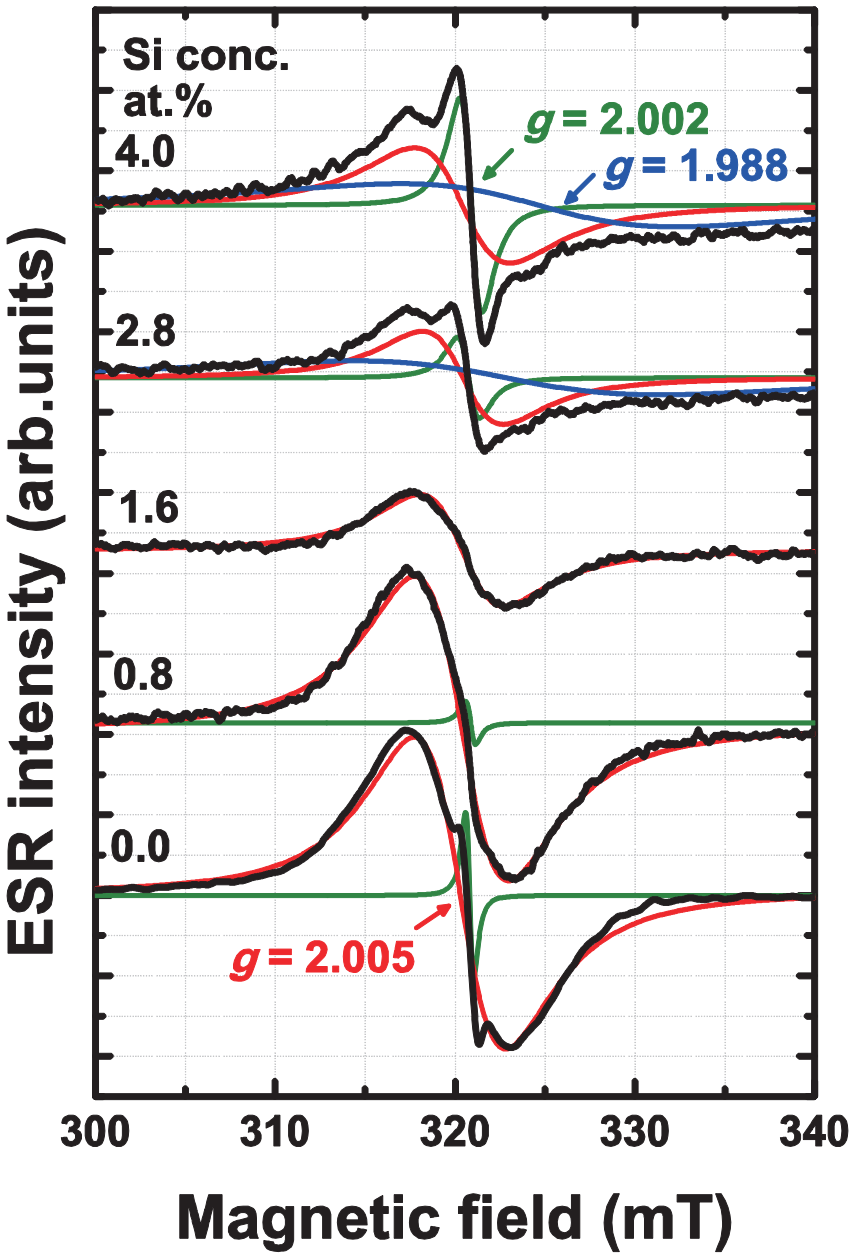

Figure 5-3. *ESR signals (black) with fitted signals (colored) of Si-doped AlN powders.*

For the detailed discussion, the number of spins of each fitted signal was evaluated as a function of x in Figure 5-4. The A signal decreases until x=1.6%, then slightly increases. The B signal is small at low x, almost disappears at the medium x, and then appears again at high x with the appearance of the C signal. The g-values are strongly associated with the point defects in AlN crystal. Here, the evolution of the A signal has similar tendency to the O-concentration and the C signal behaves similar to Si-concentration as shown in figure 4-1.

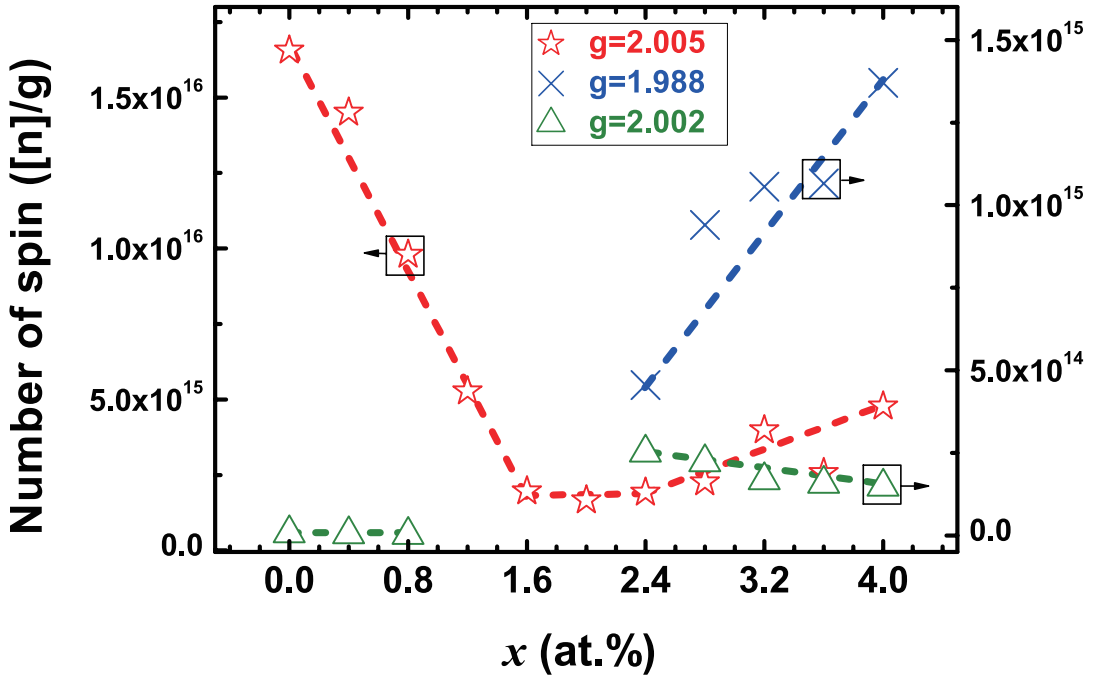

Figure 5-4. *The number of spin per gram of the fitted ESR signals as a function of x.*

Thus, it is reasonable to consider g=2.005 originates from O-related defect, while g = 1.988 comes from Si-related defect. Since these 2 signals have broad line width and the g values are apart from that of the free electrons, g_e (2.0023), they may be originated from the localized electrons on the deep levels. On the other hand, the g=2.002 is close to g_e, and its line-width is narrow and singlet line-shape. Thus, this may attribute to the delocalized electrons in shallow impurities.

5.2 Summary of ESR

We have clarified the defects origin of b-values of Si-doped AlN powders using ESR. Based on the evolutions of spin number compared with chemical concentrations result, the intensity of the *g*=2.005 signal is attributed to O-related defects, g=2.002 to shallow trap and g=1.998 to Si-related deep levels. Table 5-1 shows the correspondence of g-values and their possible origins in the references. The lowest paramagnetic defect density could be achieved at medium *x*.

Table 5-2. *Original defects of g-factors in Si-doped AlN powder*

Sort	***g*-value**	**Origin**	
		Our data	**Reference**
A	2.005	O-related defect	V_N [79]
			O_N-V_{Al} [38, 80]
B	2.002	Delocalized electron in shallow trap	V_{Al} [38]
C	1.988	Si-related defect	Si_{Al} [35, 42]

5.3 Evolution of CL spectra with Si-doping

Figure 5-5 shows the CL spectra of AlN powders doped with various Si concentrations. The un-doped AlN possesses two peaks at 3.2 eV and 3.6 eV. In accordance with Si doping, the 3.6 eV peak is dominant until *x*=1.6%, while 3.2 eV peak above it. Small shoulders can be seen at 4.2 eV (for medium *x*) and 2.8 eV (for high *x*). Figure 5-6 shows the variation of maximum CL peak intensity. The CL intensity increases with Si doping from *x*=0.8% to 2.4%, and then drastically decreases at high Si concentrations. Maybe luminescence occurs with very low O concentration, while the decrease of CL intensity may due to the increase of non-radiative defects.

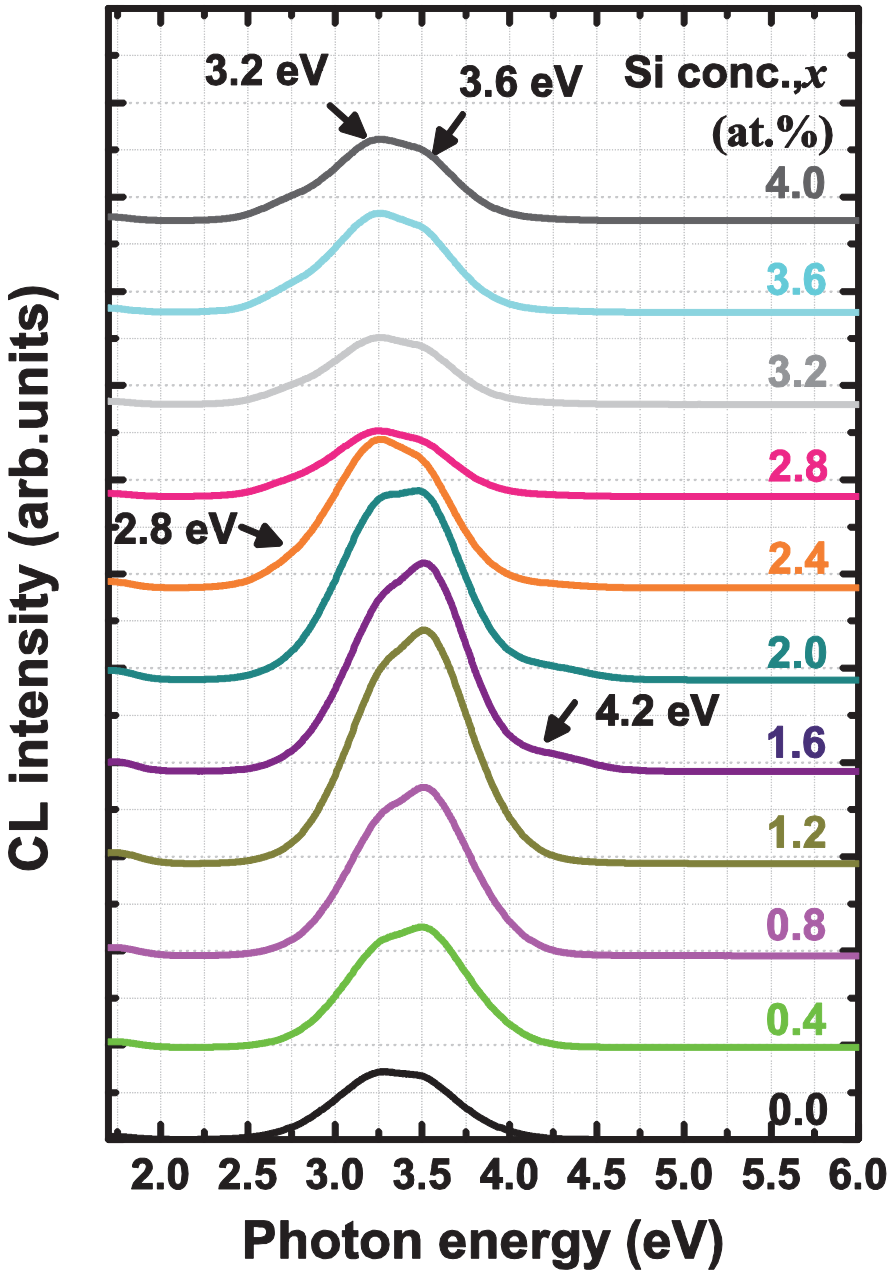

Figure 5-5. *CL spectrum of Si-doped AlN powders with different variations of x.*

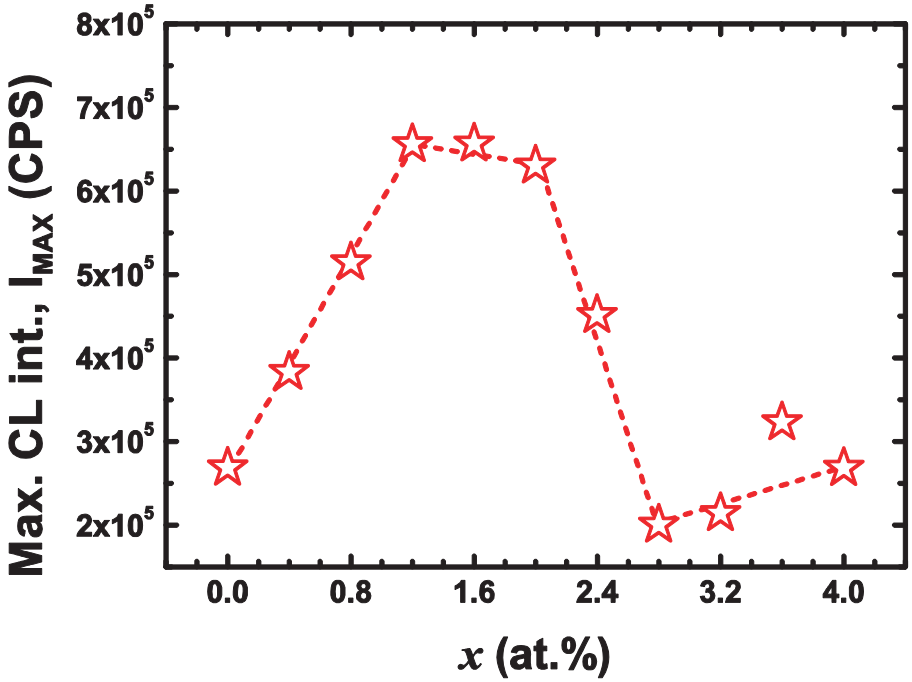

Figure5-6. *The CL peak maximum of Si-doped AlN powders as a function of x.*

The UV-blue peaks are originated from the radiative defect. So far, the defect related luminescence has been reported[42, 81, 82]. However, the attribution of these UV-blue emissions is highly controversial. In our approach, we have fitted the CL spectra and tried to correlate the CL peaks with the previous chemical and ESR results. Figure 5-7 shows the fitting of CL spectra on figure 5-5, and the ratios of fitted components ($I_{\text{fitted spectra,p}}/I_{max}$) were evaluated as a function of Si-doping in Figure 5-8. The ratio for 3.6 eV decreases until 2.8 eV and remains. The ratio for 3.2 eV is almost constant but slightly decreases at low x ($0.4\% \leq x \leq 1.6\%$). The general tendencies of both 3.6 eV and 3.2 eV ratios are similar to the defects evolution on Figure 5-4 but they do not correspond. Alternately, the tendencies are nearly related to the figure 4-2 that is the chemical concentration of Al and N. The 3.6 eV is dominant at poor-N area ($x \leq 1.6$ eV), while 3.2 eV is dominant at poor Al area ($x \geq 1.6$ eV). It indicates that the peak at 3.6 eV and 3.2 eV are related to V_N and V_{Al} of AlN powder.

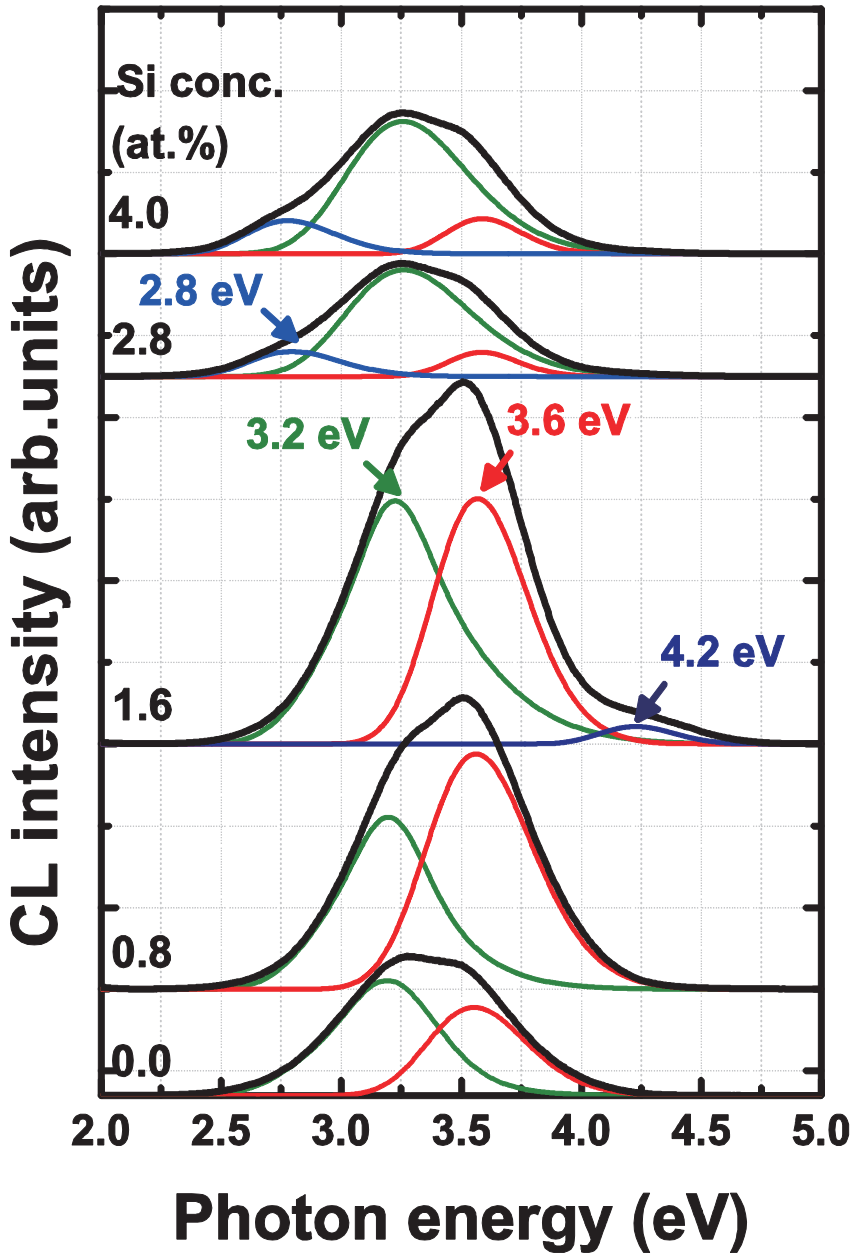

Figure 5-7. *CL spectra (black) with fitted spectra (colored) of Si-doped AlN powders.*

On the other hand, The peak at 4.2 and 2.8 eV can be seen at Si incorporation region (1.6%≤x), the shoulder at 4.2 eV exists in the lowest defect region (1.6%≤x≤2.0%), while that of the 2.8 eV in the secondary phase (2.4%≤x). The shoulders at 4.2 eV and 2.8 eV can be ascribed to the different states of Si related extrinsic defects in AlN crystal. The peak at 4.2 eV may be associated substitutional Si at Al-site (Si_{Al}) in and the one at 2.8 eV is due to Si formation in contaminated AlN.

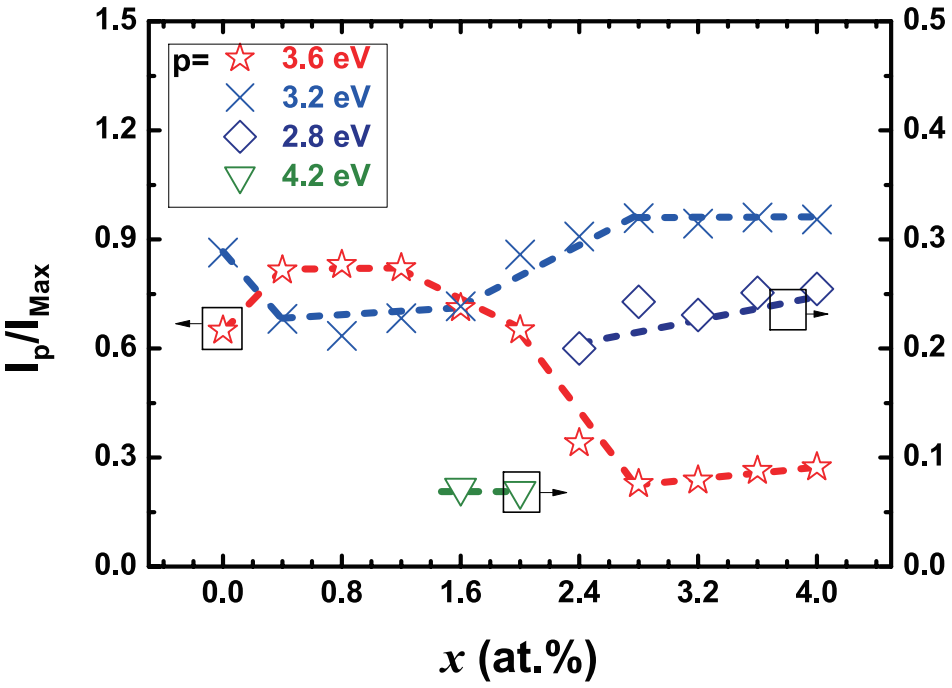

Figure 5-8. *The ratio of the fitted CL spectra as a function of x.*

5.3 Summary of CL

In this chapter, we have clarified the luminescence evolution of AlN powders by Si-doping. We have found an enhancement of the UV emission at the medium Si concentrations, which may be due to removal of non-radiative defects (phonons) and an improvement of the native defect emissions. We have also predicted the origin of defects and luminescence by correlating them with previous results. Although both of 3.6 eV and 3.2 eV peaks have been known as O-related native defects in AlN in previous research, our data indicated that the peak at 3.6 eV can be assigned to V_N-related defects while the peak at 3.2 eV to V_{Al}-related defects in AlN. The new peaks at 4.2 eV and 2.8 eV generated with Si-doping may be related to the different types of Si-accommodating defects, the 4.2 eV is Si_{Al} and the 2.8 eV is Si-AlN formation.

5.4 Conclusion (Ch.3-Ch.5)

To clarify the effect of Si in AlN powder, the structural, chemical, electrical and optical evolution were studied using SEM, ICP, XPS, XRD, ESR and CL. It can be categorized into 3 stages depending on the role of Si.

Table 5-3. *Summary from Ch.3 to Ch.5.*

	0.0%<x<1.6%	**1.6%<x<2.4%**	**2.4%<x<4.0%**
SEM	Polyhedral	Particle growth	Distortion
ICP	O-desorb/ poor-N	Si-incorporate/ poor-Al	
XPS	Al-O bonding	Al-N bonding	Si-N bonding
XRD	Lattice expand	High quality	Secondary phase
ESR	g=2.005	Fewer defects	g=1.988
CL	3.6 eV	Higher intensity	2.8 eV

Stage 1. Purification of AlN powder by removing O impurities.

Stage 2. Incorporation inside of AlN lattice by substituting Al-site, which improves the quality, luminescence and particle growth reaction of AlN powder.

Stage 3. Generation of secondary phase (concentration quenching)

For 1950°C and 8h sintering, the first stage occurs at the low Si concentrations (x<1.6%), the second one at the medium Si concentrations (1.6≤x<2.4), and third one at the high Si concentrations (x≥2.4%). In the next chapter, we are going to clarify the luminescence point more precisely as well as the sintering mechanism of Si-doped AlN powders depending on these stages.

Chapter 6: UV emissions and particle growth mechanism of Si-doped AlN powders

In Ch. 3 to Ch. 5, we have performed the macro-measurement to check the structural, chemical, electrical and optical properties of Si-doped AlN powders. As a result, we have found 3 different stages depending on the Si concentration. Si plays an important role in O-desorption, particle growth and secondary phase on the AlN particles at low (x<1.6%), medium (1.6%≤x<2.4%) and high (x≥2.4%) doping, respectively.

In this chapter, we evaluate the detailed luminescence properties and defects distribution of Si-doped AlN powders by micro-CL measurement. Firstly, to confirm its potential as UV emitting powder, luminescence distribution among the particles is investigated. Secondly, the synthesis mechanism of Si-doped AlN powders will be discussed via cross-sectional CL and EPMA analysis. The typical samples among low, medium, and high concentrations of Si-doped AlN powders were selected and compared with non-doped AlN powders.

6.1. Luminescence distribution among the particles

6.1.1. Non-doped AlN

Figure 6-1 shows the SE image (a), and CL image taken at 3.6 eV (b) of non-doped AlN powder. Powder is granular and the 3.6 eV emission is observed except darker spots at some particles. Point CL spectra are measured at several points indicated by arrows and are plotted in Fig. 6-1 (c) together with normalized CL spectra (inset). Although the intensities of brighter (point 1 and 2) and darker points (point 3 and 4) varied, all the spectra hava two peaks at 3.2 eV and 3.6 eV. Normalized spectra show that darker areas have strong shoulder at 3.2 eV. The 3.2

eV emission is strong in the defective structure, hence this emission can result from some defect structures. Through the previous chapter, we have correlated the 3.2 eV to V_{Al}-related and the 3.6 eV to V_N-related emission. These results suggest that the non-doped AlN powder is not uniform in terms of defect concentration.

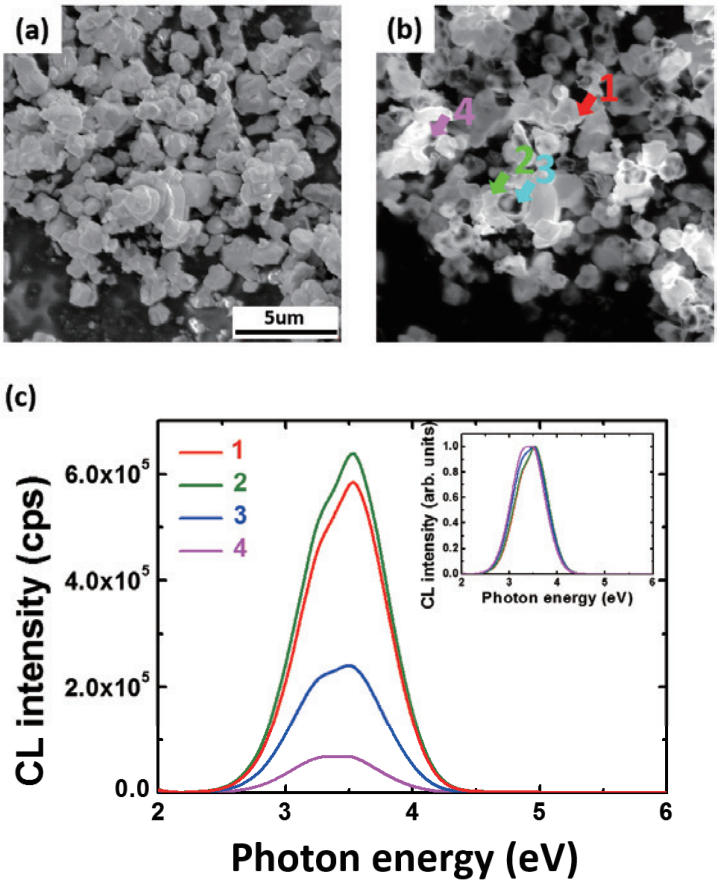

Figure 6-1. *SE (a) and CL images taken at 3.6 eV (b) for non-doped AlN powder. (c) CL spectra taken on areas indicated by arrows, with the normalized CL spectra as an inset.*

6.1.2. Low Si-doping

Figure 6-2 shows the SE (a), and CL images taken at 3.6 eV (b) and 4.2 eV (c) of 0.4% Si-doped AlN powder. The particles are bigger than non-doped AlN and have sharp polyhedral shape. The 3.6 eV emission is nonuniformly distributed along the particle with brighter and darker parts. The 4.2 eV emission is weak and its distribution is similar to 3.6 eV. Local point CL spectra are measured on areas indicated by arrows and are plotted in Fig. 6-2 (d), with the normalized CL spectra as an inset. The spectra consist of the main peak at 3.6 eV and a shoulder at 3.2 eV. The brighter areas (point 1 and 2) show stronger intensities with a smaller shoulder at 3.2 eV, while darker areas (point 3 and 4) weaker intensity with a stronger shoulder at 3.2 eV.

In comparison with the non-doped sample, only the shoulder at 3.2 eV becomes relatively smaller. These results indicate that low doping decreases the deep levels of AlN powder, but still some parts contain non-radiative defects.

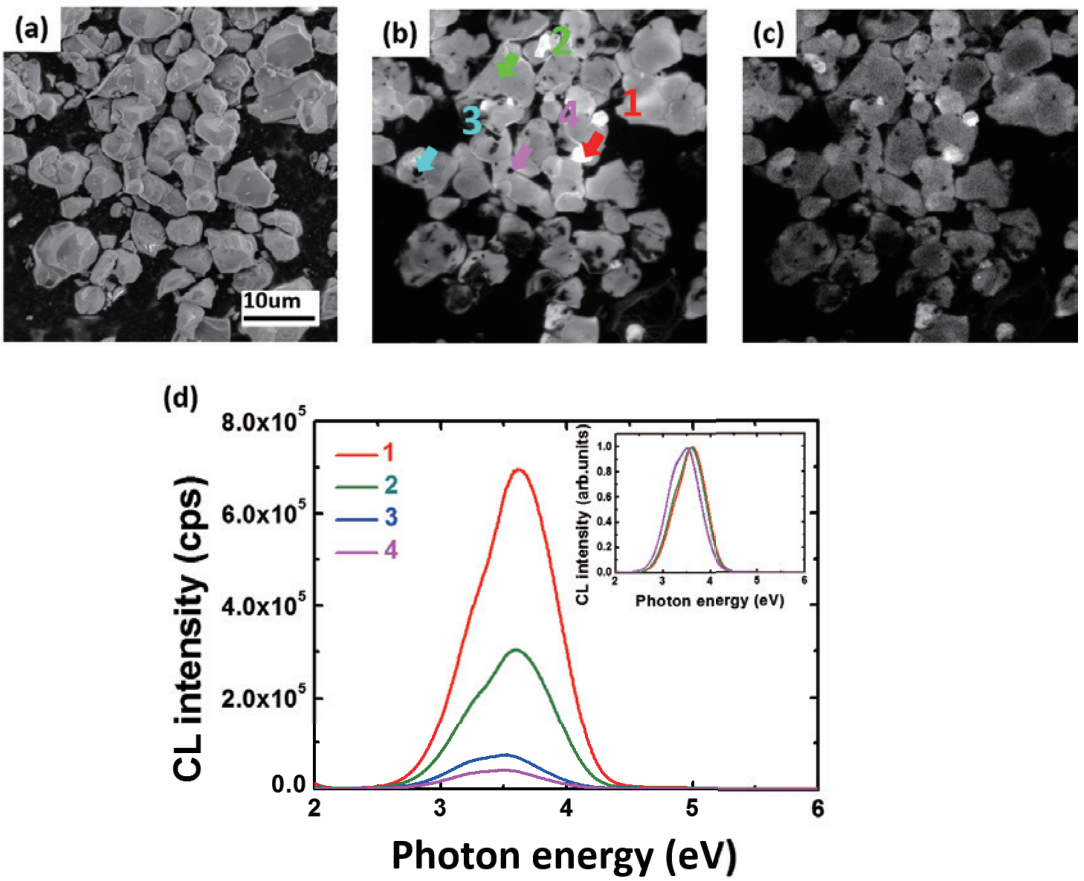

Figure 6-2. *SE (a) and CL images taken at 3.6 eV (b) and at 4.2 eV (c) for 0.4% Si-doped AlN powder. (d) CL spectra taken on areas indicated by arrows, with the normalized CL spectra as an inset.*

6.1.3. Medium Si-doping

Figure 6-3 shows the SE (a), and CL images taken at 3.6 eV (b) and 4.2 eV (c) of 1.6% Si-doped AlN powder. The particle morphology is truncated octahedron. The 3.6 eV emission is uniformly distributed without darker areas that was detected in non-doped or 0.4% Si-doped AlN. In the 4.2 eV emission image, some areas in a particle are brighter. Point CL spectra are measured on areas indicated by arrows and plotted in Fig. 6-3 (d), with the normalized CL spectra as an inset. Point 1 and 2, corresponding to the brighter areas in 4.2 eV image, shows a

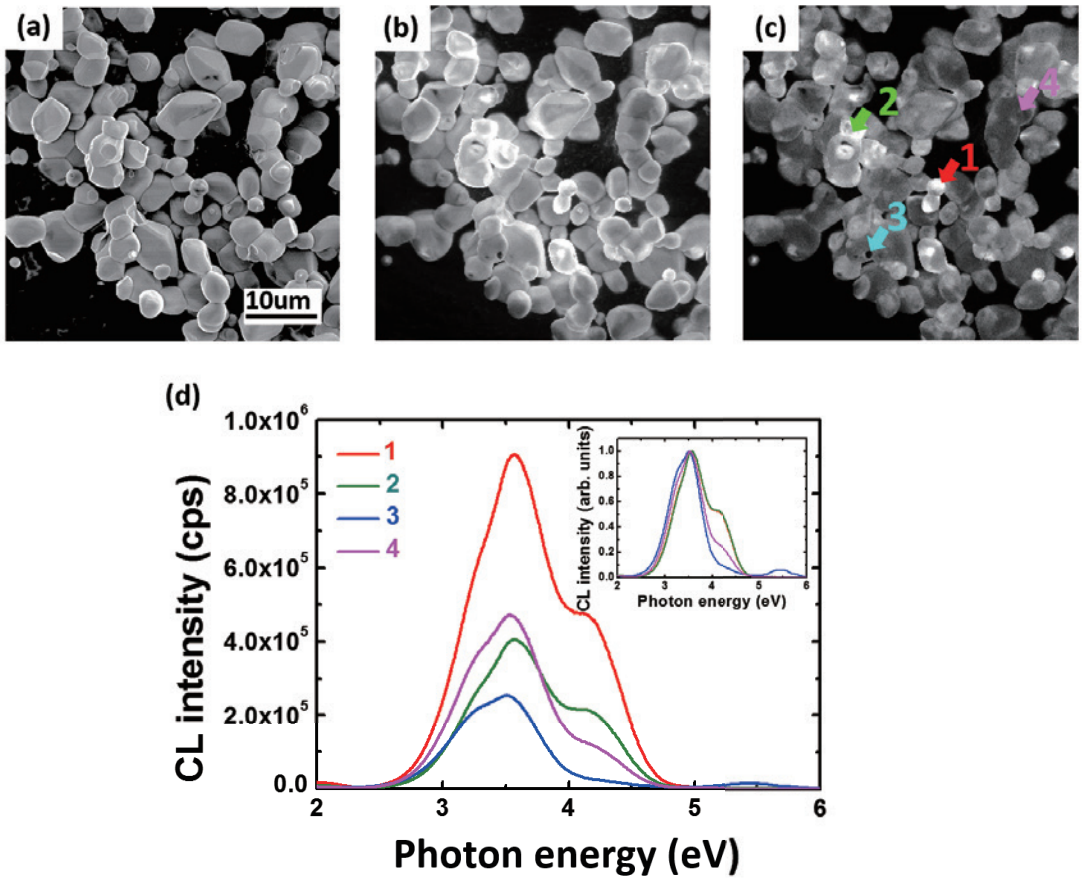

Figure 6-3. *SE (a) and CL images taken at 3.6 eV (b) and 4.2 eV (c) for 1.6% Si-doped AlN powder. (d) CL spectra taken on areas indicated by arrows, with the normalized CL spectra as an inset.*

main peak at 3.6 eV with a shoulder at 4.2 eV. Point 4, which corresponds to darker area in 4.2 eV, shows a main peak at 3.6 eV with the small shoulders at 3.2 eV and 4.2 eV. Point 3, corresponding to a dark spot, shows a main peak at 3.6 eV with a stronger shoulder at 3.2 eV and smaller shoulder at 4.2 eV. Unexpectedly, another peak at 5.5 eV appears. This peak is close to the band edge emission of 6.2 eV. Thus this emission may be related to shallow defects in AlN. We have attributed the 4.2 eV to Si-related (Si_{Al}) defect in AlN in Ch.5. These results indicate that medium Si doping has a great possibility to improve deep UV emission. Moreover, it is widely known that spherical phosphor particles with fine size can improve the panel efficiency by forming a thin and flat phosphor layer in the device fabrication[83].

6.1.4. High Si-doping

Figure 6-4 shows the SE (a), and CL images taken at 3.6 eV (b) and 4.2 eV (c) of 4.0% Si-doped AlN powder. The particles morphologies are of an asymmetric polyhedral shape. The CL image taken at 3.6 eV shows the existence of darker patches along the particles. The 4.2 eV emission is weak and its distribution is similar to 3.6 eV one. Point CL spectra are taken on the bright and dark areas. Points 1 and 2 correspond to bright, while the point 3 and 4 correspond to darker patches. The formers have a main peak at 3.2 eV with a shoulder at 3.6 eV. Small peak at 2.8 eV is also observed. The latter have a main peak at 3.6 eV with a shoulder at 3.2 eV. Small shoulder at 4.2 eV is also observed. The 2.8 eV may be related to Si formation defect in AlN. These results indicate that Si is non-uniformly distributed with secondary phase, which is responsible for suppressing the luminescence.

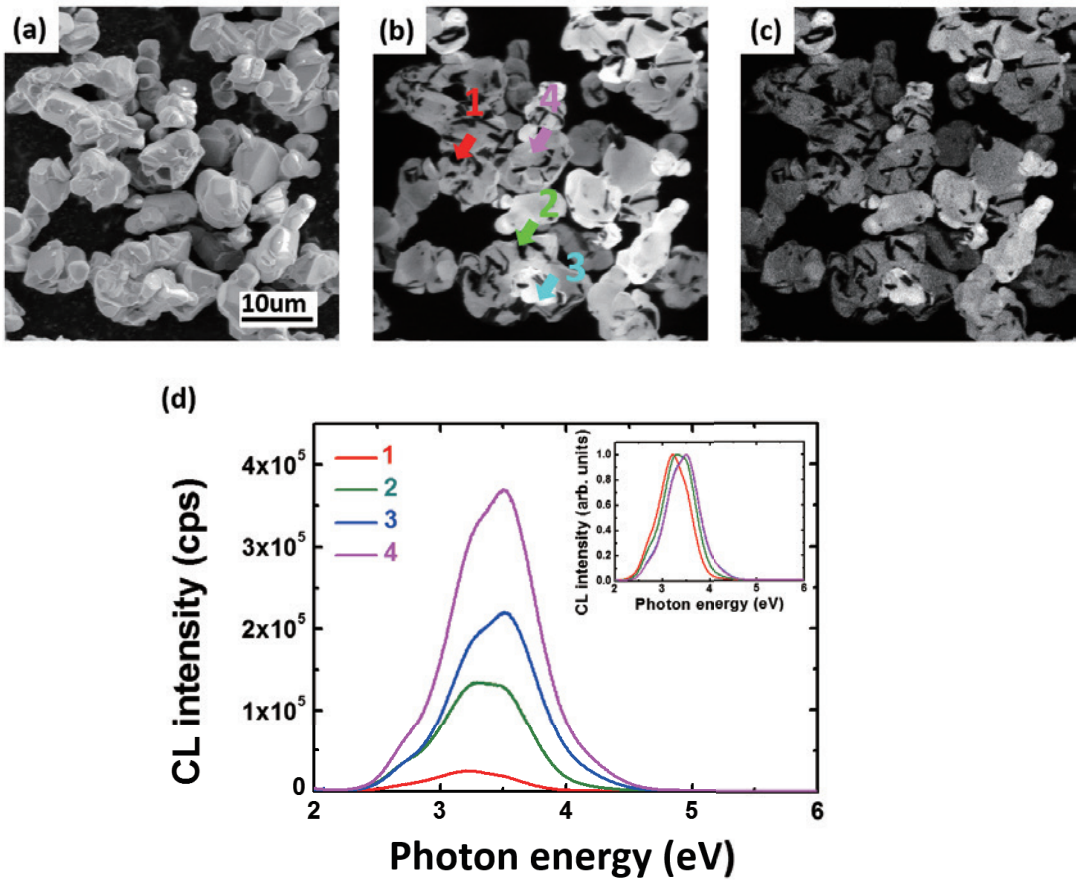

Figure 6-4. *SE (a) and CL images taken at 3.6 eV (b) and 4.2 eV (c) for 4.0% Si-doped AlN powder. (d) CL spectra taken on areas indicated by arrows, with the normalized CL spectra as an inset.*

6.2. Synthesis mechanism

In order to confirm the synthesis mechanism of Si-doped AlN powders, it is necessary to observe the inner part of particles. Thus, we have performed cross-sectional (CS) observation. We will firstly introduce the CS specimen preparation technique. Then, detailed CS observations are elaborated.

6.2.1. Sample preparation: Cross-sectional polishing

Cross sectional polishing method using an argon ion beam (CP method) is an useful method to observe layered structures, due to its wider polishing area with less surface damage. In order to achieve CP for the luminescent powders, powders were embedded into a resin to form a sample chip. Although the particles are randomly distributed and cannot specify the exact cutting position, the cutting area had enough particles to observe.

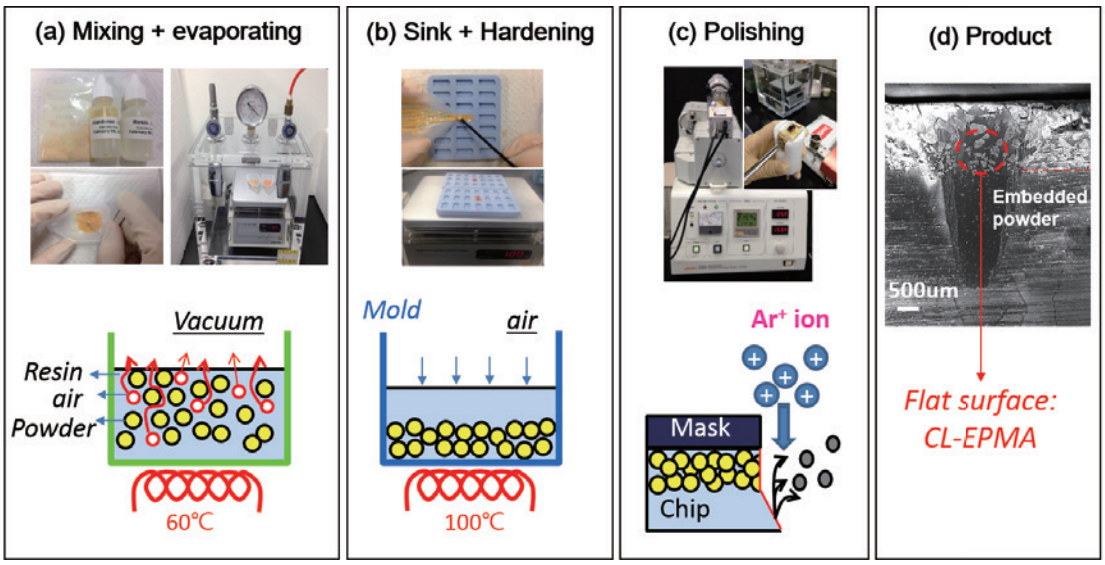

Figure 6-5. *Cross-sectional preparation of ceramic powder.*

Figure 6-5 shows the CS preparation of ceramic powders. Firstly, the powders are mixed with resin and hardener, and then poured into a plastic cup. They are heated at 60 °C in vacuum for evaporating oxygen from the mixture (a). Secondly, they were put into a silicon mold and baked again at 100 °C in air to fabricate a powder embedded chip (b). During heating, most of the powders are deposited at the bottom due to high material density. The facet of underside of the chip is polished by means of CP (c). As shown in (d), the produced mirror surface and higher amount of molded powders allows observation of the inner structure of powders.

6.2.2. Non-doping

Figure 6-6 shows the cross-sectional SE (a) and CL images taken at 3.6 eV (b) and 4.2 eV (c) of non-doped AlN powder. Schematic illustration is shown in (d). The 3.6 eV image reveals some bright parts and dark spots. The 4.2 eV image is weak and looks similar to the 3.6 eV image. The darker spot inside the particle is attributed to the defective area, which is similar to the dark areas observed in Fig.6-2. The particles have started to coalesce each other without Si_3N_4 additives.

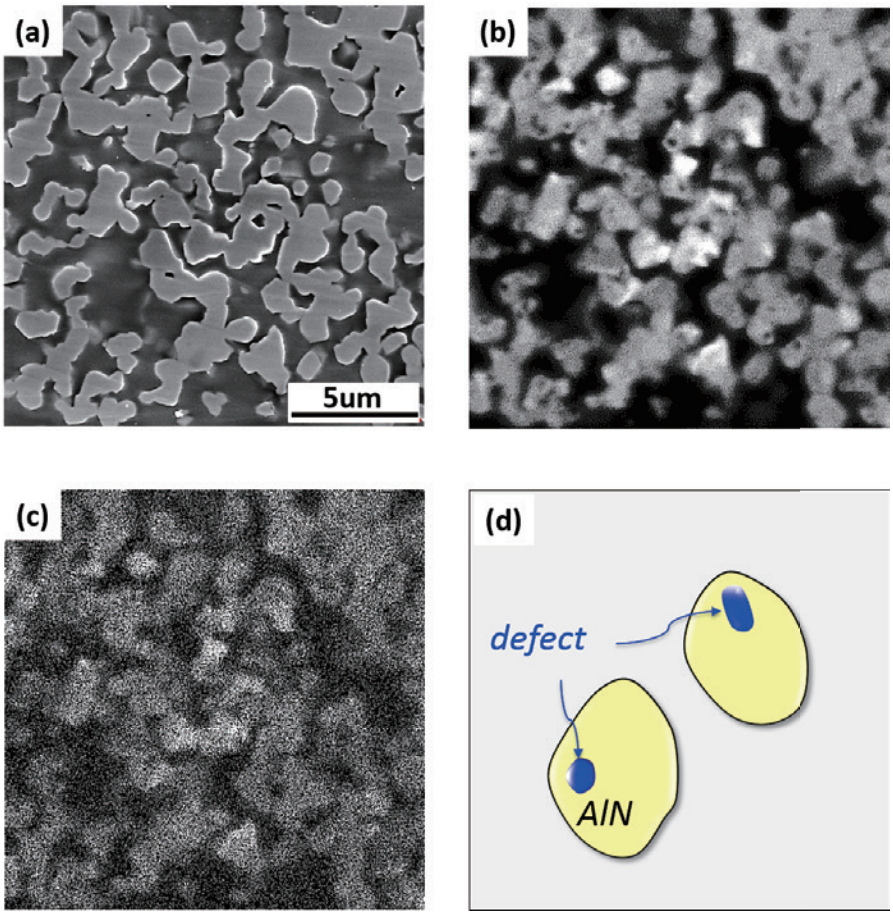

***Figure 6-6**. Cross-sectional SE (a) and CL images taken at 3.6 eV (b) and 4.2 eV (c) for non-doped AlN powder. (d) Schematics illustration.*

6.2.3. Low Si-doping

Figure 6-7 shows cross sectional SE (a) and CL images taken at 3.6 eV (b) and 4.2 eV (c) of 0.4% Si-doped AlN powders. Schematic of the powders was drawn on (d). The SE image shows that the particles are agglomerated to each other what makes it difficult to distinguish their grain boundaries. Interestingly, the CL image taken at 3.6 eV is uniform and no dark spots are observed in the particle. It shows a little difference exists between core and grain boundary. In the 4.2 eV image, such discrepancy is more clearly observed. The surface area is brighter than core. Many particles are connected to each other with these bright skins. Since the 4.2 eV is

related to the Si_{Al} (Ch.5), it is reasonable to think that a thin Si-rich layer coats the surface. It creates an attractive force between particles, putting particle contact in compression. Consequently, the element diffusion may be increased along the particles that contact and liquidus grain boundary. On the other hand, small amount of Si is not incorporated but reacted with out-diffused O in AlN matrix to form SiO vapour.

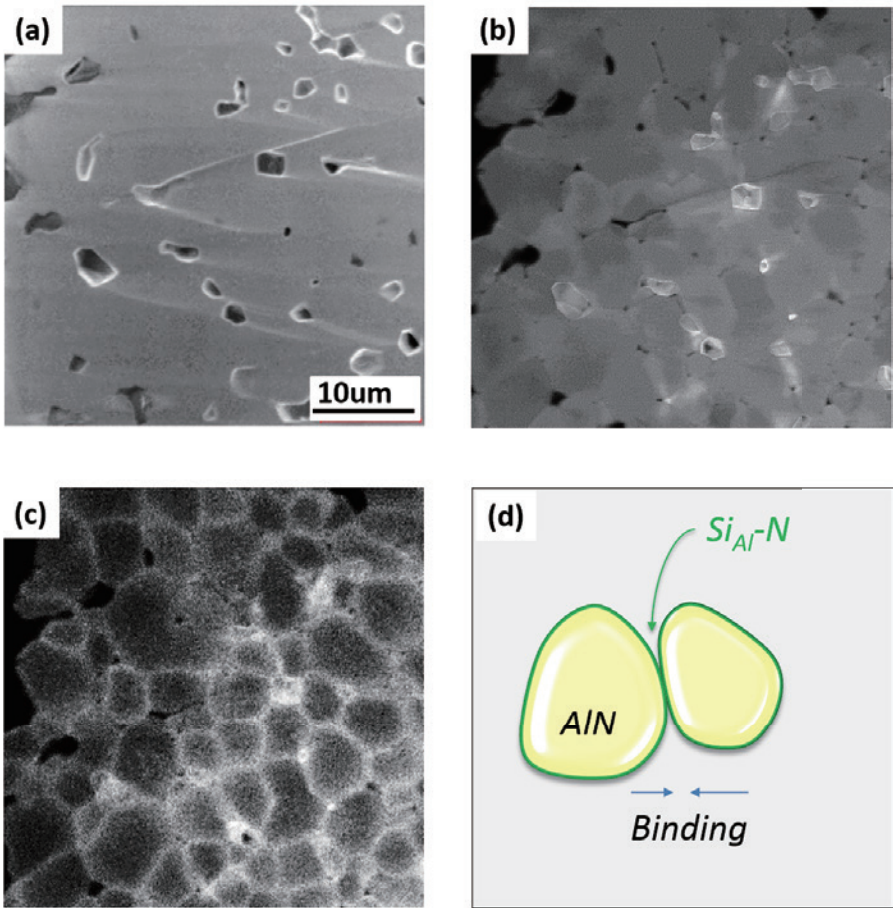

Figure 6-7. *Cross-sectional SE (a) and CL images taken at 3.6 eV (b) and 4.2 eV (c) for 0.4% Si-doped AlN powder. (d) Schematic illustration.*

6.2.4. Medium Si-doping

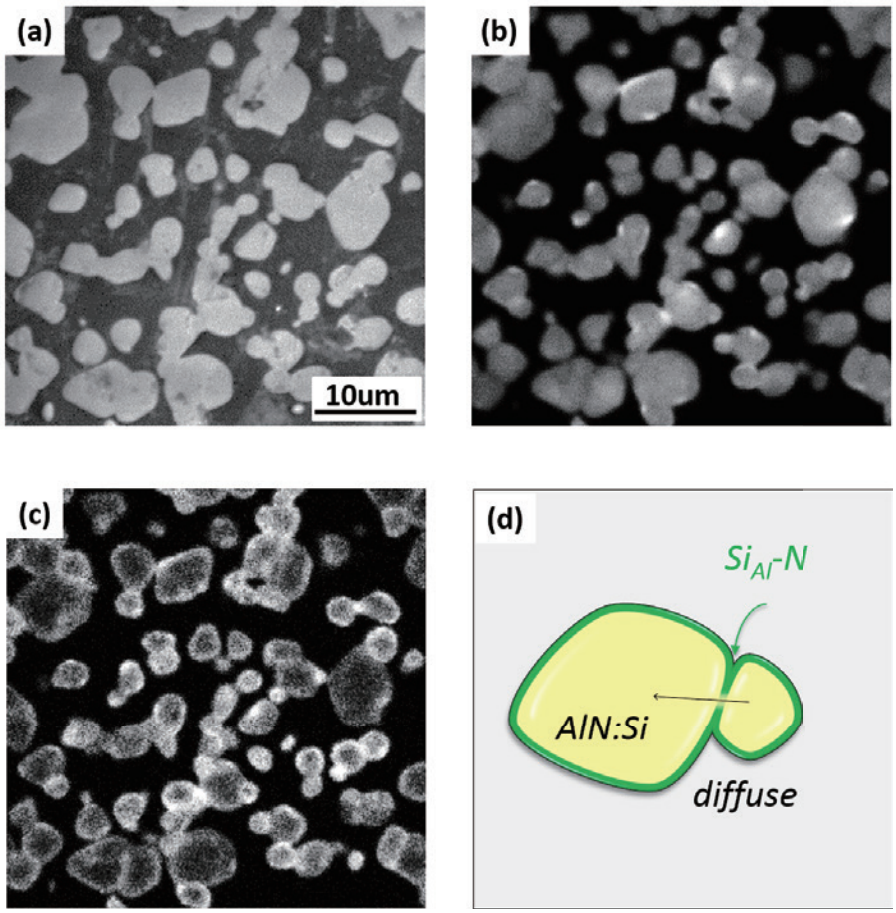

Figure 6-8. *Cross-sectional SE (a) and CL images taken at 3.6 eV (b) and 4.2 eV (c) for 1.6% Si-doped AlN powder. (d) Schematic illustration.*

Figure 6-8 shows cross sectional SE (a) and CL images taken at 3.6 eV (b) and at 4.2 eV (c) for 1.6% Si-doped AlN powders. Schematic is drawn on (d). At x=1.6%, the 3.6 eV emission is rather uniform with some brighter area. The 4.2 eV emission is strong at the particle surface. The bright skins are thicker than those in x=0.4%. It is interesting to note that the larger particles contact with smaller particles. This may be due to the Ostwald ripening. Namely the smaller particles dissolve and re-deposit on larger particles during sintering. Thus, we think that the element diffusion may be driven across grain boundaries at medium Si-doping.

6.2.5. High Si-doping

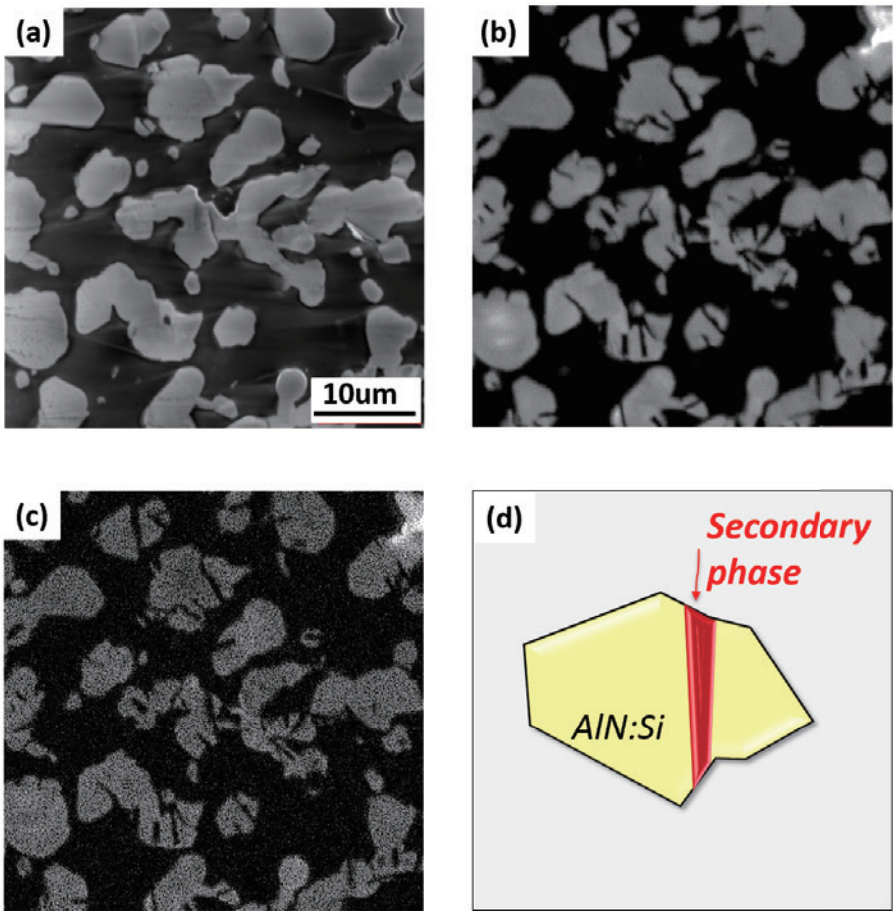

Figure 6-9. *Cross-sectional SE (a) and CL images taken at 3.6 eV (b) and 4.2 eV (c) for 4.0% Si-doped AlN powder. (d) Schematic illustration.*

Figure 6-9 shows cross sectional SE (a) and CL images taken at 3.6 eV (b) and at 4.2 eV (c) of 4.0% Si-doped AlN powders. Schematic explaining the CL observations is drawn on (d). At x = 4.0 %, both 3.6 eV and 4.2 eV emission images look similar although the latter emission is rather weak. It was found that dark bands exist in large particles, which can be seen in Fig. 6-5. (b), (c). Such bands may correspond to the interfaces between particles. The point CL spectrum shows high ratio of 2.8 eV emission at these dark bands and XRD analysis suggests that they are secondary phase.

In order to confirm the element distribution along the particle, EPMA line scan was performed. The figure 6-10 shows the back scattering electron (BE) image of cross sectional (a), CL image at 2.8 eV (b), and variation of elements along the lines indicated in (b). The concentrations are plotted (c) with 0.2 μm spacing of the *x*=4.0% Si-doped AlN. The BE and CL image shows the difference contrasts at region Ⅰ and Ⅱ. The EPMA line scan of Al, N, O and Si

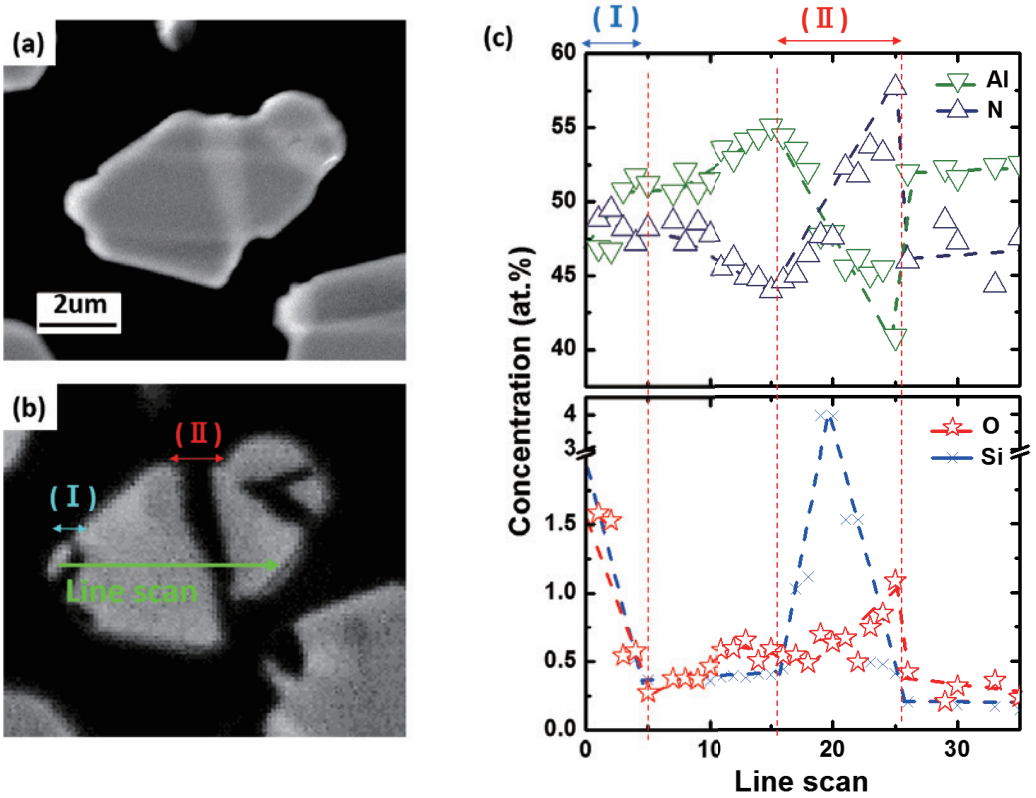

Figure 6-10. *Cross-sectional BE (a) and CL image taken at 2.8 eV (b) for 4.0% Si-doped AlN powder. (c) Compositional concentration variation along the green arrow in (b).*

elements shows that higher amounts of Si exist at region Ⅰ and Ⅱ, the interfaces between particles. The O-component is also relatively high at the interface regions but non-uniformly distributed. The component of Al and N elements complementarily varied. Al concentration is high at the inner part of the particle, while N is at the interfaces. These results indicate that higher concentration of Si_3N_4 may form massive Si-Al-O-N band at the boundaries of AlN

particles. Such Si-Al-O-N phase may stabilize, hence not promoting AlN crystal growth.

6.3. Model of particle growth

CL investigation shows that medium Si doping is the most accurate to present the uniform emission and to give 4.2 eV and 5.5 eV. On the other hand, low and high Si concentrations show the plenty of darker areas along the particles.

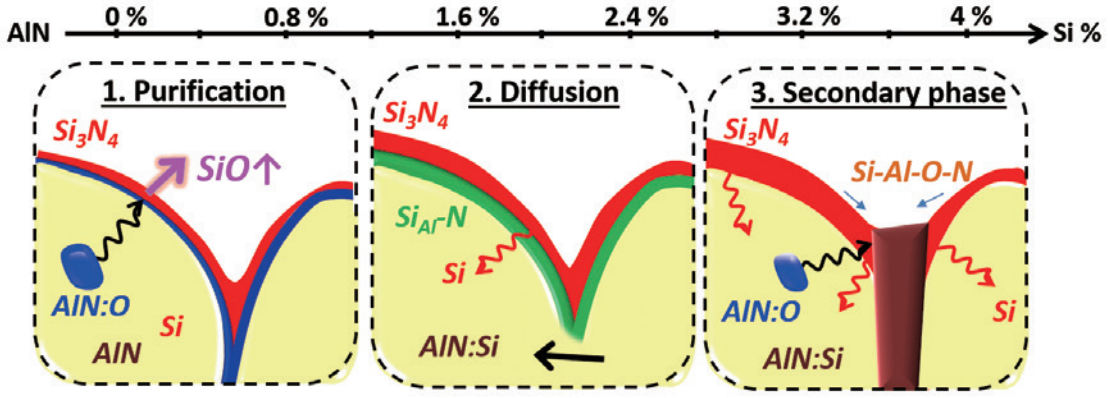

Figure 6-11. *Schematics explaining of sintering mechanism of Si-doped AlN powder at 1950°C for 8h depending on Si concentration.*

We consider the following sintering processes of Si-doped AlN powders based on CS investigation. The melting temperature of AlN and Si_3N_4 is 2200 and 1900 °C. During sintering at 1950 °C, Si_3N_4 may initially melt and a liquidus Si-N coats on the AlN particle surface which consequently increases particles adhesion. Then, the solid-state diffusion may be driven resulting in faster bonding and densification along the boundaries, as followed the conventional liquid phase sintering process[45]. Subsequent reaction during densification and coalescence depends on the amount of Si concentration is proposed on Figure 6-12.

At low Si-doping, the oxygen impurities in AlN particles are out-diffused, than they may react with Si-N to form SiO at the surface and grain boundaries. Since SiO is volatile, O is effectively removed from the surface. Small amount of Si is insufficiently incorporated into AlN crystal.

At medium Si-doping, Si can be incorporated from the surface into AlN crystal. Through the liquidus Si-N grain boundary migration, solid state and liquid diffusion processes may be driven, consequently particle growth with a larger particle consuming the smaller particle.

At high Si-doing, high amount of Si reacts with AlN to form massive Si-Al-O-N structure at the interface between the particles.

Chapter 7: Conclusions and perspectives

7.1. Summary of Si-doped AlN study

This thesis is devoted to the study of the influence of Si on the properties of AlN powder. Commercial AlN powders were sintered with Si_3N_4 additives according to the composition of $Al_{1-x}Si_xN_{1+x/3}$ with $0.0\% \leq x \leq 4.0\%$ using a GPS furnace.

At the first half of this thesis (Ch. 3-Ch. 5), the structural, chemical, electrical and optical properties of Si-doped AlN powders were elucidated. At the latter half (Ch. 6), using cross sectional observation, the sintering mechanism was discussed.

- Effects of Si on the structural, chemical, electrical and optical properties of AlN

The structural, chemical, electrical and optical properties of the Si-doped AlN system were studied using SEM, ICP, ESR and CL.

As for the powder reaction, 3 stages were defined as shown in Table 7-1. For low Si concentration, AlN powders were purified through O desorption and the formation of SiO vapor. At medium Si concentration, Si starts to be incorporated in AlN. The crystal quality, particle size and CL intensity have been significantly improved. For high Si concentration, Si induces the formation of secondary phases that alter the luminescence properties.

Table 7-1. *Three different stages for Si-doped AlN system.*

Stage	Si conc.	Phase	Role of Si	Defects (ESR)	Luminescence (CL)
1	Low (<1.6%)	AlN:O	O-purification	O-defects	X
2	Medium (1.6≤x<2.4)	AlN:Si	Particle growth	Fewer defects	O
3	High (≥2.4%)	SiAlON	Secondary phase	Si-defects	X

- Sintering mechanism of Si-doped AlN powders

The sintering mechanism of Si-doped AlN powder of was investigated by cross-sectional CL-EPMA measurement. Based on these observations, we propose a model to explain the growth mechanism, as shown in Figure 7-1.

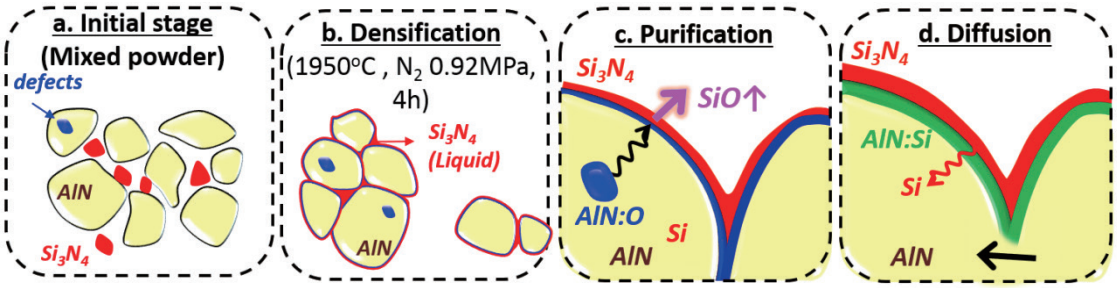

Figure 7-1*. Proposal for the growth mechanism at medium concentration of Si-doped AlN.*

It was found that Si_3N_4 additives may promote the liquid phase sintering process by melting and combining the particles. Consequently, the O out-diffusion may enhance particle growth and Si dissolution into the AlN matrix.

7.2. Future perspectives

We present the following perspective for future research

- UV emitters

We have found that Si-doping induces the O-desorption from commercial AlN powders. AlN powders doped with 1.6 Si% have the most promising properties as UV emitters. The spherical particle shape with fine size is expected to form a compact phosphor layer in the actual device.

On the other hand, it was still difficult to get a near band edge (NBE) emission from AlN powders. Only the native emissions of 3.2 eV and 3.6 eV were significantly improved. They may be associated with vacancies in AlN. To get NBE emissions from Si-doped AlN powders, it is better to try a different sintering method, such as HIP process. We are going to try this method and preliminary results were shown in Annex2.

Furthermore, the phenomena found in this work may be easily be extended to other nitride components, such as BN or GaN for their application to UV emitters.

- Other applications of AlN

High quality Si-doped AlN powders may be applicable not only for UV emitters but for other usages as well. For instance, AlN powder could be used to fabricate single-crystal AlN substrates or it could be used in Sialon phosphor sintering.

- Perspective for other (oxy)nitride components

We have investigated the sintering mechanism by cross sectional sample preparation. This preparation technique can be applied to other kinds of powders and could be used to prepare samples for TEM analysis.

Annex 1: TEM and CL analysis of Si-doped AlN powders

In this Annex, we highlight the TEM and CL analysis for Si-doped AlN powders. In this thesis, we have found that Si-doping is an effective way to control the defects of AlN powders. The proposed model postulates that the proper amount of Si doping (x<1.0%) has suppressed the oxygen impurity in AlN. At medium x (1.6≤x<2.4%), Si substitute for Al, while, above x=2.4%, a new type of phase defect is stable with containing Si and O. And this phase has yields a 2.8 eV emission band with non-radiative patches. So far, the polytypoid structure of 8H, 15R, 12H, 21R and 27R were found in the AlN-Al_2O_3, AlN-Al_2O_3-Y_2O_3 and AlN-Al_2O_3-SiO_2 sintering systems[78, 84, 85]. Previously, it has been accepted that the structure of AlN polytypoids based on the 2H AlN structure (wurtzite type) with periodically spaced stacking faults along the close-packed planes[84, 86]. Recent researches have been described as arrays of inversion domain boundaries (IDBs) along AlN basal (100) planes[85, 87-89].

Now, it is possible to correlate the new emission at 2.8 eV to a certain polytypoid structure or part of AlN powders. For this purpose, we have selected the 4.0% Si-doped AlN sample to investigate the localized structure of those Si-AlN particles by energy dispersive X-ray spectroscopy (EDS), cathodoluminescence (CL) and transmission electron microscope (TEM).

A1.1 Sample preparations

To fabricate the specimen for TEM measurement, we have used the focused ion beam (FIB) lift out technique. Which is well known as a versatile method for the preparation of site-specific TEM specimens[90]. Firstly, we have prepared the cross-sectional sample polished by CP, and then performed FIB. Figure A1.1 is a sample for CP (a) and TEM specimen fabricated by FIB lift out method (b). The size of fabricated specimen is 10 (width) x 3 (height) x 0.1μm (thickness).

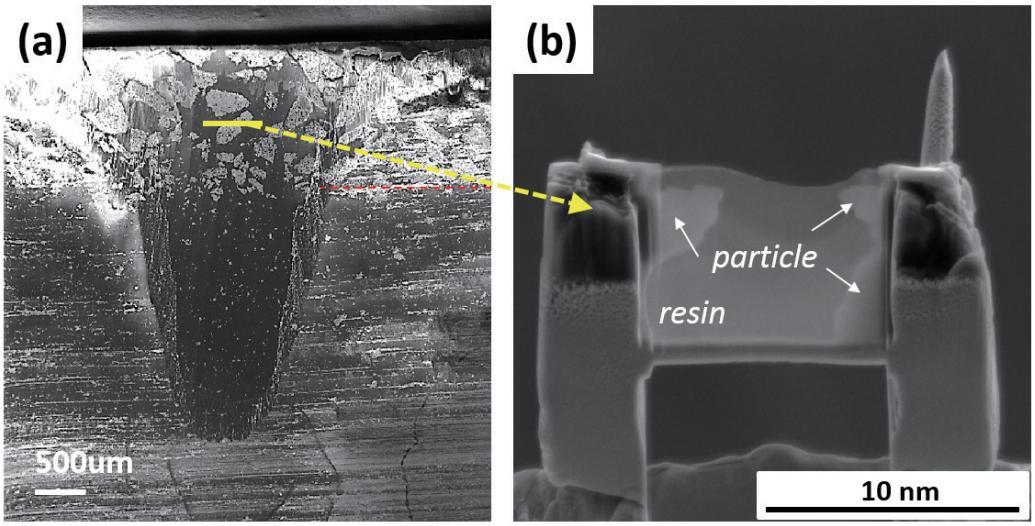

Figure A1.1 *(a) Cross-sectional polished sample of 4.0% Si doped AlN powder and (b) TEM specimen that picked out from (a)*

A1.2 EDS and CL results

Figure A1-2 shows the SEM (a), EDS (b) and CL images of FIB specimen taken at 3.6 eV (c) and 2.8 eV (d). It has been found that the particle consists of 3 different parts. Although it is very thin (~100nm), we could clearly see the element distributions of Al and Si in EDS image. There is a thick Si rich phase at the interface of the two particles. The CL image at 3.6 eV and the 2.8 eV emissions are observed uniformly in 2 particles, while both become weak at the Si-rich interface.

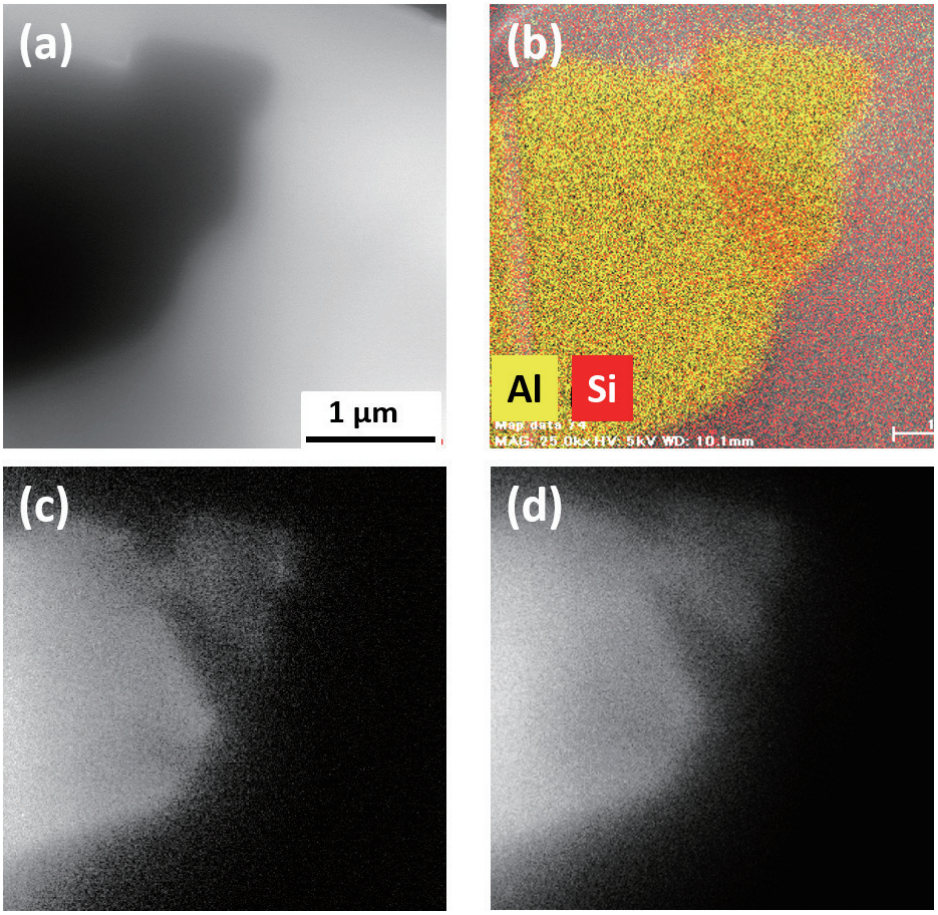

Figure A1.2 *SE image (a), EDS image of Si and Al element distribution (b) and CL images of FIB specimen taken at 3.6 eV (c) and 2.8 eV (d).*

A1.3 Origin of luminescence

Figure A1-3 shows the typical TEM photomicrograph (a), and the selected-area diffraction (SAD) patterns taken at the $[2\bar{1}\bar{1}0]$ and $[0001]$ zone-axes from point 1 (b) and point 2 (c), respectively. The big and small particles have different contrast in TEM image. In SAD investigation, A big particle (point 1) shows hcp single crystal pattern with the lattice parameter a= 0.51 nm. This value is near to that of β-Sialon (a=0.76 nm)[91]. The smaller particle (point 2) shows the long-period polytypoid AlN pattern. It contains the five diffraction-spots in AlN unit cell long $[0001]$ direction, corresponding 24H (11AlN-SiO_2)[89]. It indicates that the 24H polytypoid structure coexists with 2H structure within one Si-doped AlN particle. In order to confirm its emission, point CL spectrum has been observed in Figure A1-3 (d). CL spectrum of (b) part (points 1) shows a strong emission at 2.8 eV with a shoulder at 3.2 eV. On the other hand, the (c) part (point 2) has a weak emission at 2.8 eV and a smaller shoulder at 3.2 eV. It suggests that the origin of the 2.8 eV peak is from Sialon. The special resolution of point CL measurement, AlN emission of 3.2 eV could be overlapped.

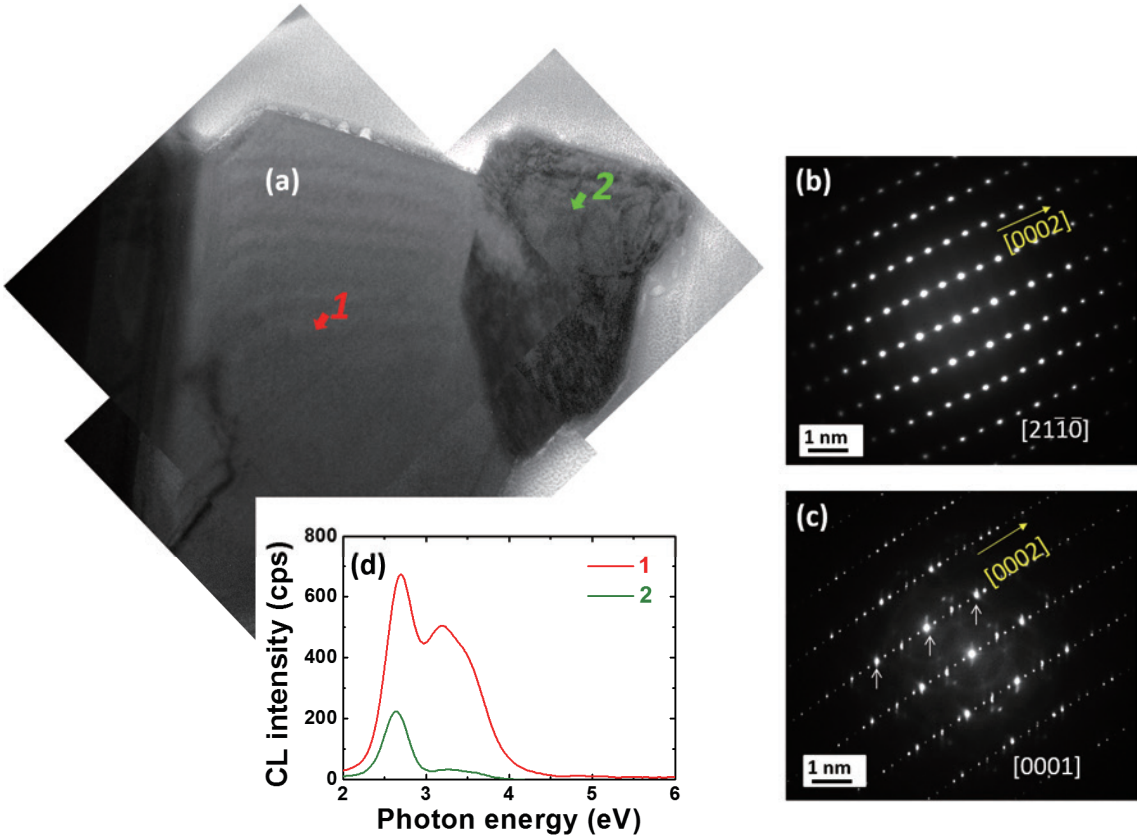

Figure A1-3. *TEM bright-field image of 4.0% doped Si-doped AlN particle (a), electron diffraction patterns (b, c) and point CL spectrum (d) of point 1 and 2, marked in (a).*

A1.4 Origin of darker patches

The interface between AlN and polytype shows darker patch in CL image and the higher Si concentration in EDS mapping. Figure A1-4 shows the SAD pattern and corresponding high-resolution (HR) TEM image of this darker patch. The SAD pattern shows the overlapped hcp patterns in rhombus shape with streaks along the $[2\bar{1}\bar{1}0]$ direction. This indicates two hcp domains with stacking imperfections exist in this area. The corresponding HRTEM image shows the twinning structure, namely herringbone pattern. The point CL spectrum shows very week emissions at 3.2 eV with a shoulder of 2.8 eV.

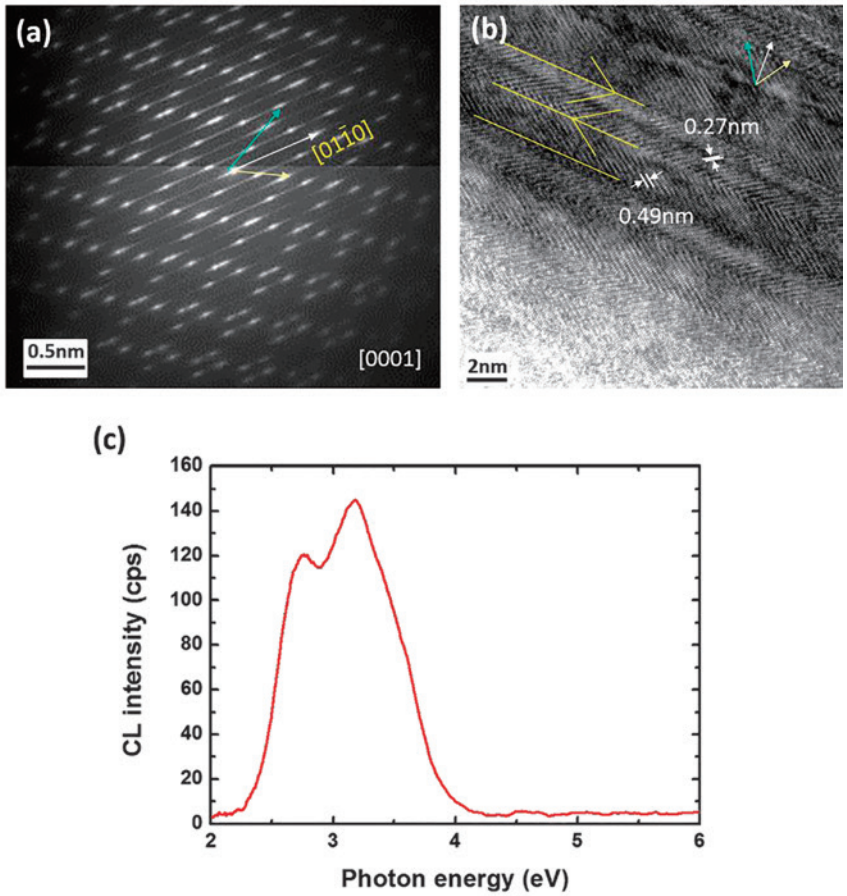

Figure A1-4. *(a) Selected-area diffraction (SAD) patterns and corresponding high-resolution (HR) TEM image and (c) CL spectra of the darker patch of 4.0% Si-doped AlN particle.*

A1.5 Conclusions

We have investigated the structure of 4.0% Si-doped AlN particles by TEM with CL. The elongated Si-rich interface exhibited polytype AlN phase. The irregular mixtures of 2H AlN produced twinning structure and a streaked diffraction pattern. The 2.8 eV is attributed to single Sialon crystal while the polytypoid and twinning AlN structure is almost non-luminescent.

Annex 2: A comparison between GPS and HIP methods for Si-doped AlN powders synthesis

This annex concerns the comparison of Gas Pressure Sintering (GPS) and Hot Isostatic Pressing (HIP) processes for Si-doped AlN sintering. As described in Ch.2, GPS and HIP processes are conventional methods to synthesize ceramic powders. In this thesis, we have been used GPS technique to synthesize Si-doped AlN powders for UV emitters. The results suggested that the synthesis temperature and N_2 pressure should be higher than the typical GPS conditions. Since HIP can apply higher temperature and pressure to the specimen (GPS: ~2200°C/~10 MPa HIP: ~2500°C/~200 MPa), it may be preferable to use HIP for Si-doped AlN powder sintering.

Hereby, we have prepared from 0.0% to 4.0% Si-doped AlN powders and synthesized them by HIP process under 1950°C, for 4h and 150 MPa N_2. The structural, chemical and luminescent properties of obtained powders were compared with those made by GPS process, sintered under the same temperature and duration but different N_2 pressure of 0.92 MPa N_2.

A2.1 Structural properties

Figure A2-1 shows the SE images of x=0.0% (a), (d), 1.6% (b), (e) and 4.0% (c), (f) of Si-doped AlN powders sintered by GPS (a, b, c) and HIP (d, e, f) methods. In GPS samples, the particle size was significantly grown at x=1.6%, and particle morphology is polyhedral at x=0.0 and 4.0%, and octahedron at x=1.6%. In HIP method, on the other hand, all the samples were small granular with less than 1 μm in size.

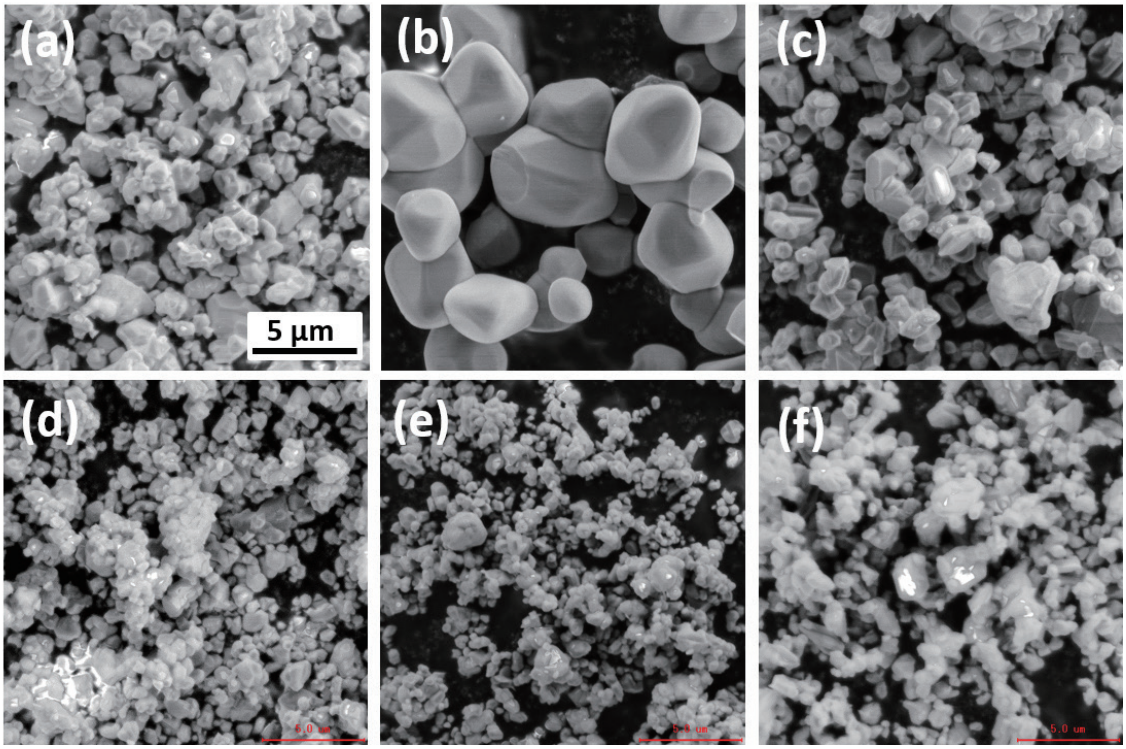

Figure A2-1. *SE images of x=0.0% (a), (d), 1.6% (b), (e) and 4.0% (c), (f) of Si-doped AlN powders sintered by GPS (a,b,c) and HIP (d,e,f) methods.*

Figure A2-2 shows the XRD results of x=0.0% and 1.6% of Si-doped AlN powders sintered by GPS and HIP methods. The GPS samples showed wurtzite phases of AlN and there are no changes between the non-doped and 1.6% doped samples. In HIP samples, a secondary phase of SiAlON appears Si-doped specimen.

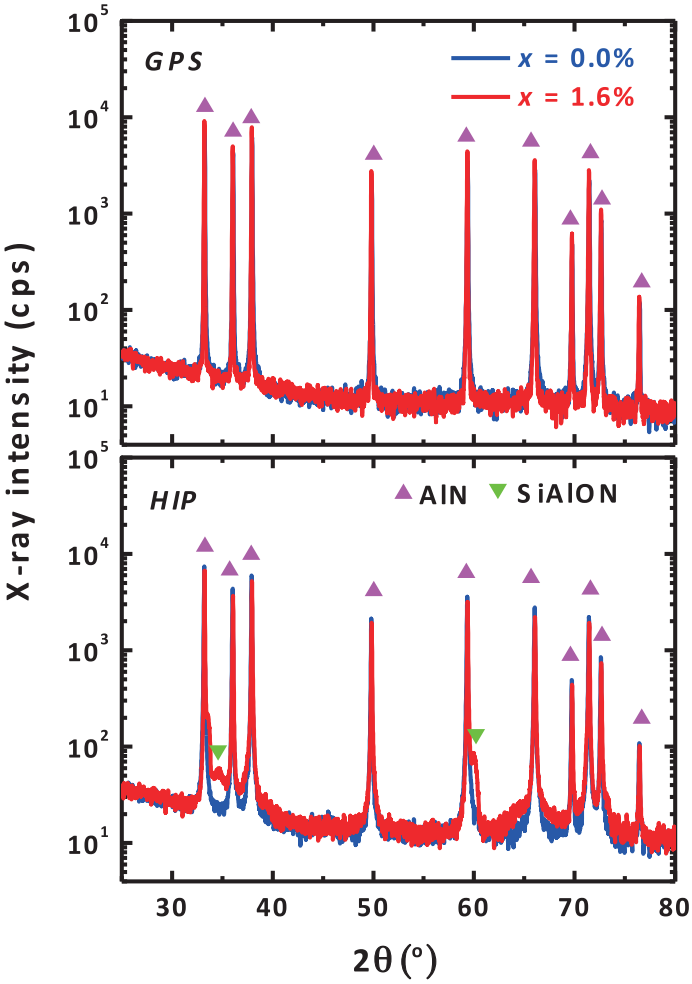

Figure A2-2. *XRD results of x=0.0% and 1.6% of Si-doped AlN powders sintered by GPS and HIP, respectively.*

A2.2 Chemical properties

Figure A2-3 shows the chemical concentrations of O and Si of Si-doped AlN powders sintered by GPS and HIP methods, measured by thermal evolution (for O) and ICP-OES (for Si). In both GPS and HIP, non-doped AlN powders contain more than 1% of O exists at un-doped AlN powders. As for 1.6% Si-doped AlN, GPS specimen have 0.2% O and 0.2% Si. It could be seen a decrease of O and constant amount of Si. This indicates that O reacts with Si to form silicon mono-oxide (SiO) vapor. On the other hand, HIP sample contains about 1% O and 1% Si.

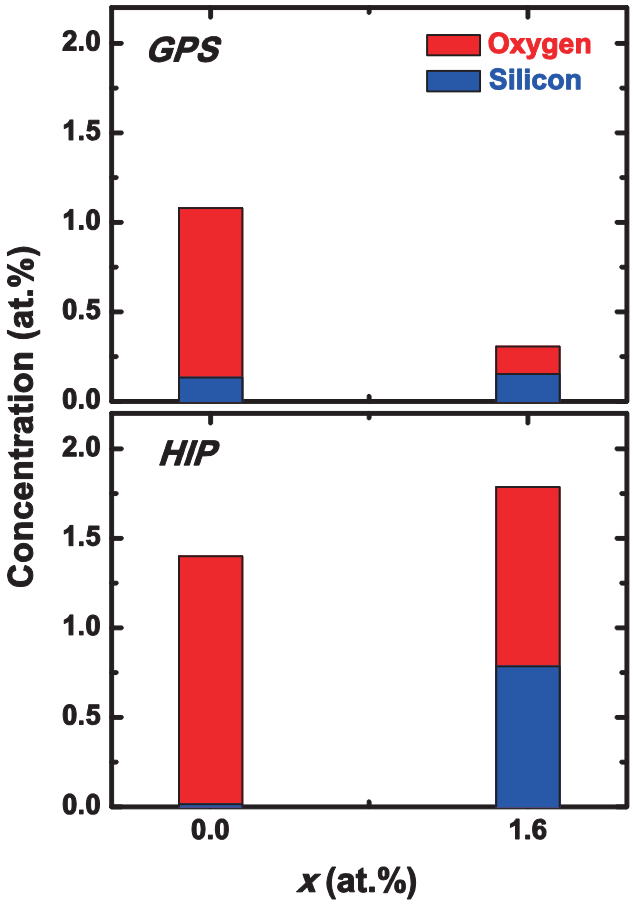

Figure A2-3. *Chemical compositions of O and Si of Si-doped AlN powders sintered by GPS and HIP, respectively.*

A2.3 Optical properties

Figure A2-4 shows the CL spectra of Si-doped AlN powders with different Si concentrations sintered by GPS and HIP methods. Inserted images show the normalized CL peaks. The GPS samples show a clear variation of CL intensities with *x*, and the normalized spectra show the dominant peak was 3.2 eV at x=0.0%, and x>2.0% but 3.6 eV at x=1.6%. The crystal quality of GPS specimen was significantly improved at medium Si-doping, resulting in the maximum intensity. On the other hand, the HIP samples show smaller variation in CL intensity. If we attribute 3.2 eV and 3.6 eV emissions to V_{Al} and V_N respectively, V_{Al} may be easily created while V_N suppressed in HIP specimens.

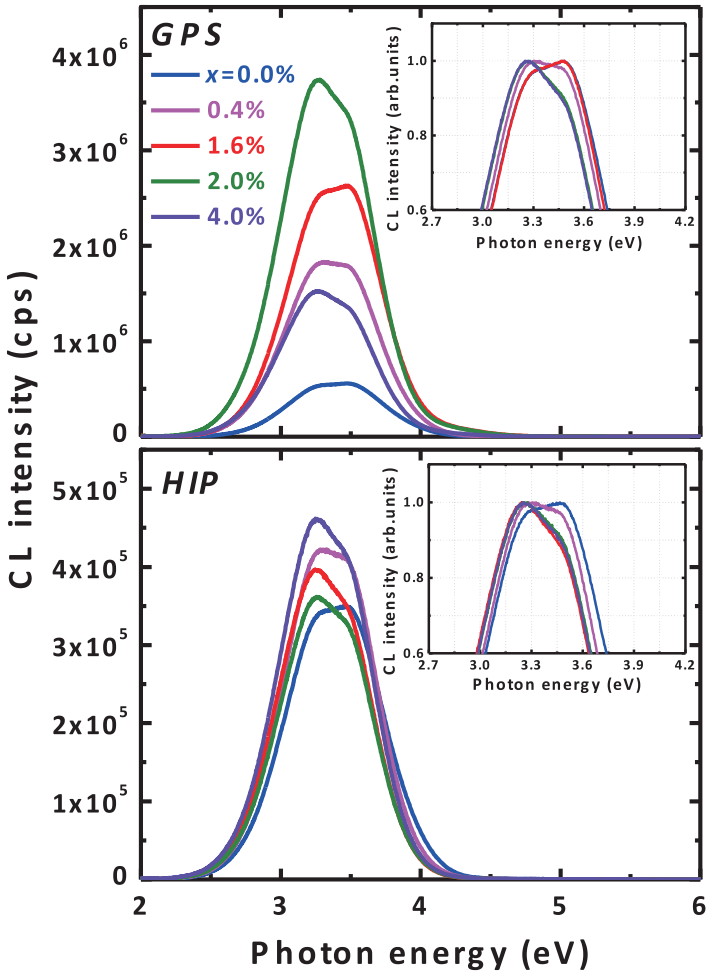

Figure A2-4. *CL spectrum of Si-doped AlN powders with variety of x. Inserted images are the normalized CL spectrum.*

Figure A2-5 is the cross-sectional SE and CL images taken at 4.2 eV and at 3.6 eV for 1.6% Si-doped AlN powder sintered by GPS (a, b, c) and HIP (e, f, g), and schematics of specimens (GPS (d) and HIP (h)). These data show that the GPS powders were connected each other and coated by Si-N layers, which has promoted particle growth. On the other hand, the sintering process does not occur at the HIP powders, with SiAlON particles existing among AlN particles.

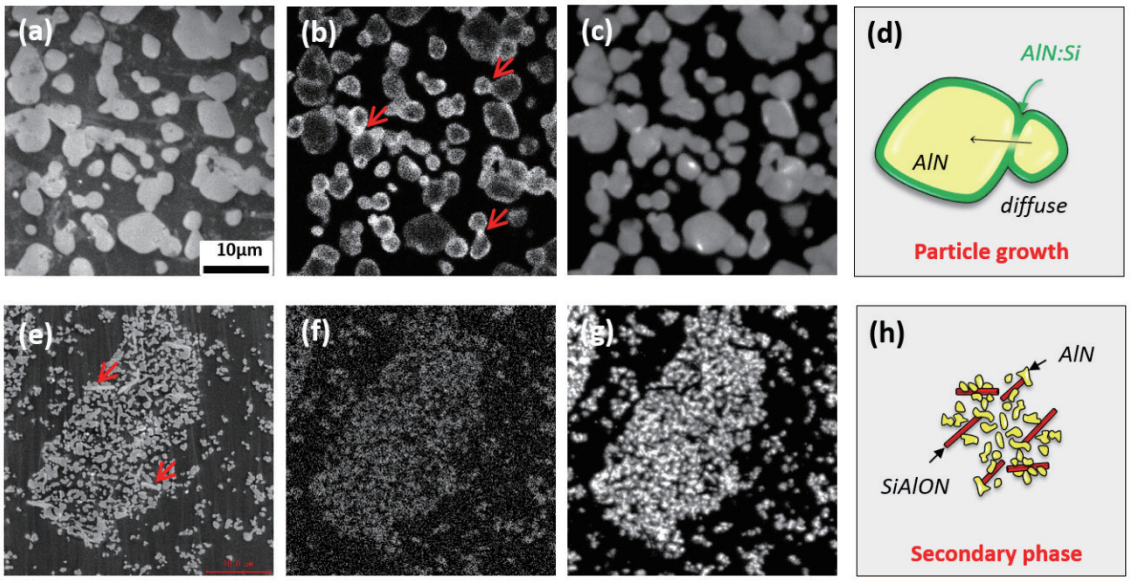

Fig.A2-5 *Cross-sectional SE and CL images taken at 4.2 eV and 3.6 eV for 1.6% Si-doped AlN powder sintered by GPS (a,b,c) and HIP (e,f,g). Schematics for each method (GPS (d) and HIP (h)).*

A2.4 Discussion and summary

All HIP powders contain higher amount of O and Si. This discrepancy may be attributed to the gas purity. As can be seen the diagram of GPS and HIP furnace in Figure 2-1 and 2-2, N_2 gas is continuously flowing in GPS furnace, during sintering, so that N_2 gas purity is maintained. In HIP process, on the other hand, N_2 gas remains and fresh gas is only supplied to keep the pressure. Thus, the N_2 gas may contain higher amount of O gas. This may suppressed the AlN sintering.

Abbreviations

AlN	Aluminum nitride
AlGaN	Aluminum gallium nitride
AlGaInN	Aluminum gallium indium nitride
AlInN	Aluminum indium nitride
Ar	Argon
CCD	Charge coupled device
CL	Cathodoluminescence
CVD	Chemical vapor deposition
DAP	Donor-acceptor pairs
Eu	Europaeum
E-beam	Electron beam
EDS	Energy-dispersive X-ray spectroscopy
EPMA	Electron probe micro-analyzer
ESR	Electron spin resonance
eV	Electron voltage
GaN	Gallium nitride
GPS	Gas pressure sintering
HIP	Hot isostatic pressing
SEM	Scanning electron microscope
Si	Silicon
Si_3N_4	Silicon nitride
Si_{Al}	Silicon substitution in Al-site

TEM	Transmission electron microscope
hυ	Photon energy
HRTEM	High-resolution transmission electron microscopy
ICP-OES	Inductively coupled plasma-optical emission spectrometry
MBE	Molecular beam epitaxy
M_{Al}	Metal substitution in Al-site
N_2	Nitrogen
NH_3	Ammonia
NBE	Near band edge emission
O	Oxygen
O_N	O substitution in N-site
PL	Photoluminescence
SE	Secondary electron
SEM	Scanning electron microscope
STM	Scanning tunneling microscope
TEM	Transmission electron microscope
UV	Ultraviolet
UVA	Ultraviolet A
UVB	Ultraviolet B
UVC	Ultraviolet C
V_{Al}	Aluminum vacancy
V_N	Nitrogen vacancy
XRD	X-ray diffraction
XPS	X-ray photoelectron spectroscopy

List of figures

List of tables

List of publications

1 Y. Cho, T. Sekiguchi, T. Kimura, H. Iwai "Imaging and spectroscopy of secondary electrons from AlN and beta-SiAlON ceramics using fountain detector" *Superlattices and Microstructures, accepted for publication*

2 Y. Cho, B. Dierre, T. Sekiguchi, T. Suehiro, K. Takahashi, T. Takeda, R. J. Xie, Y. Yamamoto, N. Hirosaki "Low-energy Cathodoluminescence for (Oxy)Nitride phosphors" *Journal of visualized experiments, accepted for publication*

3 J. li, B. Liu, W. Yang, Y. Cho, X. Zhang, D. Benjamin, T. Sekiguchi, A. wu, X. Jiang "Solubility and crystallographic facet tailoring of $(GaN)_{1-x}(ZnO)_x$ pseudobinary solid-solution nanostructures as promising photocatalysts" Nanoscale, accepted for publication

4 Y. Cho, B. Dierre, N. Fukata, N. Hirosaki, K. Marumoto, D. Son, K. Takahashi, T. Takeda, T. Sekiguchi "Defects and luminescence control of AlN ceramic by Si-doping" *Scripta Materialia* **110,** 109–112 (2016)

5 C. Zhang, T. Uchikoshi, R. J. Xie, L. Liu, Y. Cho, Y. Sakka, N. Hirosaki, T. Sekiguchi "Reduced thermal degradation of the red-emitting $Sr_2Si_5N_8:Eu^{2+}$ phosphor via thermal treatment in nitrogen" *Journal of Materials Chemistry C* **3(29),** 7642 (2015)

6 C. N. Zhang, T. Uchikoshi, L. H. Liu, B. Dierre, Y. Cho, Y. Sakka, N. Hirosaki, T. Sekiguchi "Textured Beta-Sialon:Eu^{2+} Phosphor Deposits Fabricated by Electrophoretic Deposition (EPD) Process within a Strong Magnetic Field: Preparation Process and Photoluminescence (PL) Properties Depending on Orientation" *Key Engineering Materials* **654,** 268 (2015).

7 L. Liu, L. Wang, C. Zhang, Y. Cho, B. Dierre, N. Hirosaki, T. Sekiguchi, R. J. Xie "Strong Energy-Transfer-Induced Enhancement of Luminescence Efficiency of Eu^{2+} and Mn^{2+} Codoped Gamma-AlON for Near-UV-LED-Pumped" *Solid State Lighting. Inorganic Chemistry* **54(11),** 5556 (2015)

8 K. Takahashi, B. Dierre, Y. Cho, T. Sekiguchi, R. J. Xie, N. Hirosaki "Microanalysis of Calcium Codoped $LaAl(Si_{6-z}Al_z)(N_{10-z}O_z)(z\sim1):Ce^{3+}$ Blue Phosphor" *Journal of the American Ceramic Society* **98(4),** 1253 (2015)

9 J. Zhu, R. J. Xie, T. Zhou, Y. Cho, T. Suehiro, T. Takeda, M. Lu, T. Sekiguchi, N. Hirosaki "Moisture-induced degradation and its mechanism of $(Ca,Sr)AlSiN_3:Eu^{2+}$, a red-color-converter for solid state lighting" *Journal of Materials Chemistry C* **3(13),** 3181 (2015)

10 Y. Cho, B. Dierre, T. Takeda, K. Takahashi, N. Hirosaki, and T. Sekiguchi "Influence of Si on the particle growth of AlN ceramics" *Applied Physics Express* **7,** 115503 (2014)

List of presentations

(Oral presentation)

1 Y. Cho, B. dierre, K. Takahashi, T. Takeda, N. Fukata, N. Hirosaki, T. Sekiguchi, "Improvement of luminescence properties and particle growth of AlN phosphors by Si-doping" *The 228th ECS fall meeting*, Arizona, America (October, 2015)

2 Y. Cho, B. dierre, K. Takahashi, T. Takeda, N. Fukata, N. Hirosaki, T. Sekiguchi, "TEM and CL analysis of Si-doped AlN powders" *The 76th JSAP Autumn Meeting 2015*, Nagoya, Japan (September, 2015)

3 Y. Cho, B. dierre, K. Takahashi, T. Takeda, N. Fukata, N. Hirosaki, T. Sekiguchi, "Defects, luminescence, particle growth of Si-doped AlN powder" *The 18th Joint Symposium on Electronic Materials*, Ansan, Korea (August, 2015)

4 Y. Cho, K. Takahashi, B. dierre, R.J. Xie, N. Hirosaki, T. Sekiguchi, “Microscopic approach for optimizing the growth conditions of $LaAl(Si_{6-z}Al_z)(N_{10-z}O_z)(z\sim1):Ce^{3+}$ blue phosphor” *The 62st JSAP Spring Meeting 2015*, Tokyo, Japan (March, 2015)

5 Y. Cho, B. Dierre, T. Takeda, K. Takahashi, N. Fukata, N. Hirosaki, T. Sekiguchi “Conditions and mechanism for crystal growth of Si-doped AlN powders” *The 75th JSAP Autumn Meeting 2014*, Tokyo, Japan (September, 2014)

6 Y. Cho, B. Dierre, T. Takeda, D. H. Son, K. Takahashi, Y. Kamigaki, N. Fukata, N. Hirosaki, T. Sekiguchi "Influence of Si-doping on the luminescence and defect evolution of AlN" *The 61st JSAP Spring Meeting 2014*, Tokyo, Japan (March, 2014)

7 Y. Cho, B. Dierre, T. Takeda, D. H. Son, K. Takahashi, Y. Kamigaki, N. Fukata, N. Hirosaki, T. Sekiguchi, "Structural and optical properties of Si_3N_4-doped AlN as UV emitters" *The 74th JSAP Autumn Meeting 2013*, Kyoto, Japan (September, 2013)

8 Y. Cho, B. Dierre, T. Takeda, D. H. Son, K. Takahashi, Y. Kamigaki, N. Fukata, N. Hirosaki, T. Sekiguchi "Influence of Si-doping on the structure and optical properties of AlN" *The 16th Joint Symposium on Electronic Materials*, Ulsan, Korea (August, 2013)

(Poster presentation)

1 Y. Cho, B. dierre, K. Takahashi, T. Takeda, N. Fukata, N. Hirosaki, T. Sekiguchi, "Enhancement of particle growth and luminescence of AlN by Si-doping" *The 11th International Nanotechnology International Conference on Communication and Cooperation (INC 11)*, Fukuoka, Japan (May, 2015)

2 Y. Cho, K. Takahashi, B. dierre, T. Takeda, N. Hirosaki, T. Sekiguchi, "A comparison between GPS and HIP methods for Si-doped AlN powders synthesis" *International symposium for phosphor materials and applications (Phosphor safari 2015)*, Niigata, Japan (July, 2015)

3 Y. Cho, B. Dierre, T. Takeda, K. Takahashi, N. Hirosaki, T. Sekiguchi, “Effect of Si-doping on the luminescence and particle growth of AlN phosphors” *International symposium for phosphor materials and applications (Phosphor safari 2014)*, Kunming, China (November, 2014)

4 Y. Cho, B. Dierre, T. Takeda, K. Takahashi, N. Hirosaki, T. Sekiguchi, “Defect evolution of AlN particle by Si” *12th international workshop on Beam Injection Assessment of Microstructures in Semiconductors (BIAMS 12)*, Tsukuba, Japan (Jun, 2014)

5 Y. Cho, B. Dierre, T. Takeda, D. H. Son, K. Takahashi, Y. Kamigaki, N. Fukata, N. Hirosaki, T. Sekiguchi, “Defects dependence in AlN with Si doping”, *10th Materials Science School for Young Scientists*, Sendai, Japan (November, 2013)

6 Y. Cho, B. Dierre, T. Takeda, D. H. Son, K. Takahashi, Y. Kamigaki, N. Fukata, N. Hirosaki, T. Sekiguchi, “Effect of Si3N4-doping on the structure and UV emission properties of AlN”, *NIMS conference 2013*, Tsukuba, Japan (May, 2013)

References

[1] S. Strite, "GaN, AlN, and InN: A review," *J. Vac. Sci. Technol. B*, **10** [4] 1237–31 (1992).

[2] E. Kuokstis, J. Zhang, Q. Fareed, J.W. Yang, G. Simin, M.A. Khan, R. Gaska, M. Shur, *et al.*, "Near-band-edge photoluminescence of wurtzite-type AlN," *Appl. Phys. Lett.*, **81** [15] 2755–4 (2002).

[3] Y. Taniyasu, M. Kasu, and T. Makimoto, "An aluminium nitride light-emitting diode with a wavelength of 210 nanometres," *Nature*, **441** [7091] 325–328 (2006).

[4] *ISO 21348 Definitions of Solar Irradiance Spectral Categories*. 2004.

[5] P.E. Hockberger, "A History of Ultraviolet Photobiology for Humans, Animals and Microorganisms," *Photochemistry and Photobiology*, **76** [6] 561–579 (2002).

[6] H.Y. Jiang, S. Kelch, and A. Lendlein, "Polymers Move in Response to Light," *Adv. Mater.*, **18** [11] 1471–1475 (2006).

[7] I.W. Boyd and J.Y. Zhang, "New large area ultraviolet lamp sources and their applications," *Nuclear Instruments and Methods in Physics Research Section B: Beam Interactions with Materials and Atoms*, **121** [1-4] 349–356 (1997).

[8] D. Praschak, T. Bahners, and E. Schollmeyer, "Excimer UV lamp irradiation induced grafting on synthetic polymers," *Applied Physics A: Materials Science & Processing*, **71** [5] 577–581 (2000).

[9] Crystal. IS corp., "UVC LEDs Provide More Benefits than Traditional UV Lamps in Instrumentation," 1–2 (2013).

[10] J. Zhang, H. Zhao, and N. Tansu, "Effect of crystal-field split-off hole and heavy-hole bands crossover on gain characteristics of high Al-content AlGaN quantum well lasers," *Appl. Phys. Lett.*, **97** [11] 111105–4 (2010).

[11] T.M. Al tahtamouni, J.Y. Lin, and H.X. Jiang, "Optical polarization in c-plane Al-rich AlN/$Al_xGa_{1-x}N$ single quantum wells," *Appl. Phys. Lett.*, **101** [4] 042103–4 (2012).

[12] Y. Taniyasu and M. Kasu, "Polarization property of deep-ultraviolet light emission from C-plane AlN/GaN short-period superlattices," *Appl. Phys. Lett.*, **99** [25] 251112–5 (2011).

[13] Y.-H. Lu *et al.,* "Tailoring of polarization in electron blocking layer for electron confinement and hole injection in ultraviolet light-emitting diodes," *J. Appl. Phys.*, **115** [11] 113102–7 (2014).

[14] G. Liu *et al.*, "Metalorganic vapor phase epitaxy and characterizations of nearly-lattice-matched AlInN alloys on GaN/sapphire templates and free-standing GaN substrates," *Journal of Crystal Growth*, **340** [1] 66–73 (2012).

[15] R.B. Chung, F. Wu, R. Shivaraman, S. Keller, S.P. DenBaars, J.S. Speck, and S. Nakamura, "Growth study and impurity characterization of $Al_xIn_{1-x}N$ grown by metal organic chemical vapor deposition," *Journal of Crystal Growth*, **324** [1] 163–167 (2011).

[16] T. Suzuki *et al.*, "Trench-Shaped Defects on AlGaInN Quantum Wells Grown under Different Growth Pressures," *Jpn. J. Appl. Phys.*, **52** [8S] 08JB27–5 (2013).

[17] H. Zhao, G. Liu, J. Zhang, J.D. Poplawsky, V. Dierolf, and N. Tansu, "Approaches for high internal quantum efficiency green InGaN light-emitting diodes with large overlap quantum wells," *Optics Express*, **19** [104] A991–A1007 (2011).

[18] M. Asif Khan, "AlGaN multiple quantum well based deep UV LEDs and their applications," *Phys. Status Solidi A*, **203** [7] 1764–1770 (2006).

[19] K.H. Kim, Z.Y. Fan, M. Khizar, M.L. Nakarmi, J.Y. Lin, and H.X. Jiang, "AlGaN-based ultraviolet light-emitting diodes grown on AlN epilayers," *Appl. Phys. Lett.*, **85** [20] 4777–4 (2004).

[20] J. Zhang, H. Zhao, and N. Tansu, "Large optical gain AlGaN-delta-GaN quantum wells laser active regions in mid- and deep-ultraviolet spectral regimes," *Appl. Phys. Lett.*, **98** [17] 171111–4 (2011).

[21] S.V. Ivanov, V.N. Jmerik, D.V. Nechaev, V.I. Kozlovsky, and M.D. Tiberi, "E-beam pumped mid-UV sources based on MBE-grown AlGaN MQW," *Phys. Status Solidi A*, **212** [5] 1011–1016 (2015).

[22] T. Oto, R.G. Banal, K. Kataoka, M. Funato, and Y. Kawakami, "100 mW deep-ultraviolet emission from aluminium-nitride-based quantum wells pumped by an electron beam," *Nature Photonics*, **4** [11] 767–770 (2010).

[23] D.S. Thakare, S.K. Omanwar, P.L. Muthal, S.M. Dhopte, V.K. Kondawar, and S.V. Moharil, "UV-emitting phosphors: synthesis, photoluminescence and applications," *Phys. Status Solidi A*, **201** [3] 574–581 (2004).

[24] İ. Pekgözlü, "A novel UV-emitting phosphor_$LiSr_4(BO_3)_3$_Pb^{2+}," *Journal of Luminescence*, **143** [C] 93–95 (2013).

[25] P.D. Belsare, C.P. Joshi, S.V. Moharil, V.K. Kondawar, P.L. Muthal, and S.M. Dhopte, "Preparation of Ce^{3+}-activated UV-emitting fluoride phosphors," *Radiation Effects and Defects in Solids*, **164** [3] 197–203 (2009).

[26] M. Yanagihara, T. Tsuji, M.Z. Yusop, M. Tanemura, S. Ono, T. Nagami, K. Fukuda, T. Suyama, *et al.*, "Research Article Vacuum Ultraviolet Field Emission Lamp Consisting of Neodymium Ion Doped Lutetium Fluoride Thin Film as Phosphor," *The Scientific World Journal*, 1–5 (2014).

[27] K. Watanabe, T. Taniguchi, T. Niiyama, K. Miya, and M. Taniguchi, "Far-ultraviolet plane-emission handheld device based on hexagonal boron nitride," *Nature Photonics*, 3, 591–594 (2009).

[28] Y. Cho, J. Koo, Y. Cho, W. Lee, J. Lee, B. Lee, S. Lee, and J. Chang, "Synthesis of AlON materials for UV emitting devices," *phys. stat. sol. (c)*, **10** [5] 861–864 (2013).

[29] A. Franco Júnior and D.J. Shanafield, "Thermal conductivity of polycrystalline aluminum nitride (AlN) ceramics," *Cerâmica*, **50** [315] 247–253 (2004).

[30] X. Du, M. Qin, A. Rauf, Z. Yuan, B. Yang, and X. Qu, "Structure and properties of AlN ceramics prepared with spark plasma sintering of ultra-fine powders," *Materials Science and Engineering: A*, **496** [1-2] 269–272 (2008).

[31] R.A. Youngman and J.H. Harris, "Luminescence Studies of Oxygen-Related Defects In Aluminum Nitride," *J. Am. Ceram. Soc.*, **73** [11] 3238–3246 (1990).

[32] T. Mattila and R.M. Nieminen, "Point-defect complexes and broadband luminescence in GaN and AlN," *Phys. Rev. B*, **55** [15] 9571–9576 (1997).

[33] A. Sedhain, L. Du, J.H. Edgar, J.Y. Lin, and H.X. Jiang, "The origin of 2.78 eV emission and yellow coloration in bulk AlN substrates," *Appl. Phys. Lett.*, **95** [26] 262104–4 (2009).

[34] K. Laaksonen, M.G. Ganchenkova, and R.M. Nieminen, "Vacancies in wurtzite GaN and AlN," *J. Phys.: Condens. Matter*, **21** [1] 015803–7 (2008).

[35] N.T. Son, M. Bickermann, and E. Janzén, "Silicon in AlN: shallow donor and DX behaviors," *phys. stat. sol. (c)*, **8** [7-8] 2167–2169 (2011).

[36] J.M. Vail, T. Haroon, J. Hernandez-Melgar, D.K. Chevrier, and R. Pandey, "Nitrogen vacancy and oxygen impurity in AlN: spintronic quantum dots," *Radiation Effects and Defects in Solids*, **164** [10] 585–591 (2009).

[37] C. Stampfl and C.G. Van de Walle, "Theoretical investigation of native defects, impurities, and complexes in aluminum nitride," *Phys. Rev. B*, **65** [15] 155212–10 (2002).

[38] A. Kai, D. Tomohiro, Y. Kanechika, and T. Miki, "Electron Spin Resonance of Defects Related to Thermal Conductivity in AlN Ceramics," *Jpn. J. Appl. Phys.*, **47** [8] 6394–6398 (2008).

[39] Y.F. Zhukovskii, N. Pugno, A.I. Popov, C. Balasubramanian, and S. Bellucci, "Influence of F centres on structural and electronic properties of AlN single-walled nanotubes," *J. Phys.: Condens. Matter*, **19** [39] 395021–18 (2007).

[40] D.F. Hevia, C. Stampfl, F. Viñes, and F. Illas, "Microscopic origin of n-type behavior in Si-doped AlN," *Phys. Rev. B*, **88** [8] 085202–6 (2013).

[41] R. Zeisel, M.W. Bayerl, S.T.B. Goennenwein, R. Dimitrov, O. Ambacher, M.S. Brandt, and M. Stutzmann, " DX -behavior of Si in AlN ," *Phys. Rev. B*, **61** [24] R16283–R16286 (2000).

[42] N.T. Son, M. Bickermann, and E. Janzén, "Shallow donor and DX states of Si in AlN," *Appl. Phys. Lett.*, **98** [9] 092104–4 (2011).

[43] G. Sarusi, O. Moshe, S. Khatsevich, D.H. Rich, J. Salzman, B. Meyler, M. Shandalov, and Y. Golan, "Cathodoluminescence study of micro-crack-induced stress relief for AlN films on Si(111)," *Journal of Electronic Materials*, **35** [12] L15–L19 (2006).

[44] B.N. Pantha, A. Sedhain, J. Li, J.Y. Lin, and H.X. Jiang, "Probing the relationship between structural and optical properties of Si-doped AlN," *Appl. Phys. Lett.*, **96** [13] 131906 (2010).

[45] R.M. German, *Sintering Theory and Practice*. Elsevier, 2014.

[46] A. Lakshmanan, *Sintering of Ceramics – New Emerging Techniques,* Intech, 2012.

[47] L. Silvestri, K. Dunn, S. Prawer, and F. Ladouceur, "Concentration of point defects in wurtzite AlN: A hybrid functional study," *EPL*, **98** [3] 36003–7 (2012).

[48] P. Lu, R. Collazo, R.F. Dalmau, G. Durkaya, N. Dietz, and Z. Sitar, "Different optical absorption edges in AlN bulk crystals grown in m- and c-orientations," *Appl. Phys. Lett.*, **93** [13] 131922–4 (2008).

[49] K.B. Nam, M.L. Nakarmi, J. Li, J.Y. Lin, and H.X. Jiang, "Photoluminescence studies of Si-doped AlN epilayers," *Appl. Phys. Lett.*, **83** [14] 2787–4 (2003).

[50] B. Dierre, X.L. Yuan, K. Inoue, N. Hirosaki, R.-J. Xie, and T. Sekiguchi, "Role of Si in the Luminescence of AlN:Eu,Si Phosphors," *J. Am. Ceram. Soc.*, **92** [6] 1272–1275 (2009).

[51] T. Takeda, R.-J. Xie, and N. Hirosaki, "Local Structure Analysis in Nitride and Oxynitride Phosphors," *ECS Journal of Solid State Science and Technology*, **2** [2] R3132–R3137 (2012).

[52] T. Takeda, N. Hirosaki, R.-J. Xie, K. Kimoto, and M. Saito, "Anomalous Eu layer doping in Eu, Si co-doped aluminium nitride based phosphor and its direct observation," *J. Mater. Chem.*, **20** [44] 9948–7 (2010).

[53] B. Dierre, X.M. Zhang, N. Fukata, T. Sekiguchi, T. Suehiro, T. Takeda, R.-J. Xie, and N. Hirosaki, "Growth Temperature Influence on the Luminescence of Eu,Si-Codoped AlN Phosphors," *ECS Journal of Solid State Science and Technology*, **2** [7] R126–R130 (2013).

[54] Tokuyama corp., Lot.No. 05294, type E

[55] UBE corp., Lot.No. A85111, SN-E10

[56] R.-J. Xie and N. Hirosaki, "Silicon-based oxynitride and nitride phosphors for white LEDs—A review," *Sci. Technol. Adv. Mater.*, **8** [7-8] 588–600 (2008).

[57] R.-J. Xie, Y.Q. Li, and N.H.A.H. Yamamoto, *Nitride Phosphors and Solid-State Lighting,* CRC press, 2011.

[58] H.T. Larker, *Hot Isostatic Pressing of Ceramics — an Overview*. Elsevier, 1994.

[59] G. Eisenbeis, "Scanning Electron Microscopy and X-Ray Microanalysis," *Micron*, **34** [8] 453 (2003).

[60] W.H. Bragg, "The Reflection of X-Rays by Crystals," *Nature*, **91** [2280] 477–477 (1913).

[61] R. Castaing, *The Fundamentals of Quantitative Electron-Probe Microanalysis*. Springer US, Boston, MA, 1961.

[62] I. Olefjord, *X-ray photoelectron spectroscopy*. Wiley-VCH Verlag GmbH, Weinheim, Germany, 1997.

[63] "Inductively coupled plasma—Optical emission spectroscopy ICP Information Newsletter," *Spectrochimica Acta Part B: Atomic Spectroscopy*, **30** [8] 308 (1975).

[64] D.A. Lawrenz and J. Mitchell, *Thermal Evolution Methods for Carbon, Sulfur, Oxygen, Nitrogen and Hydrogen in Iron and Steel Analysis*. John Wiley & Sons, Ltd, Chichester, UK, 2006.

[65] S.K. Misra, *Basic Theory of Electron Paramagnetic Resonance*. Wiley-VCH Verlag GmbH & Co. KGaA, Weinheim, Germany, 2011.

[66] M. Palczewska and M. Kamińska, *Magnetic resonance studies of defects in GaN and related compounds*. Elsevier, 2000.

[67] J.S. Blakemore, *Solid State Physics*, 2nd ed. Cambridge University Press, Cambridge, 1985.

[68] B.G. Yacobi and D.B. Holt, "Cathodoluminescence scanning electron microscopy of semiconductors," *J. Appl. Phys.*, **59** [4] R1–25 (1986).

[69] B. Dierre, X. Yuan, and T. Sekiguchi, "Low-energy cathodoluminescence microscopy for the characterization of nanostructures," *Sci. Technol. Adv. Mater.*, **11** [4] 043001–11 (2010).

[70] S.K. Lim, M. Brewster, F. Qian, Y. Li, C.M. Lieber, and S. Gradečak, "Direct Correlation between Structural and Optical Properties of III−V Nitride Nanowire Heterostructures with Nanoscale Resolution," *Nano Lett.*, **9** [11] 3940–3944 (2009).

[71] S.V. Komarov, D.V. Kuznetsov, V.V. Levina, and M. Hirasawa, "Formation of SiO and Related Si-Based Materials Through Carbothermic Reduction of Silica-Containing Slag," *Mat. Transac.*, **46** [4] 827–834 (2005).

[72] Y. OKAMOTO, "Surface structure of CoO-MoO_3/Al_2O_3 catalysts studied by X-ray photoelectron spectroscopy," *Journal of Catalysis*, **65** [2] 448–460 (1980).

[73] M. Torkar, D. Mandrino, and V. Rosenband, "XPS analysis of pulsed-plasma ion-nitrided Ni- and Ti-aluminides," *Vacuum*, **80** [1-3] 35–39 (2005).

[74] N. Lieske, "Formation of Al-nitride films at room temperature by nitrogen ion implantation into aluminum," *J. Appl. Phys.*, **52** [9] 5806–6 (1981).

[75] J.A. TAYLOR, "Further examination of the Si KLL Auger line in Silicon Nitride thin films," *Applications of Surface Science*, **7** 168–184 (1981).

[76] H. Morko, *Handbook of Nitride Semiconductors and Devices*. Wiley-VCH Verlag GmbH & Co. KGaA, Weinheim, Germany, 2008.

[77] P.S. Poskozim, "Multiply Bonded Main Group Metals and Metalloids (ed.s West, Robert; Stone, F. Gordon A.)," *Journal of Chemical Education*, **75** [6] 698 (1998).

[78] S.-Y. Ren and W.Y. Ching, " Electronic structures of β- and α-silicon nitride ," *Phys. Rev. B*, **23** [10] 5454–5463 (1981).

[79] S.M. Evans, N.C. Giles, L.E. Halliburton, G.A. Slack, S.B. Schujman, and L.J. Schowalter, "Electron paramagnetic resonance of a donor in aluminum nitride crystals," *Appl. Phys. Lett.*, **88** [6] 062112–4 (2006).

[80] S. Schweizer, U. Rogulis, J.M. Spaeth, L. Trinkler, and B. Berzina, "Investigation of Oxygen-Related Luminescence Centres in AlN Ceramics," *Physica Status Solidi (b)*, **219** [1] 171–180 (2000).

[81] T. Koyama, M. Sugawara, T. Hoshi, A. Uedono, J.F. Kaeding, R. Sharma, S. Nakamura, and S.F. Chichibu, "Relation between Al vacancies and deep emission bands in AlN epitaxial films grown by NH_3-source molecular beam epitaxy," *Appl. Phys. Lett.*, **90** [24] 241914–4 (2007).

[82] L. Trinkler and B. Berzina, *Luminescence Properties of AlN Ceramics and Its Potential Application for Solid State Dosimetry*, Chapter4, Intech, 2011.

[83] H.K. Park, J.H. Oh, and Y.R. Do, "Toward scatter-free phosphors in white phosphor-converted light-emitting diodes: reply to comments," *Optics Express*, **21** [4] 5074–5076 (2013).

[84] K.H. Jack, "Sialons and related nitrogen ceramics," *Journal of Materials Science*, **11** [6] 1135–1158 (1976).

[85] A. BERGER, "Inversion Domains in Aluminum Nitride," *Am. Ceram. Soc.,* **74** [5] 1148-1151 (1991).

[86] G. Van Tendeloo, K.T. Faber, and G. Thomas, "Characterization of AIN ceramics containing long-period polytypes," *Journal of Materials Science*, **18** [2] 525–532 (1983).

[87] A.D. Westwood, R.A. Youngman, M.R. McCartney, A.N. Cormack, and M.R. Notis, "Oxygen incorporation in aluminum nitride via extended defects: Part I. Refinement of the structural model for the planar inversion domain boundary," *J. Mater. Res.*, **10** [05] 1270–1286 (1995).

[88] Y. Yan, M. Terauchi, and M. Tanaka, "Structures of polytypoids in AIN crystals containing oxygen," *Philosophical Magazine A*, **77** [4] 1027–1040 (1998).

[89] Y. Yu, I.-L. Tangen, T. Grande, R. Høier, and M.-A. Einarsrud, "HRTEM Investigations of New AlN Polytypoids in the High-AlN Region of the AlN–Al_2O_3–Y_2O_3 System," *J. Am. Ceram. Soc.*, **87** [2] 275–278 (2004).

[90] S. Bhattacharjee, *Introduction to Focused Ion Beams*. Taylor & Francis, 2013.

[91] X. Yi, K. Watanabe, and T. Akiyama, "Fabrication of dense β-SiAlON by a combination of combustion synthesis (CS) and spark plasma sintering (SPS)," *Intermetallics*, **18** [4] 536–541 (2010).